Numerical modelling of plate deformation during subduction with application to back-arc extension

Duo Zhang

School of Earth and Environmental Sciences

Cardiff University

Submitted in partial fulfilment of the requirements for the degree of

Doctor of Philosophy

December 2023

Abstract

back-arc extension is the first stage in the formation of a back-arc basin (BAB). The driving mechanism of back-arc extension is still debated. To better understand the driving mechanism and factors controlling back-arc extension, a series of 2D thermally-driven subduction models with composite rheology are simulated.

Initially, models are investigated with fixed rheology parameters and a homogeneous overriding plate (OP). Varying the initial ages of the plates at the trench, these models show that the most probable driving mechanism of back-arc extension is poloidal flow induced by slab subduction (enhanced by trench retreat). I investigate varying activation energy (E) and prefactor (A) in diffusion, dislocation and Peierls creeps, as well as friction coefficient (fc) and maximum yielding strength (yld_{max}) in yielding deformation. Many modes of plate behaviours are recognised. The models show that a weaker OP does not necessarily facilitate back-arc extension. This is because these models also have a weaker mantle flow, which further verifies the importance of poloidal flow. I investigate extension of an OP with a triangular hot region to mimic a volcanic arc. The models produce back-arc extension at different locations: splitting the arc itself or extension away from the arc. Splitting the arc shows the importance of thermal weakening to OP extension, and extension away from the arc emphasises the role of poloidal flow. These models suggest that splitting the arc is more common (e.g. Mariana Trough and Lau Basin), than not extending at the arc (potentially Japan Sea).

Overall, this study shows that the poloidal flow induced by subduction is the main driving mechanism of back-arc extension together with its thermal weakening of the OP. Extension occurs when the force from the sub-OP flow exceeds the OP strength, as evidenced in the models. Testing these findings will require 3D modelling.

Acknowledgements

'I hate and love. How I do this, perhaps you ask. I know not, but I feel it happening and I am tortured.' — Quintus Lutatius Catulus

Behind PhD degree, there is a long and tough journey, especially when you study in a foreign language, an alien country, and a pandemic. I never thought I would feel such out of control before my PhD life, but I have never regretted that I chose this way. Now, as I stand at the end of this significant phase of my life, I reflect with gratitude on all the individuals who have supported and been a part of my journey during this time.

First and foremost, I sincerely thank my supervisor, Prof. Huw Davies, who helped me with my research and writing throughout my PhD life. He supported me in both academic and daily life. When I first started my research, I had little knowledge of geodynamics and numerical modelling and had some problems with communication. He is very nice and patient with me when I cannot understand some points or express myself accurately, which releases my nerves and makes me more confident. He always monitored my progress during the four years, which encouraged me to keep working when I lacked motivation during COVID-19.

I also thank my colleague, Dr Zhibin Lei, who started his PhD 2 years earlier than I did and did research in the same area as mine. By selflessly sharing his experience, and discussing academic questions with me, he offered a lot of favour with my research.

Thank other members of our group, Dr James Panton, Abigail Plimmer, Nicolas Recalde, and Gwynfor Morgan, for their kindness and friendship. I was very shy to talk to people when I started going to the office after the lockdown. They always invited me to join their activities with open arms and I felt at ease afterwards.

Thank the China Scholarship Council from which the PhD grant supported this study. It allows me to study here and do the research. Thank the supercomputer Hawk at Cardiff University for its support of my modelling. Thank Ian Thomas and Tom

Green who provided support in Fluidity and Hawk, and helped me when I encountered problems with the code.

Thank my parents, who always supported me in studying abroad and comforted me in spirit. Also, thank my old friends Han Wang and Ruihong Chang, who company me through the Internet although we are not physically together. They are my spiritual pillar in a way when I meet difficulties.

Thank Sara De Caroli, a PhD student in the same year and the same school as me, for her companionship during the first few months I came to the foreign place and during the tense weeks we were writing.

Finally, thank everyone I have met in the UK, and thank all my experience during this time. Although some encounters are painful, every single moment has taught me about life.

Contents

List of Figures

List of Tables

Chapter 1

Introduction

Geodynamics is the scientific discipline that studies the large-scale movements of Earth, based on the theory of plate tectonics, which treats the Earth as a continuous medium to study the dynamic processes. The theory of plate tectonics, unique to Earth and considered relevant to life, posits that the Earth's surface is made up of many thin, hard blocks (the lithosphere) that float on a relatively hot, fluid layer (the asthenosphere). These lithospheres which move relative to each other are termed 'plates'. Depending on the different states of relative motion, plate boundaries are classified into three types: convergent, divergent, and transform boundaries. Convergent boundaries are formed by the movement of two plates towards each other, creating a compressive environment. This includes continental collision, oceanic-continental subduction, and oceanic-oceanic subduction. Subduction processes, produce significant volcanic activity and earthquakes, as seen around the present-day longest subduction zone, the Pacific subduction zone. Divergent boundaries are formed by the opposite movement after the plates break apart, with the plates being in a state of extension. Here, hot material wells up from below, forming mid-ocean ridges and generating new oceanic crust, as seen in the Atlantic Ocean. Transform boundaries occur where two

plates slide past each other horizontally, such as the San Andreas transform fault.

At a subduction zone, a subducting plate (SP) subducts beneath the adjacent plate which is called the 'Overriding Plate' (OP), and a deep-sea trench is generated at the boundary of the two plates (Figure 1.1). There is a volcanic arc, which is formed by the partial melting due to the released fluid from the subducted part of the SP (slab), on the OP. The region between the arc and the trench is called the 'fore-arc' and the other side of the arc is called the 'back-arc'. These components make up a subduction system. In contrast to a typical convergent margin, the subduction system is not always under a compressive environment, but sometimes shows a back-arc basin (BAB) which is generated in an extensional regime.

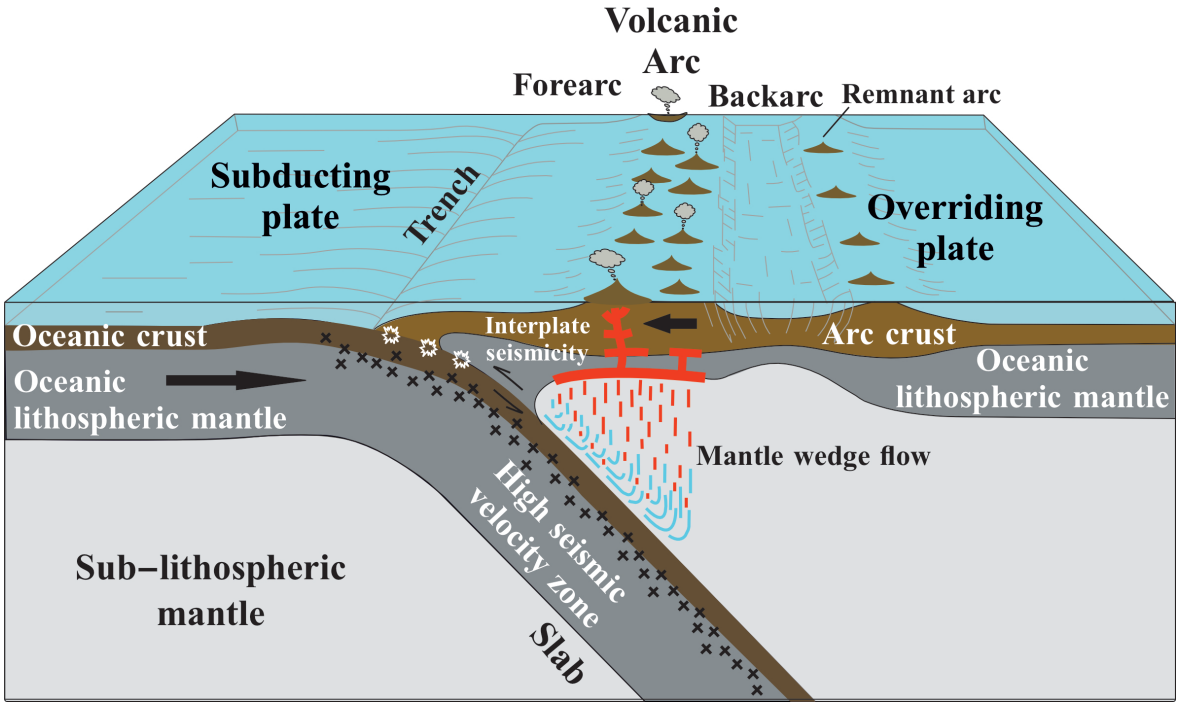

Figure 1.1: A 3D sketch of a subduction system (modified from Schellart 2023).

1.1 Introduction to back-arc basins (BABs)

As a special 'divergent boundary' in the subduction zone, the typical convergent boundary, BAB provides a significant window into plate tectonics by displaying both convergent and divergent margins. The formation of BABs is important for understanding this critical aspect of plate tectonics. The BAB formation process might also offer insights into some types of continent break-up, although it is still different from mid-oceanic ridges.

The subduction zones are distributed widely across the world, mainly along the Pacific margin, in the central- and south-western Atlantic Ocean, in southeast Asia, and in the Mediterranean Sea. However, not every arc is accompanied by a BAB. The BABs are mainly distributed along the western Pacific margin (the Japan Sea, the Mariana Trough, the Lau Basin, the Manus Basin, etc), the eastern Pacific Rim (Bransfield Strait), the central- and south-western Atlantic Ocean (the Grenada Trough and the Scotia Sea), and the Mediterranean Sea (the Alboran Sea, the Ligurian Sea, the Tyrrhenian Sea, etc). Some of them have stopped opening, such as the Alboran Sea (Early Miocene, Platt et al. 2003), the South China Sea (Late Cretaceous to Late Oligocene, Zhou et al. 1995), the South and North Norfolk Basins (Miocene, Mortimer et al. 1998), the Japan Sea (Miocene, Ikeda et al. 2000), the Ligurian Sea (25–16 Ma ago, Rosenbaum and Lister 2004), the Tyrrhenian Sea (Late Miocene–Pliocene, Biju-Duval et al. 1978; Malinverno and Ryan 1986), etc. Active back-arc spreading is currently occurring behind the New Britain (Manus Basin, Taylor 1979; Lee and Ruellan 2006), South Sandwich (Scotia Basin, Barker 1972; Barker and Hill 1981; Barker 1995), New Hebrides (North Fiji Basin, Auzende et al. 1988, 1995), Tonga (Lau Basin), Kermadec (Havre Trough, Wright 1993; Parson and Wright 1996; Caratori Tontini et al. 2019), Hellenic (Aegean Sea, Le Pichon and Angelier 1979; Pe-piper and Piper 1989), and

Izu-Bonin-Mariana (Mariana Trough, Crawford et al. 1981; Martínez et al. 1995; Yan et al. 2022) subduction zones (Jarrard, 1986). The distribution of BABs is shown in Figure 1.2.

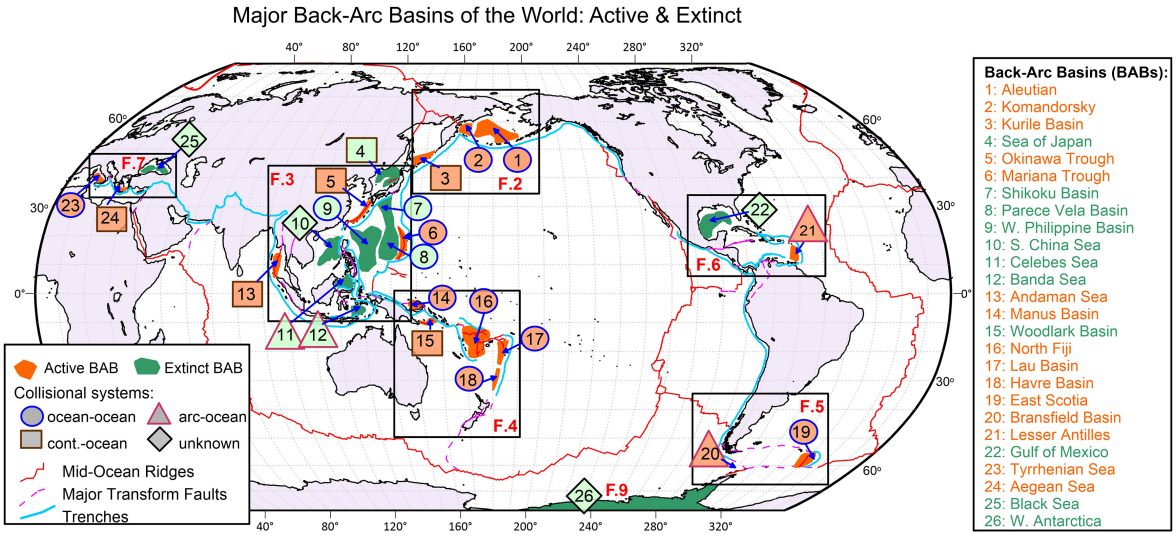

Figure 1.2: Distribution map of back-arc basins (from Artemieva 2023, OA license: CC BY–NC–ND 4.0 DEED). Active BABs are marked in orange and extinct BABs in green.

From these I see that BABs are not always active while subduction is constantly active, in other words, the life span of a BAB is relatively short from a few Myrs to tens of Myrs, while the SP keeps subducting for hundreds of Myrs. In such subduction systems as the Tonga-Kermadec, the Izu-Bonin Mariana (IBM) and the Central Mediterranean, episodic BABs develop (Faccenna et al., 1997; Fujioka et al., 1999; Faccenna et al., 2001; Clark et al., 2008). For example, there are three spreading episodes on the Philippine Sea Plate in the Izu-Bonin-Mariana subduction system (IBM) under the West Pacific subduction. The first spreading episode was produced in the West Philippines which started at about 55 Ma and ended around 33–30 Ma (Deschamps and Lallemand, 2002). Then the Shikoku-Parece-Vela Basin formed during the second episode which started at 30 Ma in the north (Shikoku Basin) and 29–26 Ma in the south (Parece Vela Basin) and ended at about 15 Ma (Sdrolias et al., 2004). After a

period of quiescence lasting about 10 Myr, the present-day back-arc basin, the Mariana Trough formed at 5 Ma (Bibee et al., 1980; Hussong, 1981; Hawkins et al., 1990). BAB extension events change the OP, therefore it is possible to have different OP properties at different times even in the same subduction system.

A complete process of BAB formation can range from 'back-arc extension', to 'rifting' to 'seafloor spreading', but not every BAB initiates seafloor spreading (Artemieva, 2023). As the first stage of formation of a BAB, back-arc extension is essential in this process. Regardless of whether a seafloor is generated, I concentrate on the extension stage in this thesis.

1.2 Previous research of back-arc extension

1.2.1 Numerical modelling of back-arc extension

Back in the 1970s, not long after 2D numerical models of subduction were first built (Minear and Toksöz, 1970), the method was also applied to research BABs. An early representative 2D example developed by Toksöz and Hsui (1978) established two models with different viscosity properties of the convecting layer to study how induced flow (a popular mechanism of BAB formation) could cause marginal basins. Two-dimensional modelling cannot satisfy the need of some numerical experiments, such as when slab width is a factor to be investigated. Thus, 3D numerical modelling started to be used to solve such problems (Dvorkin et al., 1993). This study also asserts that only if the lateral extent of subducting and overriding plates is long enough, that the corner flow of 2D numerical models is not very different from 3D ones in simulating BAB formation. The range of SP widths, which seems to influence the corner flow, varies globally from 300 to 7000 km. Also, Schellart et al. (2007) suggests that trench migration rate can

be affected by slab width and distance to a lateral slab edge. Based on these views, some 3D models have been used though they are laterally homogeneous (Baumgardner, 1985; Clark et al., 2008; Capitanio and Replumaz, 2013; Chen et al., 2015; Balázs et al., 2021). In the past ten years, both 2D and 3D numerical models have been widely used in modelling BAB formation (Arcay et al., 2008; Baitsch-Ghirardello et al., 2014; Nakakuki and Mura, 2013; Gerya, 2011; Schellart and Moresi, 2013; Sternai et al., 2014; Magni et al., 2014; Sheng et al., 2019). The choice of modelling dimensionality depends on the specific question being addressed and the observations that researchers seek to understand. For example, when the model setup needs to be laterally heterogeneous (Li et al., 2013; Magni et al., 2014), a 2D vertical section cannot simulate all the characteristics of the model.

To find out how the subducting and overriding plates influence the back-arc strain, Arcay et al. (2008) implemented two kinds of 2D computer models of intra-oceanic subduction, which are instantaneous and time-dependent, to investigate the velocities of the two plates and convergence rate and the role of water contents in plates, respectively. All the models kinematically set up constant velocities at the beginning, regardless of the buoyancy forces of slabs. Afterwards, fully dynamic models, dynamic models with kinematic boundary conditions or coupled kinematic-dynamic models are more widely used (Clark et al., 2008; Li et al., 2013; Schellart and Moresi, 2013; Sternai et al., 2014; Sheng et al., 2019), and the specific method is related to cases in nature. For example, Clark et al. (2008) imposed initial surface velocity at the trailing edge of the SP in some models (7 cm/yr, similar to the SP velocities in most real subduction zones, including the Western Pacific, the Australian plate, the Java-Sunda and New Hebrides Trenches, and the Cocos and Nazca plates), also fixed the trailing edge of the SP to the box in some other models (Hellenic and Calabria Trenches).

Numerical modelling of BAB formation is developed from that of a subduction

zone. Many early studies of subduction zone dynamics focus on the SP, such as its initial velocity, slab width, age, as well as induced mantle flow (Toksöz and Hsui, 1978; Dvorkin et al., 1993; Arcay et al., 2008; Clark et al., 2008). However, studies of the OP have largely focussed on the influence on it, there are even some models without an OP in their setup (Stegman et al., 2010). With the development of the understanding of OP feedbacks in the subduction simulation (Capitanio et al., 2010), the mechanical/rheological coupling between OP and SP has become an important parameter to investigate (Baitsch-Ghirardello et al., 2014; Sheng et al., 2019). It has been shown that rheological coupling between plates is affected by fluid and melt weakening (Baitsch-Ghirardello et al., 2014; Sheng et al., 2019). Although using different methods and focusing on different points, many researchers, such as Arcay et al. (2008) and Clark et al. (2008), state that plate motion plays an important role in the BAB formation of an intra-oceanic subduction zone. Also, Nakakuki and Mura (2013) points to the importance of plate motion: BABs can be generated when the continental OP moves away from the trench. However, Baitsch-Ghirardello et al. (2014) argues that neither SP velocity nor plate ages have a significant influence on subduction geodynamics, including back-arc extension, using their 2D petrological-thermo-mechanical models. Beyond that, slab/trench rollback has become a very popular mechanism for generating back-arc extension. Hence, several BAB numerical models focus on investigating the mechanism of slab/trench rollback in 2D (Nakakuki and Mura, 2013; Sheng et al., 2019) and 3D simulation (Stegman et al., 2006, 2010; Butterworth et al., 2012; Li et al., 2013; Clio and Pieter, 2013).

Besides plate motion (including velocities of OP and SP), slab width and age of SP, induced mantle flow, rheological coupling between plates, some further factors have been tested, such as viscosity, density and thickness of OP, viscosity of SP (Holt et al., 2015), activation volume (Sheng et al., 2019) and mechanical strength of OP (Capitanio

et al., 2010).

In addition, there are also some BABs not forming in a pure subduction zone setting as stated above, but in a subduction-collision setting (e.g. Tonga (ridge subduction), Aegean, Papua New Guinea, New Zealand (plateau subduction), the Mariana Islands, Vanuatu, and Fiji, Magni et al. 2014). Some relevant numerical models have been established to find out the impact of continental collision (Wallace et al., 2009; Li et al., 2013; Magni et al., 2014). Wallace et al. (2009) suggests that rapid fore-arc rotation caused by collision is an important factor for BAB formation, even though they only model the upper plate of the subduction zone. Li et al. (2013) and Magni et al. (2014) conduct 3D modelling and reveal that the back-arc region spreads when the convergence velocity of continental collision is slow enough (such as 1 cm/yr) or slab windows exist, respectively. However, these studies only explored the factors influencing the initial back-arc extension.

As I see there has been significant modelling of BABs, but there are still many unresolved questions, especially where this relates to the driving mechanism and controls of back-arc extension. These are the focus of this thesis and introduced further next.

1.2.2 Driving mechanism of back-arc extension

The formation of BABs has been a subject of extensive study and debate among geoscientists, with various models proposed to explain their driving mechanisms. The origin of these basins is closely linked to the complex interactions between tectonic plates and underlying mantle dynamics. Since Karig introduced the 'Diapir Model' (Figure 1.3a) in 1971 (Karig, 1971), numerous theories have emerged, each offering a unique perspective on the forces shaping these geological features. Although there are theories like the 'extrusion model' proposed by Mantovani et al. (1996, 1997, 2000, 2001, 2002), which suggest that mantle upwelling under the OP, independent of subduction,

can lead to the formation of BABs, most researchers agree that subduction-related processes play a crucial role in the formation of BABs (Martinez and Taylor, 2002, 2003; Lallemand et al., 2005; Heuret and Lallemand, 2005; Baitsch-Ghirardello et al., 2014; Nakakuki and Mura, 2013; Dal Zilio et al., 2018). This includes the 'corner flow' model (Figure 1.3b), which emphasises the role of shear traction and gravitational collapse in driving back-arc extension. However, some limitations of the corner flow model have been highlighted, such as its inability to fully explain the kinematics of certain subduction zones or the curved shape of arcs.

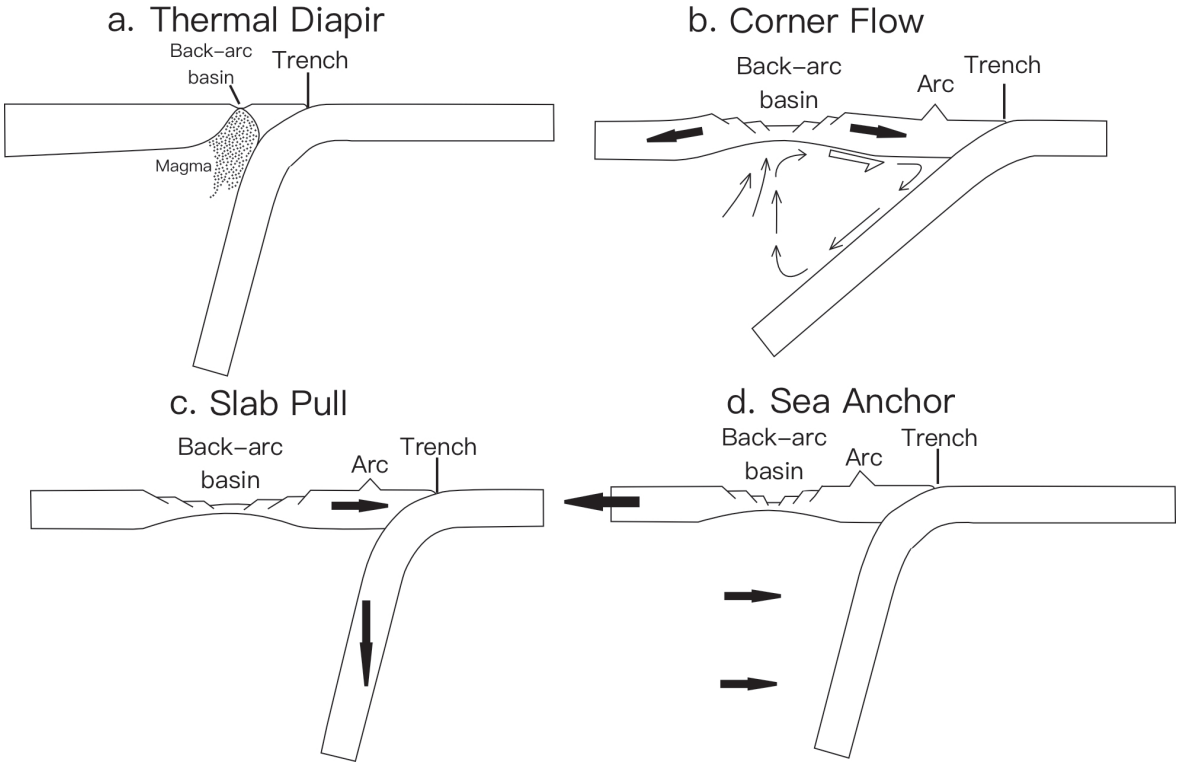

Figure 1.3: Some models showing driving mechanism hypothesises. (a) Diapir model (modified from Karig (1971)); (b) Corner flow model (modified from Mantovani et al. (2001)); (c) Slab pull model (modified from Mantovani et al. (2001)); (d) Sea anchor model (modified from Mantovani et al. (2001)).

Early lithospheric models focus on whether the SP or the OP is the primary driver of back-arc extension. These include the 'sea anchor model' (Figure 1.3c; Scholz and

Campos (1995); Heuret and Lallemand (2005)), where the movement of the OP induces extension, and the 'slab pull/rollback model' (Figure 1.3d), emphasizing the role of the SP (Malinverno and Ryan, 1986; Royden, 1993). Criticisms and questions surrounding these models revolve around the tensional stresses involved and the interaction between the plates and the asthenosphere. An increasing number of researchers have focused on slab rollback in recent years and it has become a popular model to form BABs (Nakakuki and Mura, 2013; Baitsch-Ghirardello et al., 2014; Sheng et al., 2019; Artemieva, 2023), supported by advancements in geophysical technology and computer simulations. This model, evolving from 2D to 3D, proposes that mantle flow induced by slab rollback is a key driver of back-arc extension, including toroidal flow and poloidal flow (Figure 1.4). The toroidal flow can be shown only in 3D models (Gable et al., 1991; Zhong and Gurnis, 1996; Jadamec and Billen, 2010; Jadamec, 2016; Király et al., 2017; Guillaume et al., 2021). The mantle flow focuses on the velocity gradients and shear stresses caused by this flow, offering insights into the interaction between the lithospheric and asthenospheric dynamics in BAB formation.

1.3 Knowledage gaps and aims

1.3.1 Uncertainty of rheology parameters in numerical models

A lot of laboratory rheology deformation experiments evaluate the rheology parameters of different rocks under different conditions, but the uncertainties cannot be ignored because they lead to a large range of parameter values. For example, in olivine, the range of the activation energy of dislocation creep can vary from 138 kJ/mol (Jain et al., 2019) up to 535 kJ/mol under dry conditions (Chopra and Paterson, 1981). The results from the laboratory can be influenced by many factors due to the limitations of

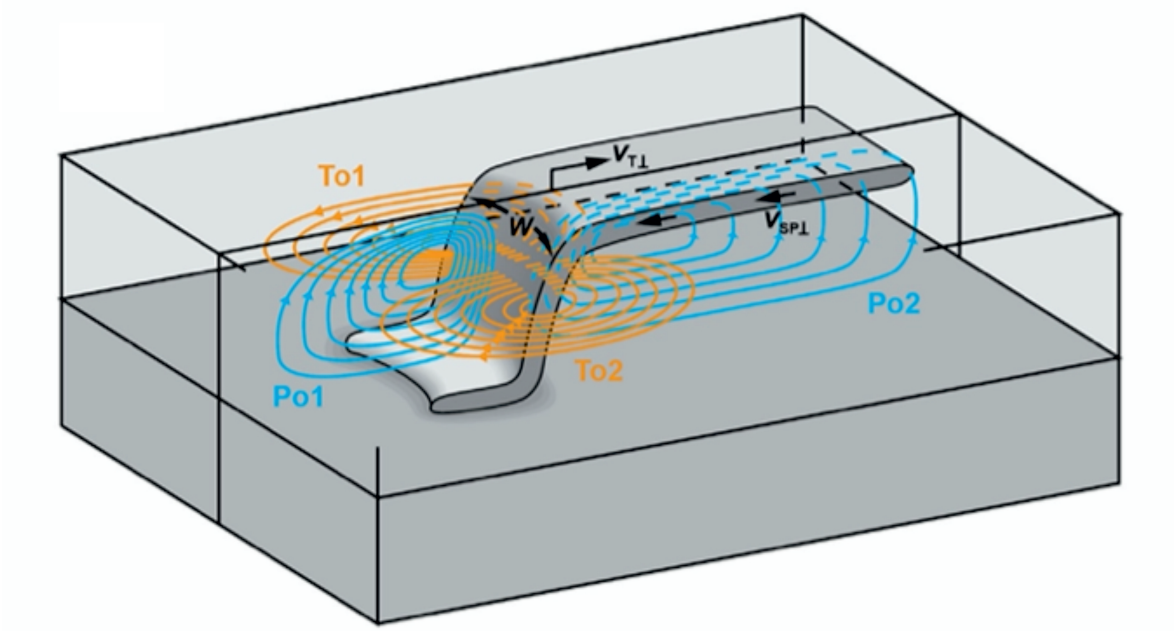

Figure 1.4: 3D perspective view of a subducting plate (SP) and slab showing the two styles of mantle flow associated with subduction. They are poloidal flow (Po1 and Po2) and toroidal flow (To1 and To2) in a setting where the trench is retreating and the slab is rolling back (from Schellart 2023). W indicates slab width.

the laboratory conditions and the different scales between the laboratory and nature. For example, the experimental strain rates in the laboratory are always much higher than in nature, which are 10^{-9}–10^{-4} s^{-1} and 10^{-18}–10^{-14} s^{-1}, respectively (Burov, 2011). Additionally, many other factors such as grain size (Karato et al., 1986), water content (Karato et al., 1986; Hirth and Kohlstedt, 1996), oxygen fugacities (Keefner et al., 2011) and chemical reactions change rock strength and behaviours, but it is difficult to know the natural conditions. These show that the understanding of the rheological deformation mechanism of the mantle is still limited due to the uncertainties, which perhaps make the modelled plates behave unrealistically.

In Chapter 4, I study deep into the complexities of composite rheology, examining how diffusion, dislocation, and Peierls creep, along with yielding strength, come together to influence plate behaviour. At the heart of this exploration lies the long-term

aim to better understand how each deformation mechanism influences plate behaviours, and to look to alternatively constrain rheological parameters by comparing modelled plate behaviours with real-world observations. I hope to discern which parameters align with natural tectonic processes and which might be beyond the realms of realistic geodynamics and therefore help to constrain the parameter space of the rheological models.

1.3.2 The role of a volcanic arc in back-arc extension

Even though BABs are all referred to as 'back'-arc basins, most of them were formed by breaking volcanic island arcs apart, leaving a remnant arc on the other side of the basin, such as Lau Basin which was formed by splitting Tonga Ridge and Lau Ridge apart (Zellmer and Taylor, 2001), Havre Trough between Kermadec Ridge and Colville Arc, Mariana Trough between Mariana Arc and West Mariana Ridge, etc. This phenomenon demonstrates that the presence of a volcanic arc can be important for constraining the location of extension, but few studies have taken this into account (Baitsch-Ghirardello et al., 2014).

In Chapter 5, I introduce a hot region that simulates a thermal volcanic arc on the OP and investigate its role in back-arc extension. I test the properties of the hot region and plate ages and aim to look into how an arc influences back-arc extension and its position. By this work, I wish to answer these questions: Must the extension happen at the arc? What combinations of arc properties lead to an extension at the arc? Are the models consistent with the reality?

1.3.3 Driving mechanism of back-arc extension

An important aim of this thesis is to further the understanding of the driving mech-

anism of back-arc extension. My models are limited by being 2D. However, avoiding the influence of the third dimension, the 2D driving forces can be nicely observed and explained. Based on all the parameters I have tested, a relatively complete driving mechanism can be built and how the parameters influence it can be discussed.

1.3.4 Outline of the thesis

In Chapter 2, I introduce the method of the whole thesis, including the governing equations, introduction of composite rheology and fundamental model setup. Chapter 3 provides foundational models for this thesis, presenting a reference model (RM) and a reference regime diagram of initial plate ages by testing the initial ages of the plates at the trench. The coupling strength between the overriding and subducting plates is also tested for reasonable values of RM. Chapter 4 discusses how variations in the parameters of deformation mechanisms impact the deformation of overriding and subducting plates by varying activation energy (E) and prefactor (A) in diffusion, dislocation and Peierls creeps, as well as friction coefficient (fc) and maximum yielding strength (yld_{max}) in yielding deformation. In Chapter 5, a hot region is introduced into the OP to mimic a volcanic arc. The influence of the properties of the 'arc' is investigated to better understand the role of an arc in back-arc extension. Finally, in Chapter 6, I summarise and conclude the work in this thesis, point out the limitations of my models, and then consider possibilities for future work.

Chapter 2

Methodology

2.1 Model setup

Based on the work of Garel et al. (2014), a series of 2D thermally-driven subduction models are run using the code Fluidity, a computational modelling framework suitable for geodynamic models. Fluidity is very capable which uses an adaptive unstructured mesh that can be optimised dynamically (Davies et al., 2011). It allows simulations in one, two, and three dimensions and multiple materials to be considered. But it does not have a visco-elastic capability. It provides a higher resolution in the region where the fields are changing most quickly spatially and a lower resolution in the regions where the field of the prognostic variable is stable and hardly changing. For example, in this 2D subduction model in a domain of 10000 km by 2900 km, adaptivity allows the model to have grid spacing ranging from 400 m near the subduction zone interface between the subducting plate (SP) and overriding plate (OP), to 200 km in more quiescent regions in the deepest mantle. The grid adapts throughout the simulation, keeping the finest resolution where the spatial gradients of fields (viscosity, second invariant strain rate, temperature and weak zone phase amount) are highest. It is a significant

advantage in that it retains the accuracy of the solution while reducing the calculation effort. I've made a conscious choice to make these models 2D, and to be homogeneous to keep the model simple.

A 2D thermo-mechanical model of the subduction system was built with a juxtaposed SP and OP by Garel et al. (2014). The model has a large domain to reduce the influence of boundary conditions, which is 10000 km in length and 2900 km (the whole mantle depth) in depth (Figure 2.1), and a thin weak layer, with lower maximum composite viscosity and lower friction coefficient, lies on the SP and decouples the two plates to encourage the subduction of the SP. In the initial condition, the SP is set to bend beneath the OP with a radius of curvature of 250 km (Buffett and Heuret, 2011), and the depth of the tip of SP is 194 km, that is, the SP has already started subduction at the beginning of the model. In this way, the problem of subduction initiation is avoided. The two corners on the top surface represent ridges of the two plates, where the initial age is 0 Ma. The intersection of the plates is the position of the trench, where I set the initial age of plates as Age^0_{SP} and Age^0_{OP}. I note the initial ages of the plates at the two top corners are zero. The initial ages of plates have a linear change horizontally from 0 to Age^0_{SP} and Age^0_{OP}. Velocity boundary conditions are free-slip on the bottom and the two sides, whereas the top boundary has a free surface (Kramer et al., 2012).

2.2 Governing equations

The governing equations of mantle convection follow the conservation law of mass, momentum and energy (The relevant parameters are shown in Table 3.1 in Chapter 3). I solve the simplest set of equations by assuming an incompressible mantle and the Boussinesq approximation (McKenzie et al., 1974). The momentum and continuity

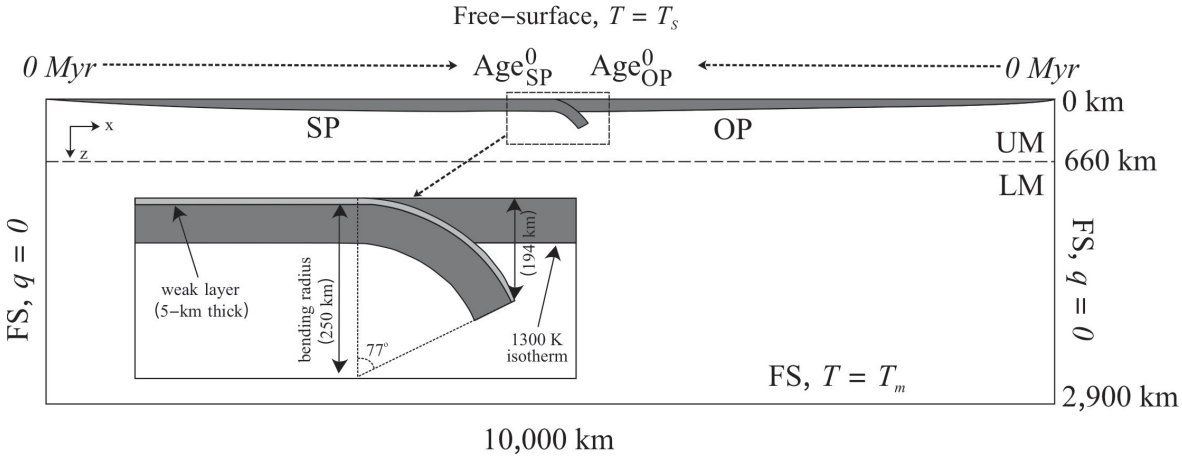

Figure 2.1: Setup and initial geometry of the subduction simulations (adapted from Garel et al. 2014).

equations are

$$\partial_i u_i = 0, \tag{2.1}$$

$$\partial_i \sigma_{ij} = -\Delta\rho g_j = \alpha\rho_s \left(T - T_s\right) g_j, \tag{2.2}$$

and the evolution of the thermal field follows:

$$\frac{\partial T}{\partial t} + u_i \partial_i T = \kappa \partial_i^2 T, \tag{2.3}$$

In these three equations, κ denotes the thermal diffusivity, u_i and g_j are the vectors of velocity and gravity (which is oriented vertically downwards), respectively, In the $\Delta\rho$ (density anomaly term), T is the temperature, T_s is the temperature at the Earth's surface and ρ_s is the nominal density at T_s, α is the coefficient of thermal expansion, and σ_{ij} is the full stress tensor which can be decomposed into deviatoric and lithostatic components, according to

$$\sigma_{ij} = \tau_{ij} - p\delta_{ij}, \tag{2.4}$$

with τ_{ij} is the deviatoric stress tensor, p is dynamic pressure, and δ_{ij} is the Kronecker delta function.

τ_{ij} the deviatoric stress tensor and $\dot{\varepsilon}_{ij}$, the strain rate tensor are related by μ, the viscosity.

$$\tau_{ij} = 2\mu\dot{\varepsilon}_{ij} = \mu\left(\frac{\partial u_i}{\partial x_j} + \frac{\partial u_j}{\partial x_i}\right), \tag{2.5}$$

2.3 Rheology

I employ a composite viscosity model that integrates four distinct deformation mechanisms. The computational domain is uniformly governed by consistent rheological laws, eliminating any compositional boundary between slab and mantle materials. This methodological choice implies that the age of the tectonic plates dictates both their buoyancy and strength, as these properties are functions of temperature-dependent density, viscosity, and thickness. This approach contrasts with the compositional or multimaterial methods, where buoyancy and strength are only interlinked through thickness, allowing for independent variations. In this study, 'strength' refers to the resistance of a plate to deformation. This resistance is quantified as the product of effective viscosity and thickness in scenarios involving uniaxial stretching or compression, and as the product of effective viscosity and thickness cubed in bending scenarios, following the framework established by Ribe (2001). In my simulations, the strength of the plates and the surrounding mantle varies both spatially and temporally.

The four deformation processes of rocks are diffusion creep, dislocation creep, Peierls creep, and yielding. The first two mechanisms dominate the deformation at a high temperature, and the diffusion creep is important in a low-stress environment, while the dislocation creep is most significant under a high-stress. All of them are temperature-

dependent except yielding viscosity, and they have the following generic relationship with temperature, stress, activation energy, the prefactor, and strain rate:

$$\mu_{diff/disl/P} = A^{-\frac{1}{n}} exp\left(\frac{E+PV}{nRT_r}\right)\dot{\varepsilon}_{II}^{\frac{1-n}{n}}, \tag{2.6}$$

In this equation, A is a prefactor, n is the stress exponent with a value of 1, 3.5 and 20 for diffusion, dislocation and Peierls creep, respectively; E is the activation energy; P is the lithostatic pressure, given by P=$\rho_s$gz, ρ_s is the reference density at the Earth's surface temperature T_s, g is the gravity and z is the depth; V is the activation volume, R is the gas constant, and $\dot{\varepsilon}_{II}$ is the second invariant of the strain rate tensor. I note that I am modelling Peierl's creep using a power-law approximation as done by Čížková and Bina (2013) and Garel et al. (2014), and not using other basic equations for the mechanism as given for example in Karato et al. (2001). Temperature (T), on which the rheology of slabs and mantle most depend, is given initially as

$$T\left(x,z,t=0\right) = T_s + \left(T_m - T_s\right) erf\left(\frac{z}{2\sqrt{\kappa Age^0\left(x\right)}}\right), \tag{2.7}$$

where z is the depth, x is the horizontal coordinate, and t is the time, T_s the temperature at Earth's surface and T_m the mantle temperature. T_r in Eq. 2.6 is the temperature in Eq. 2.7 adding an adiabatic gradient of 0.5 K/km in the upper mantle and 0.3 K/km in the lower mantle (Fowler et al., 1990). Note that I will run models with ages up to 200 Myrs, this form gives increasing continuing negative buoyancy. Many researchers argue that a plate model would better represent the lithosphere at old ages than the half-space model applied here. I do not enter that debate here, and choose this as a simple form to have variation in models. Better understanding this point would be important when wanting to compare the results with observation.

In addition, the yielding viscosity is given by

$$\mu_y = \frac{\tau_y}{2\dot{\varepsilon}_{II}}, \tag{2.8}$$

with τ_y the yield strength:

$$\tau_y = min\left(\tau_0 + fc * P, \tau_{y,max}\right), \tag{2.9}$$

τ_0 is the surface yield strength, fc is the friction coefficient (0.2), P is the lithostatic pressure, and $\tau_{y,max}$ is the maximum yield strength. The friction coefficient of 0.2 in my models is intermediate between lower values of previous subduction models (Di Giuseppe et al., 2008; Crameri et al., 2012).

The composite viscosity is based on the combination of these mechanisms via

$$\mu = \left(\frac{1}{\mu_{diff}} + \frac{1}{\mu_{disl}} + \frac{1}{\mu_y} + \frac{1}{\mu_P}\right)^{-1}. \tag{2.10}$$

This is assuming that the strain rates of all 4 deformation processes sum, as is the case for viscous dashpots in series (Schmeling et al., 2008). There are 2 materials set in these models, and the whole domain is controlled by similar rheological laws in both of them. The second material is in a weak (5-km thick) layer upon the SP tracked down to 194 km depth, and graded out below 200 km depth. It has the same parameters as the other material covering virtually the whole domain, other than it has a very low friction coefficient (fc_{weak}), and a lower maximum yielding strength to ensure the decoupling between the subducting and overriding plates. These two parameters will be tested in Chapter 3 and reasonable values will be chosen for a reference model, which provides reference parameter values for the following testing and comparison. The parameters and geometry of the fundamental model setup for the reference model will also be described in Chapter 3.

Chapter 3

Reference model

3.1 Introduction

A reference model is commonly used in numerical modelling. It acts as a benchmark, offers a basis for comparison and evaluation of new models, and ensures the reliability and accuracy of simulations. To better understand the driving mechanism and the factors which influence back-arc extension, many parameters will be investigated in this thesis, but the other parameters should be kept fixed. Therefore, the values of these fixed reference parameters are needed.

This chapter aims to provide such a reference model for this thesis and explore the subduction geodynamics of the related models fundamental to my research. Thus, I test the parameters of the coupling strength at the plate interface to make sure that the subduction goes steadily and the plates behave normally. Then I investigate the combinations of the initial plate ages at the trench (Age^0_{SP} and Age^0_{OP}) and get a regime diagram showing the threshold between 'no extension on the OP' and 'OP extension'. This will be the reference diagram for further comparison in Chapters 4 and 5.

3.2 Model setup

A 2D thermo-mechanical model of the subduction system was built with a juxtaposed subducting plate (SP) and overriding plate (OP) by Garel et al. (2014). The model has a large domain to reduce the influence of boundary conditions, which is 10000 km in length and 2900 km (the whole mantle depth) in depth (Figure 3.1), and a thin weak layer with low viscosity lies on the SP and decouples the two plates to encourage the subduction of the SP. In the initial condition, the SP is set to bend beneath the OP with a radius of curvature of 250 km, and the depth of the tip of SP is around 194 km (Garel et al., 2014), that is, the SP has started subducting at the beginning of the model. In this way, the problem of subduction initiation is avoided. The two corners on the top surface represent ridges of the two plates, where the initial age is 0 Ma. The intersection of the plates is the position of the trench, where I set the initial age of plates as Age^0_{SP} and Age^0_{OP}. The initial ages of plates have a linear change horizontally from 0 to Age^0_{SP} and Age^0_{OP}. Velocity boundary conditions are free-slip on the bottom and the two sides, whereas the top boundary has a free surface (Kramer et al., 2012). All the parameters of the model setup are listed in Table 3.1.

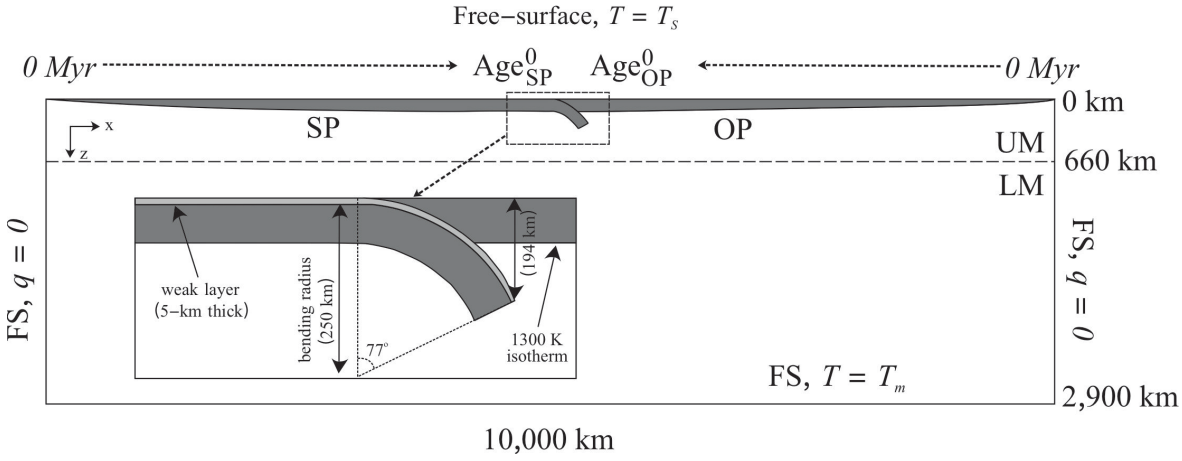

Figure 3.1: Setup and initial geometry of the subduction simulations (adapted from Garel et al. 2014). Note that it has been shown in Chapter 2, but also shown here for easier reading.

Table 3.1: Key parameters used in the reference model.

Quantity	Symbol	Units	Value
Gravity	g	$m\ s^{-2}$	9.8
Thermal expansivity coefficient	α	K^{-1}	3×10^{-5}
Thermal diffusivity	κ	$m^2\ s^{-1}$	10^{-6}
Reference density	ρ_s	$kg\ m^{-3}$	3300
Cold, surface temperature	T_s	K	273
Hot, mantle temperature	T_m	K	1573
mantle geothermal gradient	G	$K\ km^{-1}$	0.5 (UM)
			0.3 (LM)
Gas constant	R	$JK^{-1}\ mol^{-1}$	8.3145
Maximum viscosity	μ_{max}	Pa s	10^{25}
Minimum viscosity	μ_{min}	Pa s	10^{18}
Age^0_{SP}	Age^0_{SP}	Ma	90
Age^0_{OP}	Age^0_{OP}	Ma	20
Diffusion Creep			
Activation energy	E	$kJ\ mol^{-1}$	300 (UM)
			200 (LM)
Activation volume	V	$cm^3\ mol^{-1}$	4 (UM)
			1.5 (LM)
Prefactor	A	$Pa^{-n}\ s^{-1}$	3.0×10^{-11} (UM)
			6.0×10^{-17}
	n		1
Dislocation Creep (UM)			
Activation energy	E	$kJ\ mol^{-1}$	540
Activation volume	V	$cm^3\ mol^{-1}$	12
Prefactor	A	$Pa^{-n}\ s^{-1}$	5.0×10^{-16}
	n		3.5
Peierls Creep (UM)			
Activation energy	E	$kJ\ mol^{-1}$	540

Activation volume	V	$cm^3\ mol^{-1}$	10
Prefactor	A	$Pa^{-n}\ s^{-1}$	10^{-150}
	n		20
Yield Strength Law			
Surface yield strength	τ_0	MPa	2
Friction coefficient	fc		0.2
	fc_{weak}		0.02 (weak layer)
Maximum yield strength	yld_{max}	MPa	10000
	yw_{max}	MPa	10000 (weak layer)

3.3 Reference model

Fixed Age^0_{SP} and Age^0_{OP} to 90 and 20 Ma, respectively, and the friction coefficient of the weak layer over the SP to 0.02, a reference model (RM) is run, whose parameters are listed in Table 3.1. Figure 3.2 shows its evolution of temperature, viscosity, dominant deformation mechanism, horizontal stress and velocity for 46 Myrs. At the beginning, the SP sinks rapidly and reaches the boundary between the upper mantle (UM) and lower mantle (LM) at about 4 Ma after model initiation. I note that the SP sinking velocity in this short time period increases to a very high value (with a local peak of about 38 cm/yr, and a lower peak when averaged over 1 Myr [geologically observable timeframe], as expected, as the length of the driving subducting slab increases, before decreasing to nearly steady values of less than 2 cm/yr once the slab approaches and enters the more viscous lower mantle. During the time of rapid sinking, the OP basement near the trench is thinned by the mantle wedge flow (Figure 3.2a, e), and the region that is about 750 km away from the trench (far-field location) on the OP becomes thinner. These thinning regions are under extensional stress (Figure 3.2d). After the SP tip reaches the LM which is more viscous compared to the UM, its

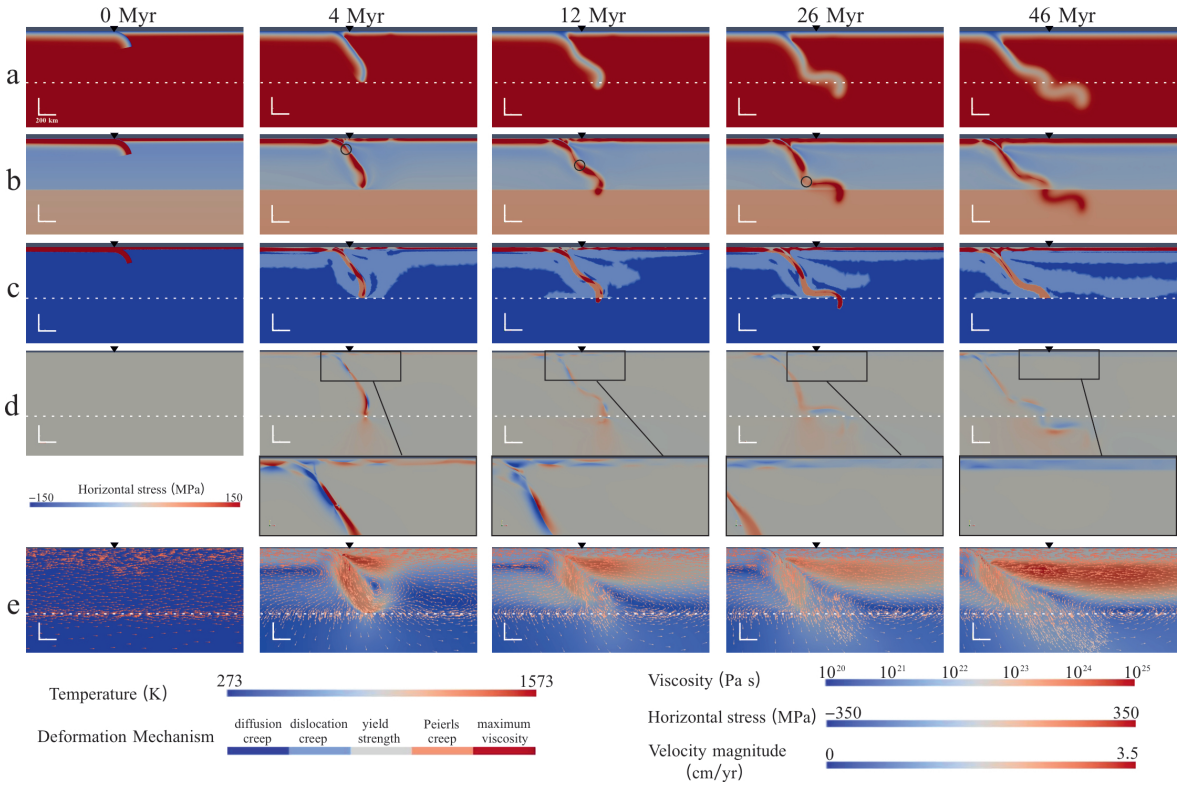

Figure 3.2: Simultaneous snapshots of a zoom-in of the reference model showing the time evolution of different fields. (a) Temperature field, (b) viscosity field, (c) dominant deformation mechanism, (d) horizontal stress (positive value indicates extensional stress), and (e) the magnitude of velocity field with arrows. The black lower triangles mark the initial trench positions, and the dashed line represents the boundary of the upper mantle (UM) and the lower mantle (LM). The small black circles mark 'bending knee' in b.

subduction slows down due to the resistance provided by the viscous LM, which means the subduction process turns to a steady state (Capitanio et al., 2007). Meanwhile, the SP at the trench keeps subducting by negative buoyancy force and the slab is not rigid enough to keep straight so the middle of the slab starts to bend up. The bending knee (this location of weakness in the SP which migrates with subduction is called the 'bending knee' in this thesis, Figure 3.2b) continues to descend with time, while the leading part of the SP flattens at the transition zone. The thinning regions near the trench and at the far-field location both cool down as the model evolves towards the steady state, at which time the whole OP is under a compressional environment. It is

noted that the trench retreats all the time even though the rate changes in the RM.

In the next sections, we start with the definition of Extension, and the initial plate ages at the interface and the degree of plate interface coupling (by changing the friction coefficient of the weak layer over the SP) are tested for getting a reasonable value. The results explain the reason why these parameters are chosen in the RM.

3.4 Definition of Extension

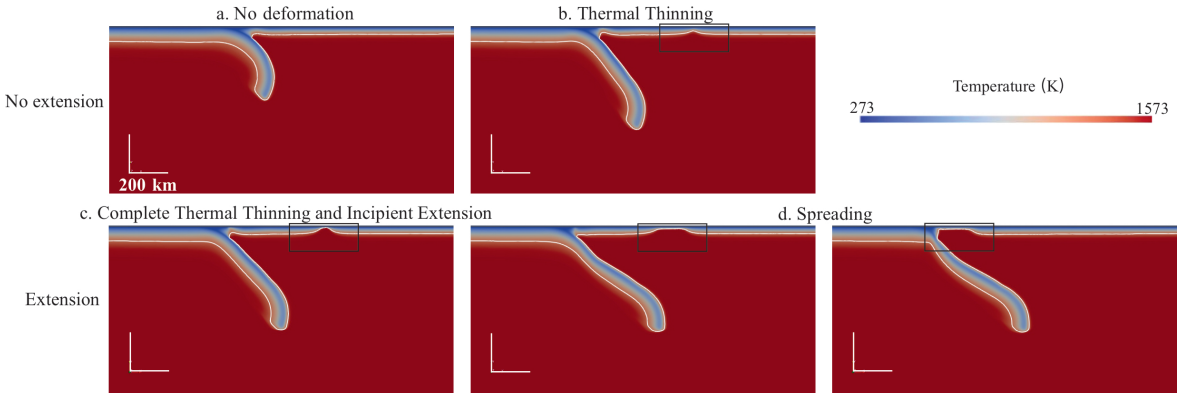

Figure 3.3: Definition of the extension levels by the isothermal contour of 1300 K (the white line). The temperature fields show (a) No deformation, (b) Thermal Thinning, (c) Complete Thermal Thinning and Incipient Extension and (d) Spreading (far-field spreading on the left and near trench spreading / hot-region spreading on the right). (a) and (b) are classified as 'No Extension', whereas (c) and (d) are classified as 'Extension'. Note that these snapshots are from different simulations, they are presented here only to visualise the definition of the different extension levels.

The extension levels on the OP are illustrated by the isothermal contour of 1300 K (Figure 3.3). The contour curving up means the OP is thinned in thermal structure, which is defined as 'Thermal Thinning' (Figure 3.3b). When the contour curve visually reaches the cold thermal surface, the OP finishes thinning (Complete Thermal Thinning, Figure 3.3c) and turns to spread (Figure 3.3d) which is named 'Spreading'. The stage when the Thermal Thinning is completed is the critical point between Thermal Thinning and Spreading and is regarded as the Incipient Extension, after that

the extensional state begins. Thus, I introduce two new classifications 'Extension' and 'No Extension' identified by capitalisation, where I classify Complete Thinning and Spreading as 'Extension' and the states before Complete Thinning as 'No Extension'. The definition of Extension applies to the entire thesis.

3.5 Coupling strength between two plates

The subduction interface is a shear zone between the two plates in a subduction zone, and the degree of its lubrication determines how easily the slab subducts. The materials at the subduction interfaces vary a lot in different subduction zones and change over geological time, which influences the subduction and plate behaviours (Behr et al., 2022). To lubricate the plate interface and make sure the subduction happens, a 5-km thick weak layer over the SP is introduced into my model. To test the influence of coupling between plates on OP deformation and get a reasonable value for these models, the yield strength of the weak layer on the top of the SP (Figure 3.1) was varied. The maximum yield strength (yw_{max}) was varied from $1{\times}10^{7}$ to $1{\times}10^{11}$ Pa, and the friction coefficient (fc_{weak}) is from 0.001 to 0.1 (Table 3.2).

There are 5 modes identified in this series of models. (a) No Extension on the OP, the SP subducts steeply and the trench retreats gradually (N, Figure 3.4a); (b) OP Extension, the SP subducts with a much lower angle than in Mode N, the trench also keeps retreating all the time as the same as Mode N, but with a higher rate (E, Figure 3.4b); (c) OP Extension, the SP subducts with medium angle and trench retreats fast at the beginning, but the trench movement turns towards the OP (Advances) a couple of million years after the extension, and the angle of SP increases (EA, Figure 3.4c); (d) the initial evolution is similar to Mode EA (OP Extension and trench Advancing), but after the trench advances, the SP Detaches and sinks into the lower mantle (EA-D,

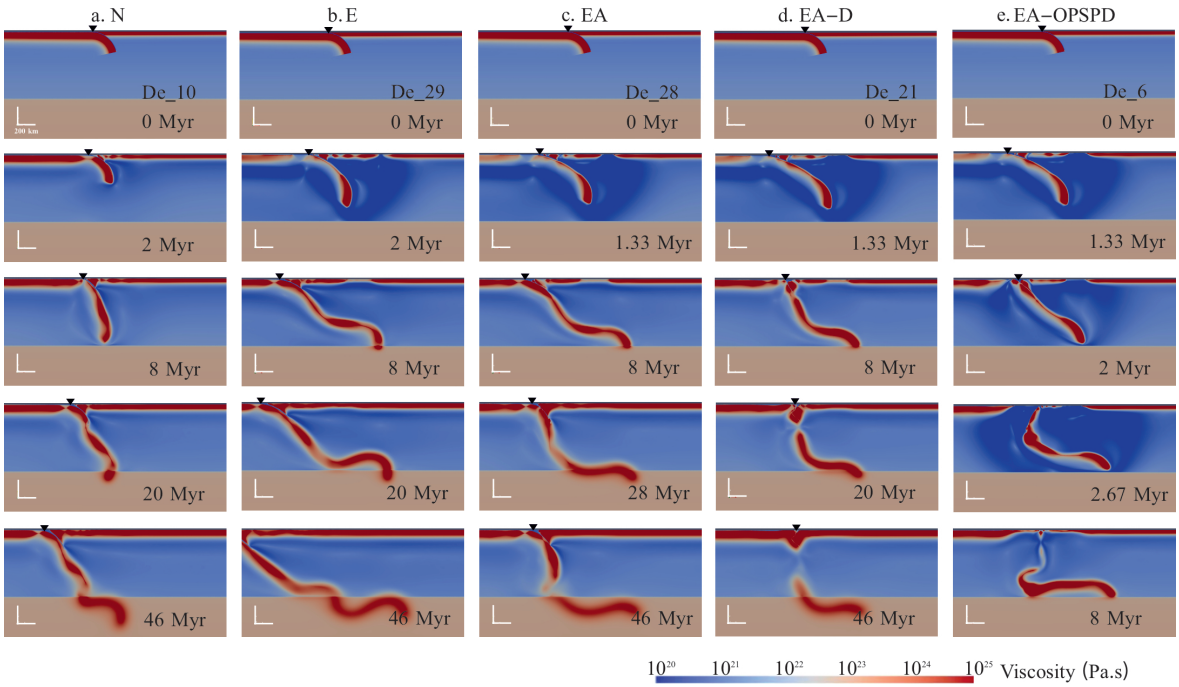

Figure 3.4: Example cases of the deformation modes illustrated using maps of viscosity field (by decoupling the plate interface). They are shown to define the different modes. (a) Mode N (model De_10), there is No extension on the OP; (b) mode E (model De_29), there is Extension on the OP; (c) mode EA (model De_28), Extension on the OP and the trench Advances; (d) mode EA-D (model De_21), Extension on the OP and the trench Advances, after a while the slab Detaches from the entire SP; (e) mode EA-OPSPD (model De_6), Extension on the OP and the trench Advances, then the OP part between the extension and the trench sinks following the broken-off SP and Detaches as well. The black triangles mark the initial trench positions. The evolution of each case is shown as a vertical column for a clearer view of the trench position.

Figure 3.4d); (e) this mode undergoes the similar process to mode EA and EA-D at the beginning, but the part of OP between the extension and the trench Detaches following the detached subducting slab quickly, the slab and a part of OP both Detaches and sinks into the LM (EA-OPSPD, Figure 3.4e).

Most models which have relatively low yield strength (decreased fc_{weak} and yw_{max}) of the weak layer show Extension on the OP, and all these extensions are located at the far-field location. The main differences among the modes are the trench motion and the SP behaviour. When the yield strength of the weak material is decreased, which encourages the plates to decouple, the trench advance and slab detachment are shown

in models (Figure 3.5). There is also an OP section breaking off with the slab when the fc_{weak} is low to 0.002.

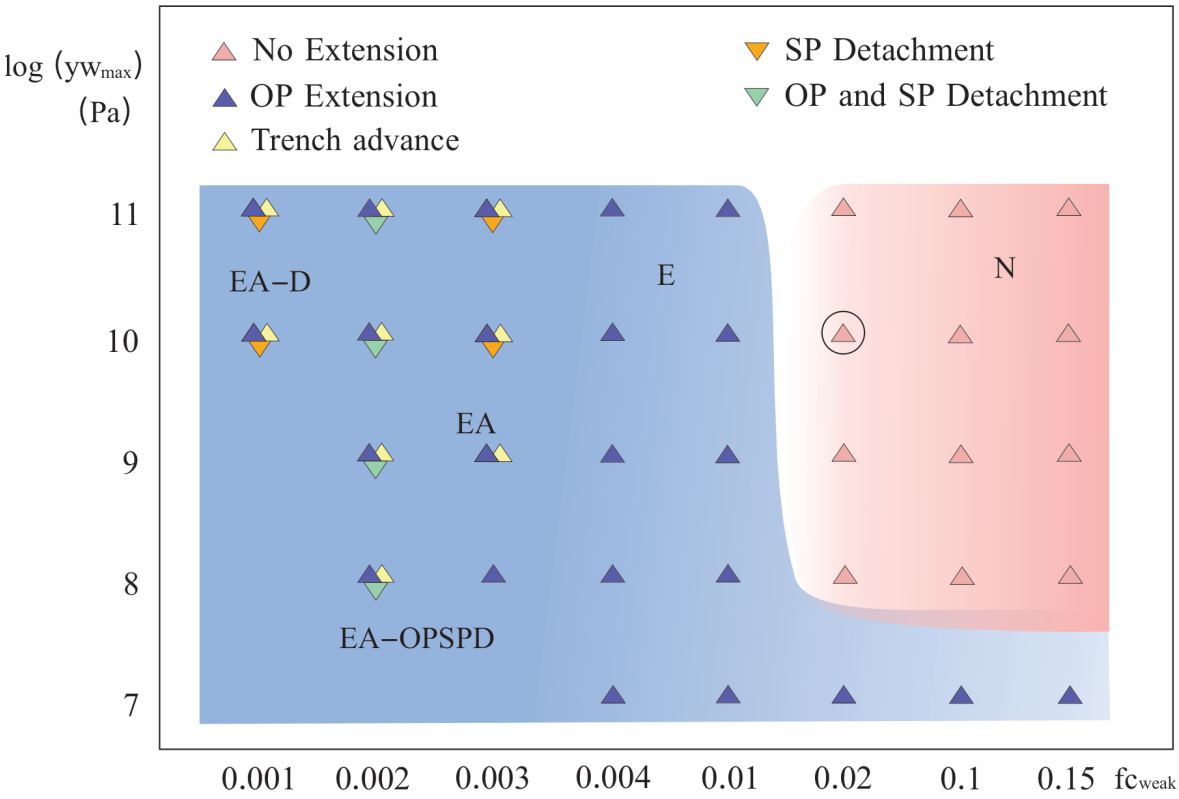

Figure 3.5: The regime diagram of the maximum yield strength (yw_{max}) and friction coefficient (fc_{weak}) of the weak layer. The plate behaviours are represented by upper and lower triangles in different colours. No lower triangle on the mark means that there is no SP detachment in this case. The reference model (RM) is marked as a circle in the diagram.

In this section, I only varied the friction coefficient (fc_{weak}) of the weak layer at the plate interface, which cannot simulate the properties of real rocks. Thus, a detailed analysis of the coupling strength is beyond this test. According to these results, the fc_{weak} value of 0.02 and the yw_{max}) value of 10,000 Pa (1×10^{10}) has been chosen in the models in the rest of the thesis because they give reasonable behaviours and are similar to Garel et al. (2014).

Table 3.2: Models of changing parameters of Yield Strength of the weak layer.

fc_{weak} / yw_{max} (MPa)	0.001	0.002	0.003	0.004	0.01	0.02	0.1	0.15
1.0×10^{11}	De_21	De_22	De_30	De_32	De_24	De_25		
1.0×10^{10}	De_16	De_31	De_17	De_18	De_19	RM		
1.0×10^{9}		De_11	De_28	De_12	De_29	De_15		
1.0×10^{8}		De_6	De_27	De_7	De_8		De_10	
1.0×10^{7}				De_1	De_2	De_3	De_5	De_26

* RM (Reference Model) and the models used in Figure 3.4 are marked in red.

3.6 Combinations of initial plate ages adjacent to the trench

The initial plate ages at the trench (Age^0_{SP} and Age^0_{OP}) play an important role in plate behaviours in a subduction system because they control the thermal structure of the plates according to equation 2.7, which controls many properties of a plate. As the ages go up, the plates become increasingly cold, thick, and strong. Varying combinations of Age^0_{SP} and Age^0_{OP} produce different effects on plate behaviours (Garel et al., 2014).

3.6.1 Regime diagram for back-arc extension

The results, showing whether there is Extension on the OP, as a result of changing the Age^0_{SP} and Age^0_{OP} in models with trench rollback are shown in Figure 3.6. The figure reveals that an older Age^0_{SP} tends to result in Extension when Age^0_{OP} remains

unchanged, whereas a younger Age^0_{OP} provides an equal effect when Age^0_{SP} is fixed. Specifically, when Age^0_{OP} is prescribed to be 20 Ma, the threshold of the SP age that leads to Extension is 100 Ma (Model SP100_OP20), and a little bit of thinning occurs at the place where the extension exists in SP100_OP20 if the Age^0_{SP} is decreased to 90 Ma (Model SP90_OP20, the same as RM). I change Age^0_{OP} in steps of 5 Myrs and find the minimum Age^0_{SP} to generate Extension for each Age^0_{OP}. As seen in Figure 3.6, models SP70_OP15, SP100_OP20, SP170_OP25, and SP280_OP30 are the marginal cases in the region in which the models have Extension. As Age^0_{SP} increases from 70 Ma to 280 Ma, the time before the extension occurs gets slightly longer, from 2.7 Ma to 4.7 Ma. For these three models, increasing the Age^0_{OP} or decreasing the Age^0_{SP} stops the extension. The extension does not last very long in the cases represented by the purple squares in Figure 3.6. Extension or Thinning in all models heals in the steady state mentioned in Section 3.3, which is always after a few million years from model initiation. The plate_age_diagram is also the Reference Diagram, which is shown as a comparison in Chapter 4 and 5.

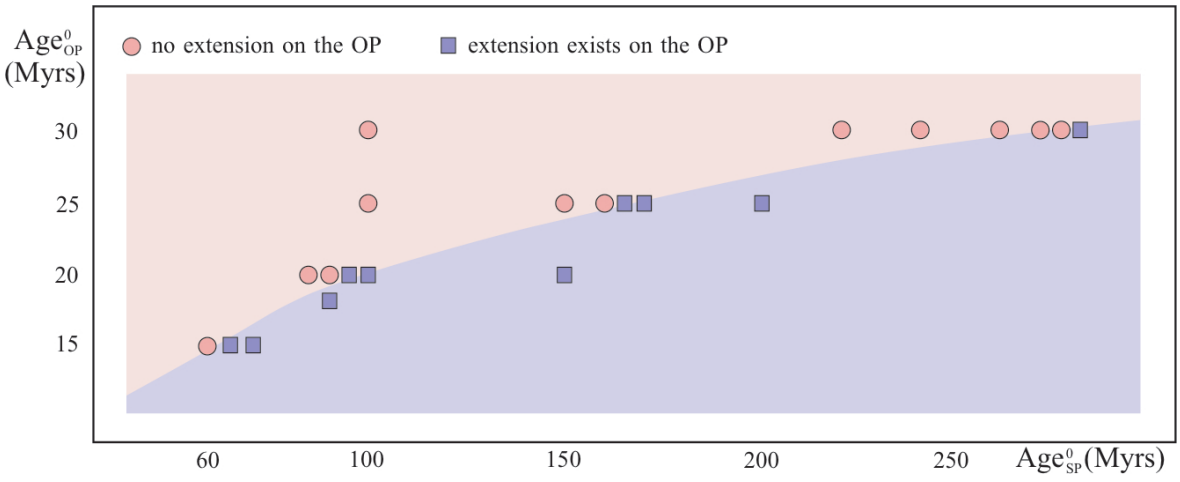

Figure 3.6: Regime diagram resulting from varying the initial plate ages based on the reference model.

3.6.2 Correlation to the trench retreat rate and SP sinking rate

The models where the initial age of OP is changed, while the Age^0_{SP} value is kept fixed at 100 Myrs (Figure 3.6) are chosen to investigate the influence on the trench retreat rate and the SP sinking rate of the Age^0_{OP}. The Age^0_{OP} varies from 15 to 30 Myrs (this age straddles extension - no extension for the Age^0_{SP} investigated). The effect of the Age^0_{SP} is also tested by the models with the Age^0_{OP} value of 25 Myrs, the range of the Age^0_{SP} is from 100 to 200 Myrs.

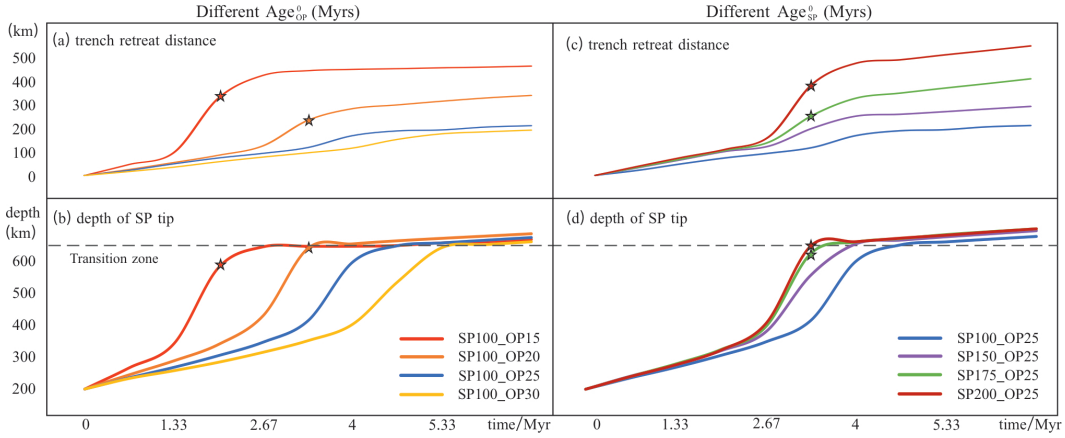

Figure 3.7: Comparisons of total (a) (c) trench retreat and (b) (d) depth of SP tip subduction throughout the first 6 Myr simulation with various Age^0_{OP} (a, b) and different Age^0_{SP} (c, d), respectively. The grey dashed line represents the transition zone depth (660 km). The stars mark the time when the Extension occurs in each model, and the colour of the stars is the same as the lines of each model.

When the Age^0_{OP} decreases, the general trench retreat rate rises markedly, which can be seen by the gradient of the distance-time plots (Figure 3.7a). The vertical SP sinking rate accelerates earlier as Age^0_{OP} decreases, and the SP tip takes less time to get to the transition zone although the maximum rates of the models are close (Figure 3.7b). When the Age^0_{SP} rises, both the SP rate and trench retreat rate show the same trend as when Age^0_{OP} decreases (Figures 3.7c, d), though the increase with Age^0_{SP} is

much less than with Age^0_{OP}. The Extension occurs in the models which have a relatively high trench retreat rate.

Overall, the age of the initial tectonic plates markedly impacts the rate of trench retreat. However, this age factor appears to have a negligible effect on the SP sinking rate. It is observed that the sinking rate may be excessively high to discern any differences prior to the SP tip reaching the transition zone between the UM and LM. One notable influence of the initial plate ages on SP sinking dynamics is the occurrence of the onset of the maximum SP sinking rate.

3.6.3 Driving mechanism of Extension

To produce back-arc extension, either the driving force acting on the OP needs to increase or the OP needs to weaken. The driving force can be related to plate motions and/or subduction-induced mantle flow in a subduction zone, which can be reflected in the horizontal stress field. The weakened mechanism could be from the upwelling flow beneath the OP.

I calculated the vertically average horizontal stress (σ_h) over the OP thickness and plotted the maximum value (σ_{hmax}) on the entire OP before the stress decreased as a function of Age^0_{SP} (Figure 3.8). When the Age^0_{SP} is relatively young, the σ_{hmax} increases fast as the Age^0_{SP} rises from 50 to about 110 Myrs (Age^0_{OP}=30 Myrs). However, the σ_{hmax} does not change obviously as the Age^0_{SP} keep rising, even though when the Age^0_{SP} is greater than 270 Myrs in which models Extension occurs (Figure 3.8c). In these models, the extensional force (indicated by σ_{hmax}) does not play an essential role in back-arc extension, which implies the weakening of the OP dominates the process.

The weakening process is from the vertical component of the underneath mantle flow (shown as only a poloidal flow in the 2D models), which also contributes to basal drag by its horizontal component (Figure 3.9). Because of the mobile OP, the driving

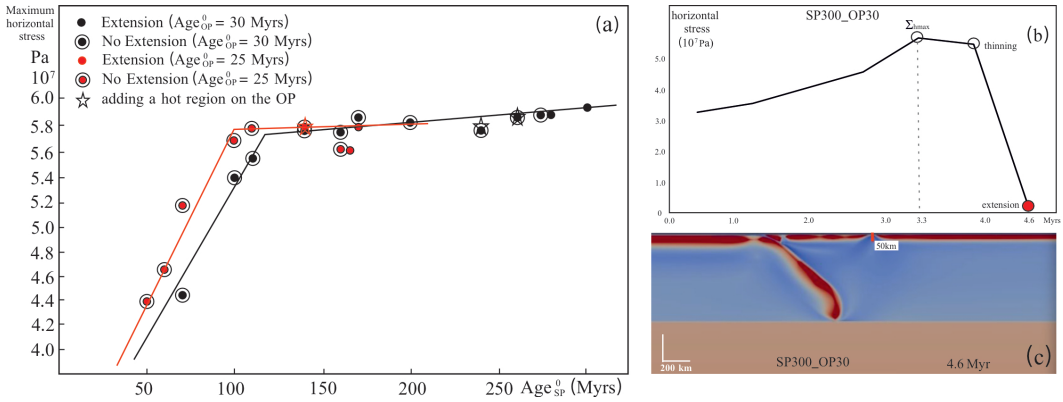

Figure 3.8: (a) Maximum vertically integrated horizontal stress (Σ_{hmax}) over OP thickness (from the surface to the OP bottom, 70 km depth when the Age^0_{OP} is 30 Myrs, which was defined by the temperature contour of 1300K.) vs. Age^0_{SP}. (b) Depicts the time evolution of vertically integrated horizontal stress (Σ_h) and (c) identifies the specific location where this stress is calculated. A positive stress value means extensional.

force from plate motions is probably limited, which indicates that the trench retreat does not generate enough pulling force. Considering the trench retreat rate has a strong correlation to Extension, the trench retreat might be one of the reasons which enhance the poloidal flow.

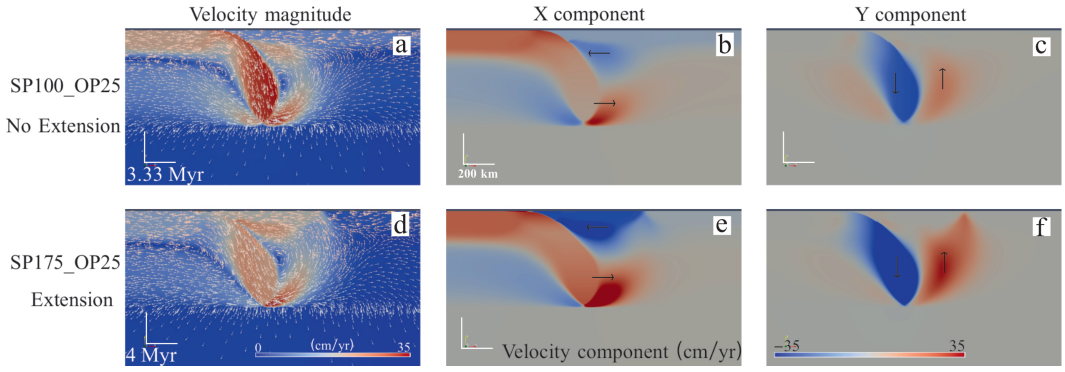

Figure 3.9: Velocity fields in 2 modes. The small arrows indicating the direction of the mantle flow are marked in the magnitude velocity field. In the velocity component field, the positive value represents rightwards (in the x component field) or upwards (in the y component field). The chosen time is when the models show the highest velocity, which is just before the Extension in case SP175_OP25.

In total, the main driving mechanism is the poloidal flow induced by the subducting slab and enhanced by the trench retreat. The trench-ward horizontal flow (X compo-

nent) produces basal drag by the velocity gradient (Figure 5.10), whereas the upwelling thermal intrusion (Y component) weakens the OP to facilitate an Extension. The upwelling flow, the cause of both components of flow, is always in a similar direction (about 60° to the horizontal) as it approaches the OP. This far-field location where the flow focuses is regarded as the edge of the flow cell in this work. The distance from the trench to the far-field extension (the horizontal size of the flow cell) is around 750 km (± 80 km), which is mainly controlled by the depth of the UM which is 660 km. The size also varies a little, which is probably a result of the varying SP dip/morphology arising from varying slab retreat rates.

The Extension process is the competition of basal drag which thins the OP versus thermal healing which thickens it (the basal drag varies beneath the OP leading to local extension). The model goes to rift when the basal drag wins out, but thermal healing is always efficient because all the Extensions heal after a few Myrs as well. The thermal weakening starts at the base of the thermal boundary between the OP and the underlying mantle, though the viscosity weakens from both the base and the top of the OP and produces 'necking' (Lei, 2022) in the middle, which is because yielding viscosity dominates at the top and it is not dependent on the temperature but on the yielding strain rate and the depth. Then the Extension appears from the base of the OP and the material flows into the gap at the surface. The detail of the effect of basal drag will depend upon the asthenosphere-lithosphere coupling, which is self-consistently solved for in my work which involves a thermal lithosphere but the basal drag could differ slightly in reality with more complex lithospheres.

From this discussion, I conclude that the primary extensional force probably arises from the basal drag, while the extension occurs when the OP is weakened.

3.6.4 Plate ages on Earth

The results show that an old SP is more likely to generate Extension in these models (Figure 3.6), which is consistent with observations in nature. For example, the East Pacific SPs are quite young at the plate interface when entering the subduction zones, corresponding to which there are few BABs found along the East Pacific margin. Specifically, the Juan de Fuca, the Explorer, the South Gorda and the Winona plates, which are along North America, are less than 10 Ma (Rogers, 1988), and the Nazca Plate which subducts beneath the South American Plate is about 40 Ma (Capitanio et al., 2011). In contrast, most western Pacific SPs are around 100 Ma (Müller et al., 2008), and there are a lot of BABs distributed along that margin. For example, the ages of consuming SPs in Shikoku and Parece Vela basin formations are 70–95 Ma and 90–115 Ma, respectively (Faccenna et al., 2009). This phenomenon meets my basic model behaviour.

A younger OP is easier to break because it is relatively thinner and warmer, which means its strength is weaker. The diagram shows that the OP is always younger than 30 Ma if there is an extension on it (Figure 3.6). Considering that very few oceanic plates on Earth are older than 170 Ma (Müller et al., 2008; Di Giuseppe et al., 2009), the OPs should be younger than 25 Ma according to the results. The Mariana subduction zone is a suitable case with both an old SP (over 150 Ma) and a young OP — the Mariana Trough is spreading in the Shikoku-Parece-Vela basins, which are less than 25 Ma when the trough started to extend (Faccenna et al., 2009). Besides, there are other young OPs such as the seafloor of the South Fiji Basin (30–15 Ma) which is the OP of the Lau Basin (Herzer et al., 2011), and the SP age was about 100 Ma when the basins started to spread (Di Giuseppe et al., 2009). However, for most subduction zones on Earth, the required Age^0_{OP}s for an extension are relatively young. The reason might be the high rheology parameters of the mantle and homogeneous material of the OP

leads to a rigid OP. In the following two chapters, the effects of rheology parameters and a weak zone on the OP will be tested, and a better comparison to the observations on Earth will be seen.

3.7 Summary

This chapter introduces a 2D thermo-mechanical model to study subduction system dynamics, focusing on the juxtaposition of the SP and OP. The chapter tests various initial conditions and parameters, including the ages of the SP and OP at the trench, and the coupling strength between the two plates by changing the friction coefficient of the weak layer over the SP. This chapter identifies key factors that influence Extension on the OP, demonstrating how older SPs tend to result in extension and the influence of younger OPs. It also explores the effects of plate coupling strength on deformation modes, revealing a spectrum of behaviours from no extension to various forms of back-arc extension and trench retreat patterns. In addition, I tested the coupling strength between plate ages by changing the friction coefficient of the weak layer over the SP, which lubricates the interface and facilitates the subduction, because the coupling strength varies a lot in reality. From this testing, I chose a set of reasonable values for the 'reference model' by requiring the SP to behave 'reasonably' and where the OP is thinned but not extended.

The primary driving mechanism of the models is the poloidal flow underneath the OP. The flow cell has almost the same size in every model, which focuses at around 750 km from the trench on the OP and gradually decreases towards the trench. A higher trench retreat rate, which is induced by an older SP or younger OP, facilitates the poloidal flow, thus encouraging back-arc extension.

The importance of this chapter is in giving a reference model (RM), a reference

diagram of the behaviour of subduction systems with different initial plate ages at the trench (Age^0_{SP} and Age^0_{OP}) for comparison to other groups of models, and a definition of Extension on the OP. These three things are used in the whole thesis. The driving mechanism of back-arc extension has been discussed and considered to be the poloidal flow induced by the trench retreat.

I have fixed the rheology parameters in my models so far, which is commonly done in numerical geodynamic models. However, rheology is an important factor in model behaviours. Thus, in the next chapter, I will investigate them further to explore their roles in plate behaviours, especially in back-arc extension.

Chapter 4

How does each rheological deformation mechanism influence plate behaviours

4.1 Introduction

Historically, the foundations of rheology have been built upon the study of the behaviour of materials when subjected to stress. It looks at how materials, under varying conditions of temperature, pressure, and composition, deform and flow. In the realm of geosciences, this translates to understanding how rocks, whether in the Earth's crust or deeper within the mantle, respond to the immense stresses they are subjected to.

Over the years, much significant work in the field of mantle rheology has shown the complexity of the rheology behaviour of mantle rocks (Karato and Wu, 1993; Hirth and Kohlstedt, 2003). The previous studies have identified various deformation mechanisms at play, each operative under different conditions and having distinct implications for

mantle flow and slab dynamics (Fadaie and Ranalli, 1990; Karato and Wu, 1993; Ranalli and Fischer, 1984; Stocker and Ashby, 1973; van Hunen et al., 2005). The intricacies of these deformation mechanisms and their role in the broader context of slab and mantle dynamics present a rich avenue for investigation.

In mantle rheology, both brittle and ductile deformation plays an important role. Brittle deformation is dominant in the cooler, upper regions of the mantle, where rocks respond to stress by fracturing, leading to the formation of faults and earthquakes. Brittle rock strength is primarily a function of pressure-depth and is essentially independent of rock type, as Byerlee's law illustrates (Byerlee, 1978). As I descend into the warmer, deeper mantle, ductile deformation becomes dominant, with rocks deforming plastically under long-term tectonic forces. The ductile regime of the mantle is a complex domain where rock strength is not a constant but a variable contingent upon several factors, such as rock type, grain size, macro- and microstructure, temperature, strain rate, and fluid content. These factors interact in a nonlinear fashion, rendering the mantle's response to deformation a function of the rate at which strain is applied. Several deformation mechanisms are working within the ductile mantle, each with its unique characteristics and dominant domain:

Diffusion Creep: This process, favoured by high temperatures and low differential stresses, involves the transfer of mass through the crystal lattice or along grain boundaries, allowing rocks to deform without fracturing. This mechanism is highly sensitive to temperature and grain size, with smaller grains facilitating a more rapid diffusion process. Diffusion creep is significant in the lower mantle (LM) and beneath mid-ocean ridges, where conditions allow for the slow, steady-state flow of rocks.

Dislocation Creep: At higher stresses and somewhat lower temperatures, dislocation creep takes over, characterised by the movement of dislocations within the crystal lattice. This mechanism allows for more substantial deformation, as dislocations move

through the grains of minerals, accommodating the shear strain. The prevalence of dislocation creep is often marked by the development of crystallographic preferred orientations, which can influence the seismic anisotropy of the mantle.

Peierls Creep: Occurring at even higher stresses, typically deep in the mantle where temperatures also remain high, Peierls creep is a mechanism where the movement of dislocations is hindered by the lattice itself, requiring significant stress to overcome this resistance. This mechanism is less well-understood but is thought to contribute to the overall strength of the mantle.

The mantle's rheological response to stress is captured in empirical flow laws derived from laboratory experiments, which often involve parameters such as activation energy and volume, stress exponent, and material constants (Burov, 2011; Chopra and Paterson, 1981, 1984; Hirth and Kohlstedt, 2003; Jain et al., 2019; Karato et al., 1986; Keefner et al., 2011; Hirth and Kohlstedt, 1996; Mei and Kohlstedt, 2000; Tielke et al., 2017). A lot of laboratory experiments show parameters of different rocks under different conditions (e.g. wet or dry), but the uncertainties cannot be ignored because they lead to a large range of parameter values. Take olivine for example, which is the major mineral in the upper mantle (UM) and often represents the mantle rheology in numerical modelling, the range of the activation energy of dislocation creep can vary from 138 kJ/mol (Jain et al., 2019) up to 535 kJ/mol under dry conditions (Chopra and Paterson, 1981). Earlier studies show larger values which are always greater than 500 kJ/mol (Chopra and Paterson, 1981, 1984; Karato et al., 1986; Hirth and Kohlstedt, 1996), while the recent works tend to report values less than 500 kJ/mol because of considering various factors (Jain et al., 2019; Keefner et al., 2011; Tielke et al., 2017). The results from the laboratory can be influenced by many factors due to the limitations of the laboratory conditions and the different scales between the laboratory and nature. For example, the experimental strain rates in the laboratory are always much bigger or-

der than in nature, which are 10^{-9}–10^{-4} s^{-1} and 10^{-18}–10^{-14} s^{-1}, respectively (Burov, 2011). Coincidentally, a higher temperature is always used for quicker deformation to avoid brittle failure in the laboratory. The boundary caused by different orders of scales is hard to be overcome. Additionally, grain size (Karato et al., 1986), water content (Karato et al., 1986; Hirth and Kohlstedt, 1996), oxygen fugacities (Keefner et al., 2011) and chemical reactions change rock strength and behaviours, but it is difficult to know the natural conditions. These show that the understanding of the rheological deformation mechanism of the mantle is still limited due to the uncertainties.

This is where my investigation finds its motivation. A group of fixed rheology parameters is extremely limited in investigating the plate behaviours, testing a larger range of values is essential for better understanding subduction geodynamics. Through this chapter, I study deep into the complexities of composite rheology, examining how diffusion, dislocation, and Peierls creep, along with yielding strength, come together to influence plate behaviour. At the heart of this exploration lies the long-term aim to constrain rheological parameters. By comparing modelled plate behaviours with real-world observations, I hope to discern which parameters align with natural tectonic processes and which might be beyond the realms of realistic geodynamics and therefore help to constrain the parameter space of the rheological models.

4.2 Rheology variables

4.2.1 Rheology equations

As described in Chapter 2, four deformation processes of rocks occurring in the slabs and mantle are considered in my models: diffusion creep, dislocation creep, Peierls creep, and yielding. The predominant mechanisms at high temperatures are diffusion and dislocation creep. Diffusion creep plays a key role in low-stress conditions,

whereas dislocation creep becomes more important under high-stress situations. All these ductile processes are influenced by temperature (T), with the exception of yielding viscosity. They exhibit a common relationship:

$$\mu_{diff/disl/P} = A^{-\frac{1}{n}} exp\left(\frac{E+PV}{nRT_r}\right)\dot{\varepsilon}_{II}^{\frac{1-n}{n}}, \tag{4.1}$$

In this equation, A is a prefactor, n is the stress exponent with a value of 1, 3.5 and 20 for diffusion, dislocation and Peierls creep, respectively; E is the activation energy, from 250 to 300 kJ/mol in diffusion creep and from 400 to 550 kJ/mol in dislocation creep of the UM, and it is smaller in the LM; P is the lithostatic pressure, given by P=$\rho_s$gz, ρ_s is the reference density at the Earth's surface temperature T_s, g is the gravity and z is the depth; V is the activation volume, R is the gas constant, and $\dot{\varepsilon}_{II}$ is the second invariant of the strain rate tensor.

In addition, the yielding viscosity is given by

$$\mu_y = \frac{\tau_y}{2\dot{\varepsilon}_{II}}, \tag{4.2}$$

with τ_y the yield strength:

$$\tau_y = min\left(\tau_y + f_c P, \tau_{y,max}\right), \tag{4.3}$$

τ_0 is the surface yield strength, fc is the friction coefficient, P is the lithostatic pressure, and $\tau_{y,max}$ is the maximum yield strength.

The composite viscosity is based on the combination of these mechanisms via

$$\mu = \left(\frac{1}{\mu_{diff}} + \frac{1}{\mu_{disl}} + \frac{1}{\mu_y} + \frac{1}{\mu_P}\right)^{-1}. \tag{4.4}$$

This is assuming that all 4 deformation mechanisms act in parallel. All the UM

Table 4.1: Key parameters of UM rheology used in the reference model.

Deformation mechanism	Quantity	Symbol	Units	Value
Diffusion Creep	Activation energy	E_{diff}	kJ mol^{-1}	300
	Activation volume	V_{diff}	cm^3 mol^{-1}	4
	Prefactor	A_{diff}	Pa^{-n} s^{-1}	3.0×10^{-11}
	Stress exponent	n_{diff}		1
Dislocation Creep	Activation energy	E_{disl}	kJ mol^{-1}	540
	Activation volume	V_{disl}	cm^3 mol^{-1}	12
	Prefactor	A_{disl}	Pa^{-n} s^{-1}	5.0×10^{-16}
	Stress exponent	n_{disl}		3.5
Peierls Creep	Activation energy	E_P	kJ mol^{-1}	540
	Activation volume	V_P	cm^3 mol^{-1}	10
	Prefactor	A_P	Pa^{-n} s^{-1}	10^{-150}
	Stress exponent	n_P		20
Yield Strength	Friction coefficient	f_c		0.2
	Surface yield strength	τ_0	MPa	2
	Maximum yield strength	yld_{max}	MPa	10000

* Quantities in the white rows are the rheology variables in this chapter.

rheology parameters used in RM are listed in Table 4.1.

4.2.2 Models investigated

For testing the effect of the parameters of each deformation mechanism on the OP deformation in a subduction zone, four sets of models were run based on the RM (SP90_OP20). The activation energy (E) and the prefactor (A) of diffusion, dislocation, and Peierls creep viscosity of the oceanic mantle have been changed systematically in every set of models (Tables 4.2, 4.3, 4.4, 4.5). As for models which investigate yielding,

the friction coefficient and the maximum yield strength are the parameters chosen to vary.

The initial plate ages are essential for plate behaviour (Section 3.6), but the initial plate ages of the reference model (Age^0_{SP} is 90 Ma, and Age^0_{OP} is 20 Ma) are not the only possibilities. Thus, the effect of plate ages under different rheology circumstances was also investigated (Tables A.1, A.2, A.3, A.4). The models that test rheology parameters show that E and A play a similar role in the viscosity, with viscosity being more sensitive to the value of activation energy. Thus, when the plate ages were tested, the only parameter which was changed was E in Diffusion, Dislocation and Peierls creep models. Due to the slight influence that y_{max} has on plate behaviours, only the friction coefficient was changed for Yielding models.

4.3 Results

4.3.1 Diffusion creep

4.3.1.1 Varying parameters of diffusion creep

By varying the parameters of the diffusion creep in the UM, the dominating deformation mechanism and the composite viscosity changes in the different models. The activation energy (E_{diff}) was varied from 250 to 320 kJ/mol, and the prefactor (A_{diff}) from 1×10^{-11} to 8×10^{-11} $Pa^{-1}s^{-1}$ (Table 4.2), otherwise the parameters of the reference model were used, see Table 3.1.

As the diffusion creep viscosity increases or decreases, both the subducting plate (SP) and the overriding plate (OP) display various behaviours (Figure 4.1). There are two end-member SP morphologies: inclined SP with relatively minor bending (Figure 4.1a); and steep (nearly vertical) SP with a strongly folding leading part which

Table 4.2: Models of changing parameters of diffusion creep.

E_{diff} (kJ/mol)	250	260	270	275	280	285	290	300	310	320
A_{diff} (Pa^{-1} s^{-1})										
1.0×10^{-11}	Diff_1	Diff_6	Diff_11	Diff_38	Diff_16		Diff_21	Diff_41	Diff_26	Diff_31
2.0×10^{-11}	Diff_2	Diff_7	Diff_12		Diff_17		Diff_22	Diff_42	Diff_27	Diff_32
3.0×10^{-11}								RM		
4.0×10^{-11}	Diff_3	Diff_8	Diff_13	Diff_39	Diff_18		Diff_23	Diff_43	Diff_28	Diff_33
5.0×10^{-11}					Diff_36		Diff_37			
6.0×10^{-11}	Diff_4	Diff_9	Diff_14		Diff_19		Diff_24	Diff_44	Diff_29	Diff_34
8.0×10^{-11}	Diff_5	Diff_10	Diff_15		Diff_20	Diff_40	Diff_25	Diff_45	Diff_30	Diff_35

* RM (Reference Model) and the models used in Figure 4.1 are marked in red.

stacks up in the transition zone (Figure 4.1e). Three degrees of OP deformation have been distinguished: no deformation (Figures 4.1a, e), thinned back-arc region (Figures 4.1b, d), and back-arc extension (Figure 4.1c). The combination of the overriding and subducting plate deformation leads to three main modes in this series of simulations, illustrated in Figure 4.1: (a) No deformation on the OP with an inclined SP (NI); (b) No deformation on the OP with a folded SP (NF); (c) OP back-arc region Extension (SP morphology changes from inclining to folding) (BE). There are also 2 transitional modes: (d) back-arc region thinned on the OP with an inclined SP (BT-I); (e) back-arc region thinned on the OP with a folded SP (BT-F). The presence of transitional modes is significant. They serve as crucial markers indicating the changing trends in deformation behaviours. Their existence provides evidence for plate behaviours not being restricted to just a few distinct modes but spanning a continuum of possible outcomes. The models shown in Figure 4.1 are all highlighted in red in Table 4.2.

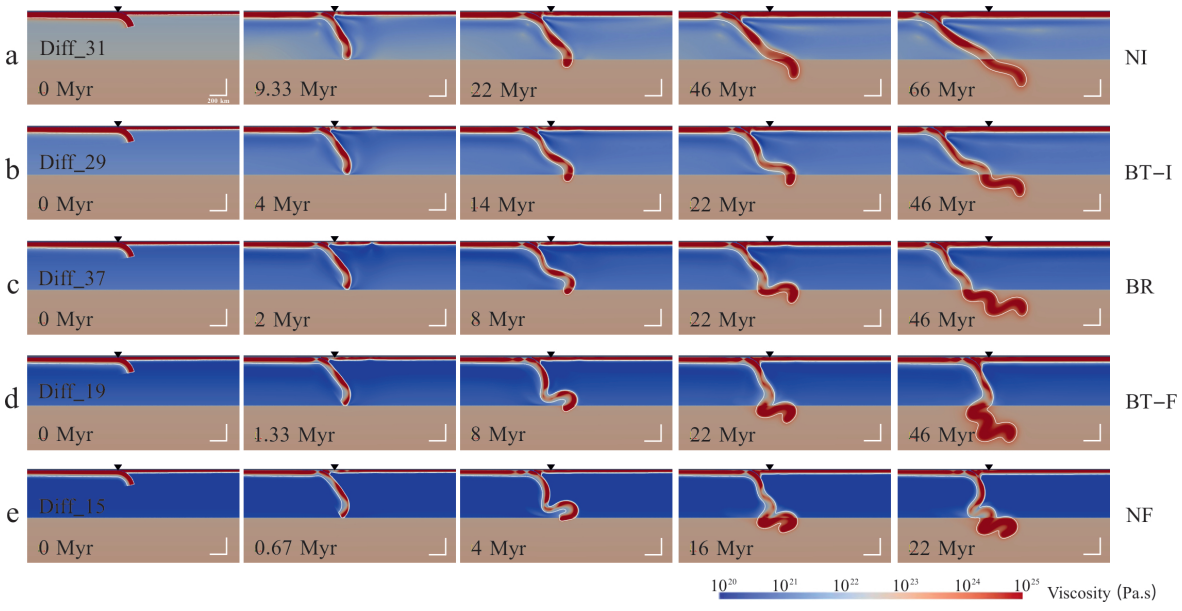

Figure 4.1: Example cases of the deformation modes illustrated using maps of viscosity field (by changing diffusion creep). (a) Mode NI (model Diff_31), (b) mode BT-I (model Diff_29), (c) mode BE (model Diff_37), (d) mode BT-F (model Diff_19), (e) mode NF (model Diff_15). The models shown here are marked by red in Table 4.2 and the rheology parameters of each model can be found in this table. The black triangles mark the initial trench positions.

Figure 4.2 shows the regime diagram for these modes. As the diffusion creep viscosity becomes stronger, the mode changes from NF, to BT-F, to BE, to BT-I, and finally to NI. Compared to the RM, which is mode BT-I in this classification, mode NI has a stronger SP, thus it has less bending after the slab tip reaches the LM than the reference model (Figure 4.1a). Models showing Mode NI also have a stronger OP than the reference model, so the OPs are harder to be broken or thinned. When the viscosity decreases the SP sinks more rapidly and tends to bend more, it deforms from inclined folding to steep folding in the transition zone. The OP also becomes weaker as the viscosity decreases. It first shows Extension in the back-arc region, then its deformation tends to vanish after the SP folding becomes increasingly steep.

4.3.1.2 Varying plate ages with various activation energy of diffusion creep ($\mathbf{E}_{diff}$)

When A_{diff} is fixed to the reference value (3×10^{-11} $Pa^{-1}s^{-1}$), the modes that models show change quickly from NF to BE, then to NI as E_{diff} increases from 270 to 310 kJ/mol. The initial plate ages were tested systematically in this range of E_{diff}, and the values were chosen every 10 kJ/mol, which are 270, 280, 290, 300, and 310 kJ/mol, respectively (Table A.1, Figure 4.3). 300 kJ/mol is the reference value of E_{diff}, and Figure 4.3d is the same as Figure 3.6 (the Reference Diagram).

As E_{diff} is reduced gradually from the maximum value (310 kJ/mol), the threshold between No deformation on the OP and OP Extension (N–E threshold) increases in Age^0_{OP} and decreases in Age^0_{SP} (Figure 4.3). The change in the N–E threshold is relatively large as the value of E_{diff} is high (from 310 to 300 kJ/mol), but when E_{diff} is less than 300 kJ/mol, the change in the N–E threshold is less. For example, there is no apparent difference between the N–E thresholds in Figures 4.3b and c. Even though the mode of OP deformation changes little when E_{diff} is reduced from 300 kJ/mol,

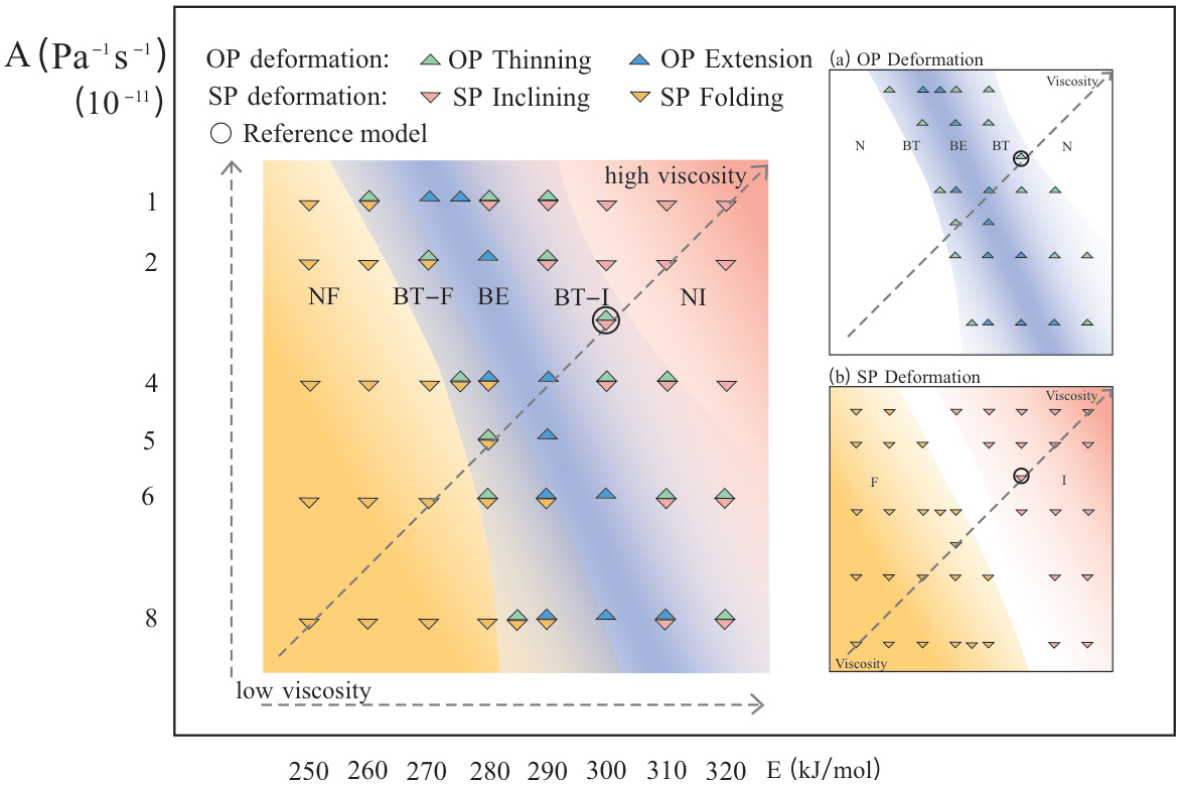

Figure 4.2: The regime diagram of E_{diff} (activation energy) and A_{diff} (prefactor) of diffusion creep viscosity. To provide clearer information, diagrams of (a) OP deformation and (b) SP deformation are shown separately. The OP deformation modes are represented by upper triangles and the SP morphologies are represented by lower triangles. No upper triangle on the mark means that there is no deformation on the OP in this case (pink and yellow domains). No lower triangle on the mark means that the SP morphology is none of the end-members but between them (some of the purple marks). The depth of each colour represents the deformation degree of each mode. For instance, the blue domain represents models which have Extension on the OP, the darker blue in the middle means the Extension occurs more easily (earlier or larger). The overlap of two colours shows that the corresponding two behaviours occur in one model. The grey dashed arrow shows the direction in which the viscosity increases. Note that I set A_{diff} decreases as it goes up the y-axis to show an upwards-increasing viscosity. The reference model (RM) is marked as a circle in the diagram.

the SP behaviour varies a lot. E_{diff} of 270 and 280 kJ/mol makes some models show SP folding instead of SP inclining when Age^0_{SP} is younger than 100 Ma. When Age^0_{SP} and Age^0_{OP} are fixed to 90 and 20 Ma, SP folding cannot induce a large enough mantle flow to encourage the back-arc extension (4.3.1), but BE is observed when the OP is very young and E_{diff} is 270 kJ/mol. It seems that the impact diffusion creep viscosity has on the SP behaviour is more significant than that on the OP deformation when

E_{diff} is between 280 and 300 kJ/mol, whereas the contrary situation happens as E_{diff} is over 300 kJ/mol. Additionally, diffusion creep viscosity has little impact on plate behaviours when Age^0_{SP} is old (e.g. 250 Ma). With this Age^0_{SP}, most models show Mode BE-I no matter how low the E_{diff} is, only a few models do not generate back-arc extension, these are when Age^0_{OP} is relatively old (30 Ma) and E_{diff} is relatively high (300 and 310 kJ/mol). The situation is almost the same when Age^0_{SP} is 200 Ma, but fore-arc extension occurs in model E310_SP200_OP25.

4.3.2 Dislocation creep

4.3.2.1 Varying parameters of dislocation creep

The UM dislocation creep is changed from the RM values, by varying the activation energy (E_{disl}, from 510 to 560 kJ/mol) and the prefactor (A_{disl}, from 2×10^{-16} to 1×10^{-15} $Pa^{-3}s^{-1}$) (Table 4.3). The models show similar behaviours of OP and SP plates, from mode BT-I to NI (Figures 4.4a, b), with increasing viscosity, to the changes seen with diffusion creep strengthening (Figures 4.1a, b).

When the dislocation creep viscosity is decreased, the modes though change in a different way from that in Section 4.3.1. An increasingly weakened SP which is produced by decreasing the diffusion creep parameters results in slab folding, whereas that produced by decreasing the dislocation creep parameters is largely weakening at the bending knee (near the trench horizontally and marked in Figures 4.4e–g). The latter process results in break-off (also called slab detachment) of the leading part of the SP at a shallow depth when the dislocation creep viscosity is low enough, which is an end-member SP behaviour in this cluster of models (Figure 4.4g). There is also a transitional morphology between SP inclining and slab break-off when the dislocation creep viscosity has an intermediate value, which shows a turning shape when

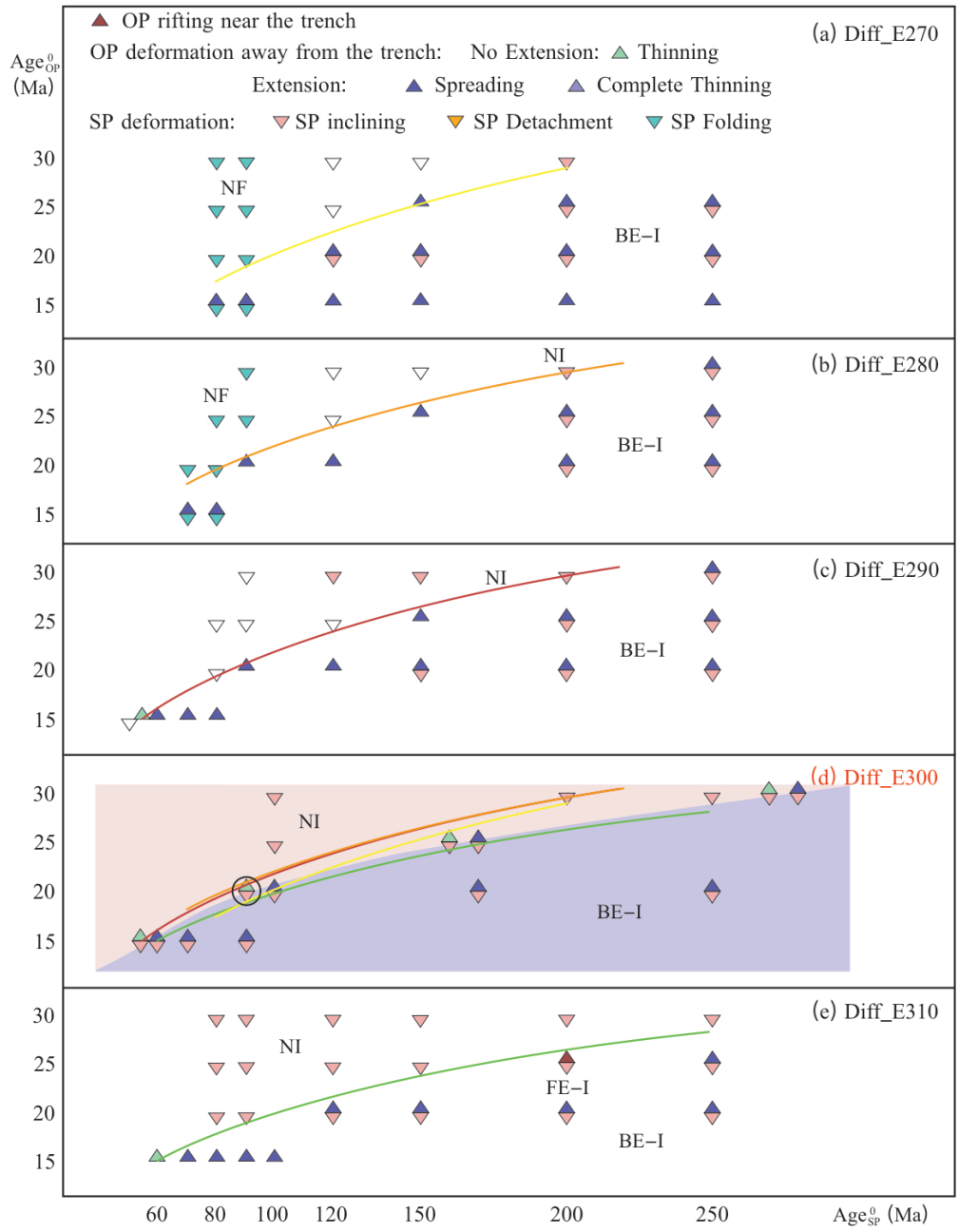

Figure 4.3: Regime diagrams resulting from varying the plate ages with 5 different E_{diff} (in diffusion creep), which are (a) 270, (b) 280, (c) 290, (d) 300, and (e) 310 kJ/mol, respectively. The lines in different colours represent the transition from Extension to No Extension in (a) (b) (c) and (e), and guide the eye in (d), showing how the boundary moves when the E_{diff} varies. The reference model (RM) is marked as a circle in (d).

the bending knee interacts with the LM (Figures 4.4d, e). Notably, the transitional SP behaviour is not delineated as a distinct SP mode because it neither impacts back-arc extension nor qualifies as an end-member mode. Nevertheless, it provides insight into the evolving dynamics between the two primary SP modes.

Three types of OP deformation have been observed in these models: no deformation (Figure 4.4a); back-arc extension (700–800 km away from the trench; Figures 4.4b–e); fore-arc extension (extremely near the trench; Figures 4.4e–g). The back-arc extension shows a trend from OP thinning to break-up to thinning again as the dislocation creep viscosity decreases. To distinguish different degrees of back-arc extension, I classified them into three levels: Thinning (Figures 4.4b, e), Complete Thinning (Figure 4.4c), and Spreading (as shown in Figure 3.3 in Chapter 3 and Figure 4.4d), and marked them with different symbols in Figure 4.5 for a clearer visualisation of the changing trend. As stated in Chapter 3, Complete Thinning and Spreading are defined as 'Extension'. when I distinguish the formation modes, the term 'Extension' is used.

There are 7 combinations of different SP and OP behaviours in this series of models: (a) No deformation on the OP with an inclined SP (NI, Figure 4.4a); (b) back-arc region thinned on the OP with an inclined SP (BT-I, Figure 4.4b); (c) OP Extension at the back-arc region with an inclined SP (BE-I, Figure 4.4c); (d) OP back-arc extension region (SP morphology changes between the two end-members) (BE, Figure 5d); (e) back-arc region thinned on the OP and an OP Extension extremely near the trench (Fore-arc Extension) (BT-FE, Figure 4.4e); (f) extreme OP Extension near the trench (fore-arc extension), but no deformation in the back-arc region (FE, Figure 4.4f); (g) extreme OP Extension near the trench with a detached SP (FE-D, Figure 4.4g). BT-I and BT-FE are transitional modes that help to show the changing trend. The models shown in Figure 4.4 are all highlighted in red in Table 4.3.

In mode FE-D (Figure 4.4g), after the SP detachment, the surface plate that lost its

Table 4.3: Models of changing parameters of dislocation creep.

E_{disl} (kJ / mol)	510	515	520	525	530	535	540	545	550	560
A_{disl} (Pa^{-3} s^{-1})										
2.0×10^{-16}	Disl_1	Disl_47	Disl_6		Disl_11				Disl_16	Disl_21
3.0×10^{-16}	Disl_34	Disl_48	Disl_35		Disl_36					
4.0×10^{-16}	Disl_2		Disl_7	Disl_44	Disl_12	Disl_39			Disl_17	Disl_22
5.0×10^{-16}			Disl_37	Disl_45			RM			
6.0×10^{-16}	Disl_3		Disl_8	Disl_46	Disl_13			Disl_41	Disl_18	Disl_23
7.0×10^{-16}	Disl_31				Disl_32		Disl_33	Disl_42		
8.0×10^{-16}	Disl_4		Disl_9		Disl_14			Disl_43	Disl_19	Disl_24
10.0×10^{-16}	Disl_5		Disl_10		Disl_15	Disl_40			Disl_20	Disl_25

* RM (Reference Model) and the models used in Figure 4.4 are marked in red.

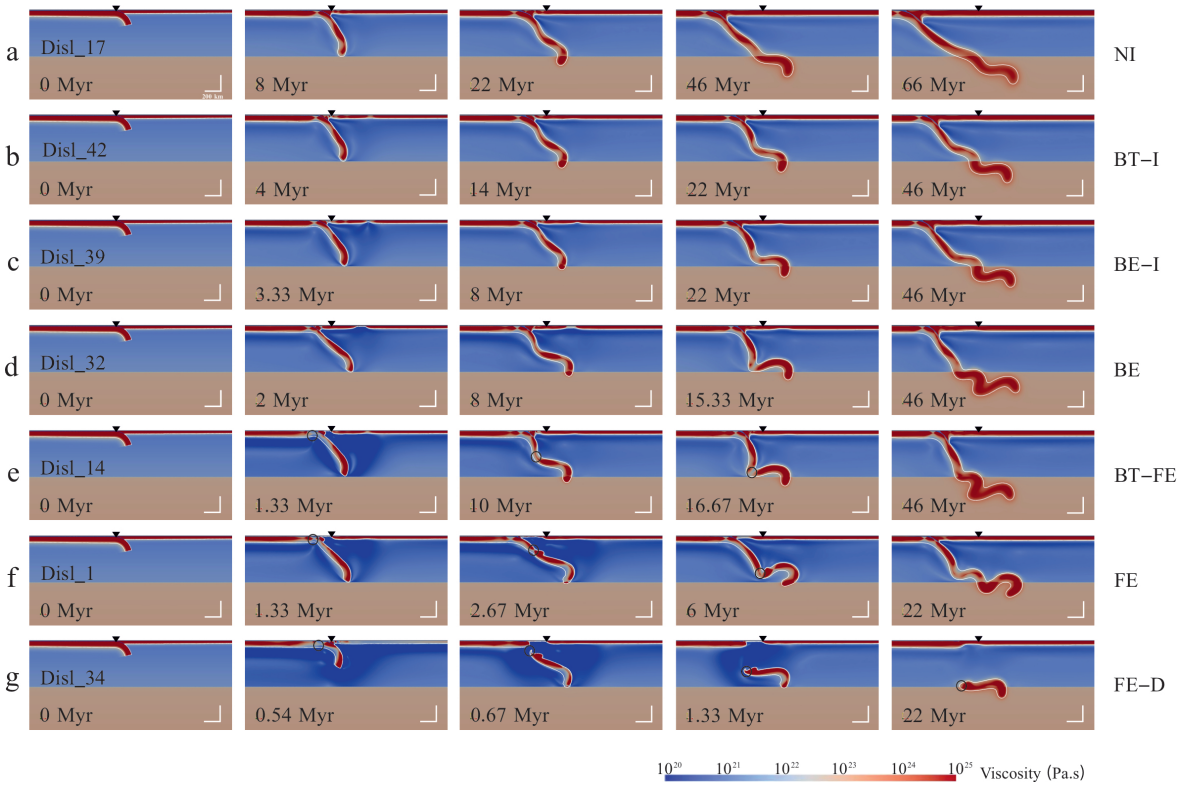

Figure 4.4: Example cases of the deformation modes, resulting from changing dislocation creep parameters, illustrated using the viscosity field. (a) Mode NI (Disl_17), (b) mode BT-I (Disl_42); (c) mode BE-I (Disl_39), (d) mode BE (Disl_32), (e) mode FE-BT (Disl_14), (f) mode FE (Disl_1), (g) mode FE-D (Disl_47). The models shown here are marked by red in Table 4.3 and the rheology parameters of each model can be found in this table. The black triangles mark the initial trench positions. The empty circles in (d)–(g) mark the changes in the locations of the 'bending knee'.

slab pull stops subduction at 0.67 Myr, and only the detached part sinks into the LM. In Figure 4.4f, the SP has been highly weakened and thinned (necking) at a shallow depth near the trench, like that in Figure 4.4g, but it does not break off. The near-broken slab continues the pulling of the following surface plate, the near-broken point behaves similarly to a new slab tip, and it does not experience other forces to be weaker during this process. It implies that the weakening effect on the area corresponding to the break-off location in Figure 4.4g in this set of models is a key to understanding the various SP deformation, which will be described in Section 4.4 Discussion.

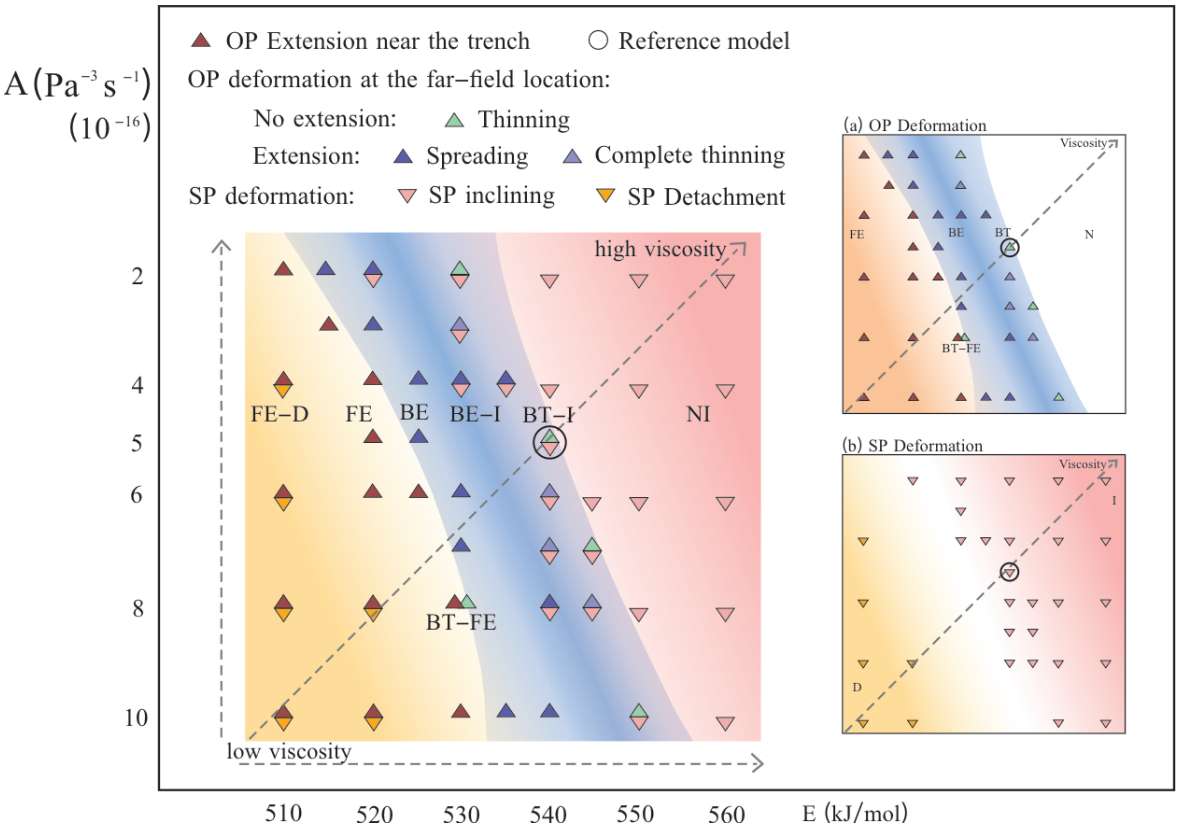

Figure 4.5: The regime diagram of resulting from varying the E_{disl} (activation energy) and A_{disl} (prefactor) parameters of dislocation creep viscosity. To provide clearer information, diagrams of (a) OP Deformation and (b) SP Deformation are shown separately. The meanings of the symbols are the same as in Figure 4.2. It is worth noting that only 3 colours are used to express 6 different modes (mode FE-BE is shown in only one model, so it does not have a domain). Models in the yellow domain have Extension near the trench (Fore-arc Extension), but the depth of yellow represents the deformation degree of the SP, and darker yellow means the occurrence of SP detachment. The blue shades represent the deformation degree of the back-arc region on the OP and the pink shades represent the deformation degree of the SP, which are the same as in Figure 4.2. The dashed arrows indicate the viscosity increasing direction. Note that I set A_{disl} decreases as it goes up the y-axis to show an upwards-increasing viscosity.

4.3.2.2 Varying plate ages with various E_{disl}

When A_{disl} is fixed to the reference value (5×10^{-16} $Pa^{-3}s^{-1}$), models show different modes (FE-D, FE, BE, BT-I and NI) as E_{disl} is varied (510, 520, 530, 540 and 550 kJ/mol), respectively (Figure 4.5). Based on these E_{disl} values, the initial plate ages were tested systematically in 5 groups (Table A.2). 540 kJ/mol is the reference value

of E_{disl}, and Figure 4.6d is the same as Figure 3.6 (the reference diagram).

When E_{disl} increases from the reference value (540 kJ/mol), the only change is the threshold between modes NI and BE (and BT-I) in plate ages (see green line in Figures 4.6d and e). It requires a younger OP (weaker to be broken) or older SP (stronger to induce a larger mantle flow) to encourage the back-arc extension (Figure 4.6e). As E_{disl} decreases gradually, the N–E threshold rises in Age^0_{OP} (Figure 4.6). Additionally, a slightly lower E_{disl} (530 kJ/mol) starts to encourage fore-arc extension near the N–E threshold, whereas the back-arc extension still dominates when Age^0_{SP} is old (e.g. 250 Ma) or Age^0_{OP} is young enough (e.g. 15 Ma, Figure 4.6c). However, a much lower E_{disl} does not encourage back-arc extension anymore, instead, the OP extension always occurs near the trench (Figures 4.6a, b). As for the SP behaviour, a lower dislocation creep viscosity encourages slab detachment when Age^0_{SP} is relatively young (mostly younger than 100 Ma). There is also a model with an old Age^0_{SP} that generates slab detachment (E510_SP200_OP30), the reason why the SP breaks off but that in E510_SP150_OP30 does not is still to be completely explored. There are some other examples which show non-intuitive results. Age^0_{SP} in model E530_SP90_OP15 (90 Ma) is older than that in E530_SP80_OP15 (80 Ma), and the older SP should be stronger than a younger one. While I would expect a younger SP to more easily break off in a subduction zone, these two models show a contrary result.

Compared to the range of dislocation creep viscosity parameters investigated here, plate ages are less important because rheology is the first-order parameter that influences plate behaviours.

Table 4.4: Models of changing parameters of Peierls creep.

E_P (kJ/mol) / A_P (Pa^{-20} s^{-1})	400	430	460	490	520	540	550	580	610
1.0×10^{-152}	P_1	P_6	P_11	P_16	P_21		P_26	P_31	P_36
1.0×10^{-151}	P_2	P_7	P_12	P_17	P_22		P_27	P_32	P_37
1.0×10^{-150}	P_41		P_43	P_44	P_45	RM			
1.0×10^{-149}	P_3	P_8	P_13	P_18	P_23	P_46	P_28	P_33	P_38
1.0×10^{-148}	P_4	P_9	P_14	P_19	P_24	P_47	P_29	P_34	P_39
1.0×10^{-147}	P_5	P_10	P_15	P_20	Diff_25	P_48	P_30	P_35	P_40

* RM (Reference Model) and the models used in Figure 4.7 are marked in red.

4.3.3 Peierls creep

4.3.3.1 Varying parameters of Peierls creep

The activation energy of Peierls creep (E_P) is varied from 400 to 580 kJ/mol, and the prefactor (A_P) from 1×10^{-147} to 1×10^{-152} $Pa^{-20}s^{-1}$ (Table 4.4).

In this set of models, some of the SP morphologies are close to that in Section 4.3.2. There is no doubt that a stronger SP exhibits an inclined orientation and promotes trench retreat no matter which Peierls viscosity parameter is increased, meanwhile, the OP shows less deformation. When the Peierls creep viscosity decreases, the SP shows a similar trend of deformation and a mostly similar end behaviour at low viscosity (SP detachment) as that in Section 4.3.2 (Figure 4.4). A new mode of SP is shown in model P_38 (Figure 4.7e), in which the remaining slab continues to subduct after an earlier episode of SP detachment. Other SP detachment models like Disl_47 (Figure 4.4g) and

P_2 (Figure 4.7f) do not keep a bending part of SP after the detachment, which results in the healing of the asthenosphere window produced by the break-off. As for the OP deformation, back-arc extension occurs in all models that have a lower Peierls creep viscosity, and it occurs before SP detachment in model P_38, P_2, and P_4 (Figures 4.7e, f, g), then the Extension tends to heal after the detachment. In addition, there is a special mode in which the part of the OP between the trench and the back-arc extension subducts into the mantle and breaks-off from the back-arc extension location when the Peierls creep viscosity is sufficiently decreased (Figure 4.7g).

There are 7 combinations of different SP and OP behaviours in this series of models: (a)–(d) are quite similar to those in Section 4.3.2 (Figures 4.7a–d); (e) OP Extension at the back-arc region with a detached SP, then the remainder of the SP continues subduction (BE-DS, Figure 4.7e); (f) OP with back-arc Extension with a detached SP, the retained slab does not subduct (BE-D, Figure 4.7f); (g) OP suffers back-arc Extension, then the SP detaches, which leads the near-trench part of the OP to subduct and break-off from the back-arc extension location (BE-OPSPD, Figure 4.7g). As the Peierls creep viscosity increases, the modes change from BE-OPSPD, to BE-D, to BE, to BE-I, to BT-I, to NI (Figure 4.8). Different from Dislocation models, no fore-arc extension occurs no matter how the Peierls creep viscosity is changed. The models shown in Figure 4.7 are all highlighted in red in Table 4.4.

The range of E_P value is broader than that of E_{diff} and E_{disl}, which is 180 kJ/mol (from 400 to 580 kJ/mol), whereas the other two E value ranges are only 70 (from 250 to 320 kJ/mol) and 50 kJ/mol (from 510 to 560 kJ/mol), respectively. More specifically, when A_P is fixed to the reference value (1×10^{-150} $Pa^{-20}s^{-1}$), one of the end-member modes BE-OPSPD requires an E_P less than 400 kJ/mol, whereas another end-member mode NI needs E_P of 580 kJ/mol. However, only 40 kJ/mol needs to be increased to get an end-member mode NI from another end-member FE-D (510 kJ/mol to get

FE-D and 550 kJ/mol to get NI) when A_{disl} is the reference value (5×10^{-16} $Pa^{-3}s^{-1}$). Similar to the range of E_{diff}, one end-member mode NF needs 260 kJ/mol and the other (mode NI) needs 310 kJ/mol with the reference A_{diff} (3×10^{-11} $Pa^{-1}s^{-1}$). Thus it can be seen that E_P is not as sensitive as E_{disl} and E_{diff} in these models in respect of changing the plate behaviour modes.

back-arc extension is ubiquitous in models with decreased Peierls viscosity, revealing a clear distinction from Dislocation models where fore-arc extension was prominent. This uniqueness in plate behaviour due to Peierls creep may be a critical consideration for geodynamic models.

4.3.3.2 Varying plate ages with various E_P

As stated in Section 4.3.3, E_P is less sensitive to change in plate bahaviour than E_{diff} and E_{disl}. Thus, E_P chosen in this section are over wider intervals, which are 400, 450, 500, 540, and 560 kJ/mol, respectively (Table A.3, Figure 4.9).

Same as the results of changing Dislocation Creep, when E_P is increased from the reference value (540 kJ/mol), the only change is the threshold between modes NI and BE (and BT-I) in plate ages. A younger OP or older SP encourages back-arc extension. The changing trend of the N–E threshold is also the same as that in Dislocation models, which is that the N–E threshold increases as E_P is reduced. Peierls creep is not significant in controlling the spatial location of OP extension. Even with various plate ages, no the models show fore-arc extension on the OP. When E_P decreases to 500 kJ/mol, the SP breaks off as Age^0_{OP} and Age^0_{SP} are both young (Age^0_{OP} is younger than 20 Ma and Age^0_{SP} is younger than 90 Ma). Further reduction in E_P causes the SP to break off more easily, it also increases the threshold of slab detachment in both Age^0_{OP} and Age^0_{SP} (e.g. E450_SP120_OP20 is able to generate an SP detachment even though the Age^0_{SP} is 120 Ma). Even more extreme, a very low E_P

(400 kJ/mol) causes the SP to break off in all models which only change Age^0_{OP} and Age^0_{SP}. It suggests that such a low E_P value is very unlikely because SP detachment is actually very rare. In addition, the low E_P also causes the OP between the back-arc extension location and the trench to subduct and then break off following the earlier detachment of the SP when Age^0_{OP} and Age^0_{SP} are both relatively young (Figures 4.9a, b). In the low-E_P models, SP Detachment (D) can happen independently without back-arc extension if Age^0_{SP} is young enough to break off but Age^0_{OP} is not young enough to be broken (Figures 4.9a, b, c).

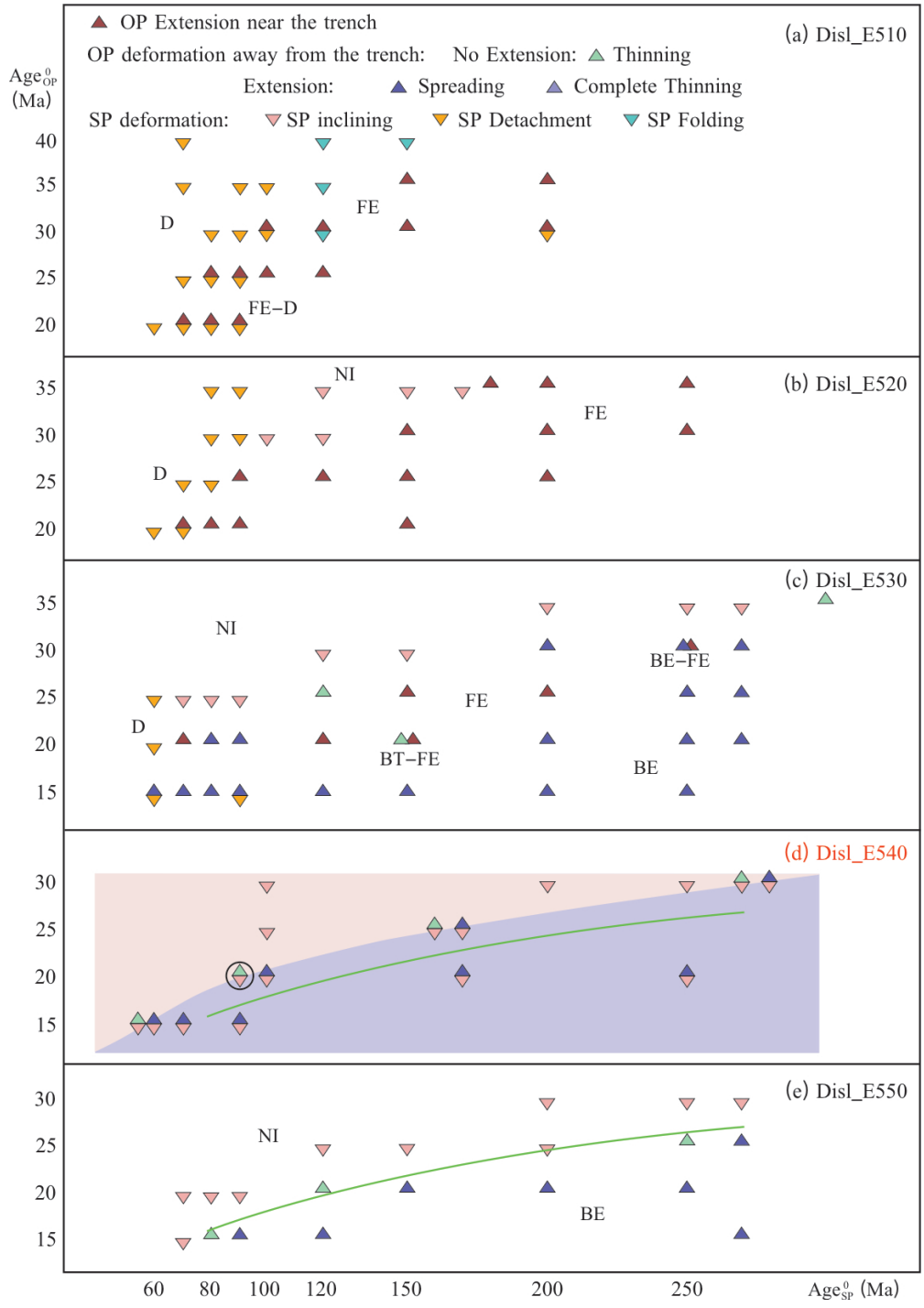

Figure 4.6: Regime diagrams resulting from varying the plate ages with 5 different E_{disl}, which are (a) 510, (b) 520, (c) 530, (d) 540, and (e) 550 kJ/mol, respectively. The green line in (d) and (e) is a line to guide the eye in (d), which represents the transition from BE in (e), showing that the boundary moves to higher Age^0_{OP}. The reference model (RM) is marked as a circle in (d).

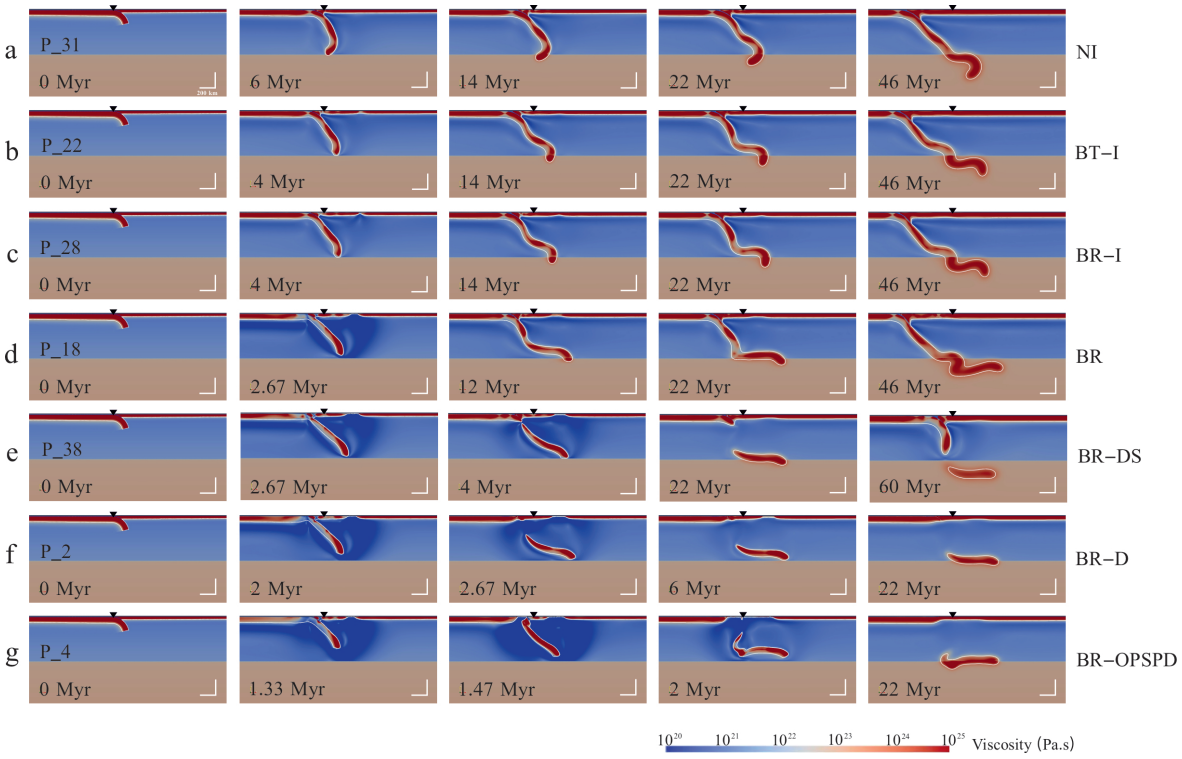

Figure 4.7: Example cases of the deformation modes illustrated using viscosity field for changing Peierls creep parameters. (a) Mode NI (P_31), (b) Mode BT-I (P_22), (c) Mode BE-I (P_28), (d) Mode BE (P_18), (e) Mode BE-DS (P_38), (f) Mode BE-D (P_2), (g) Mode BE-OPSPD (P_4). The models shown here are marked in red in Table 4.4 and the rheology parameters of each model can be found in this table. The black triangles mark the initial trench positions.

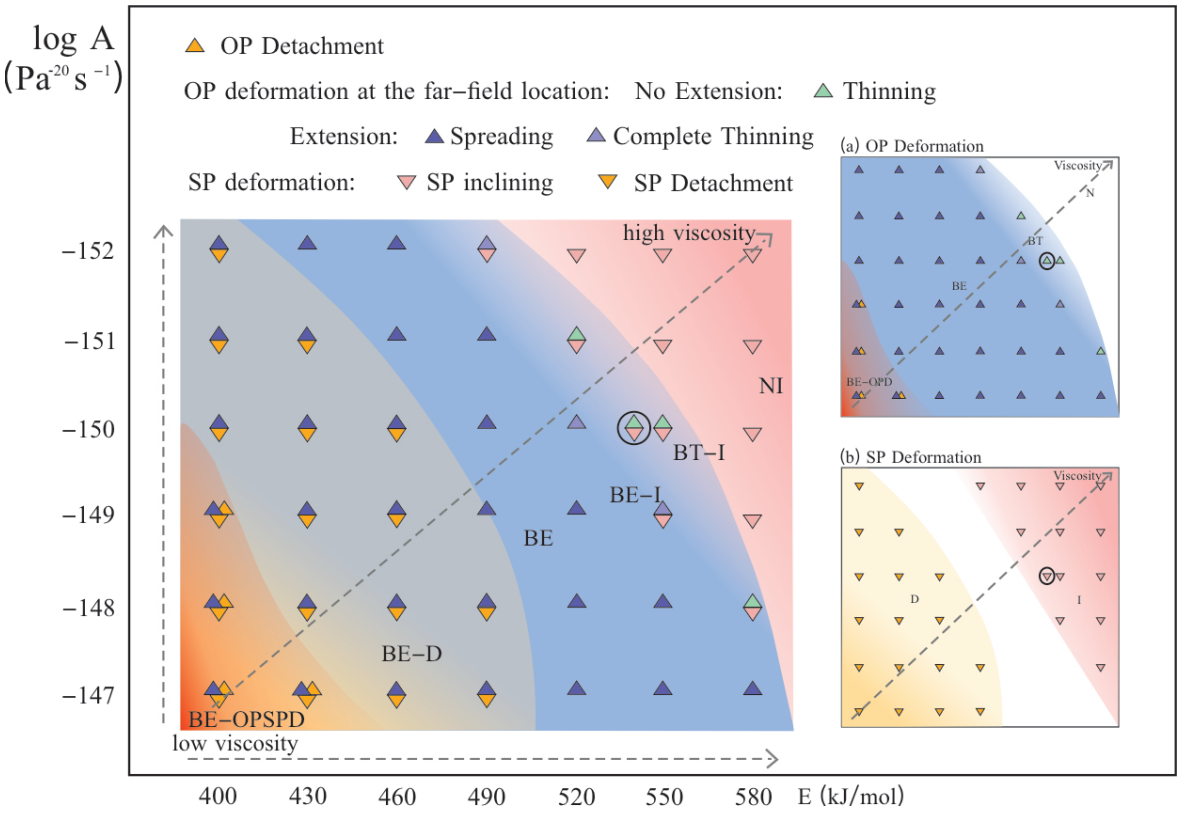

Figure 4.8: The regime diagram of E_P (activation energy) and A_P (prefactor) of Peierls creep viscosity. To provide clearer information, diagrams of (a) OP deformation and (b) SP deformation are shown separately. The meanings of symbols are the same as in Figure 4.2. The triangles in orange represent plate detachment. The upper ones mean OP detachment and the lower ones mean SP detachment. The blue domain (increasing the transition zones with pink and yellow) represents all the models which have a back-arc deformation on the OP, the light orange shade shows the SP detachment, and the orange overlap means the OP break-off. The dashed arrows indicate the viscosity increasing direction. Note that I set A_P decreases as it goes up the y-axis to show an upwards-increasing viscosity.

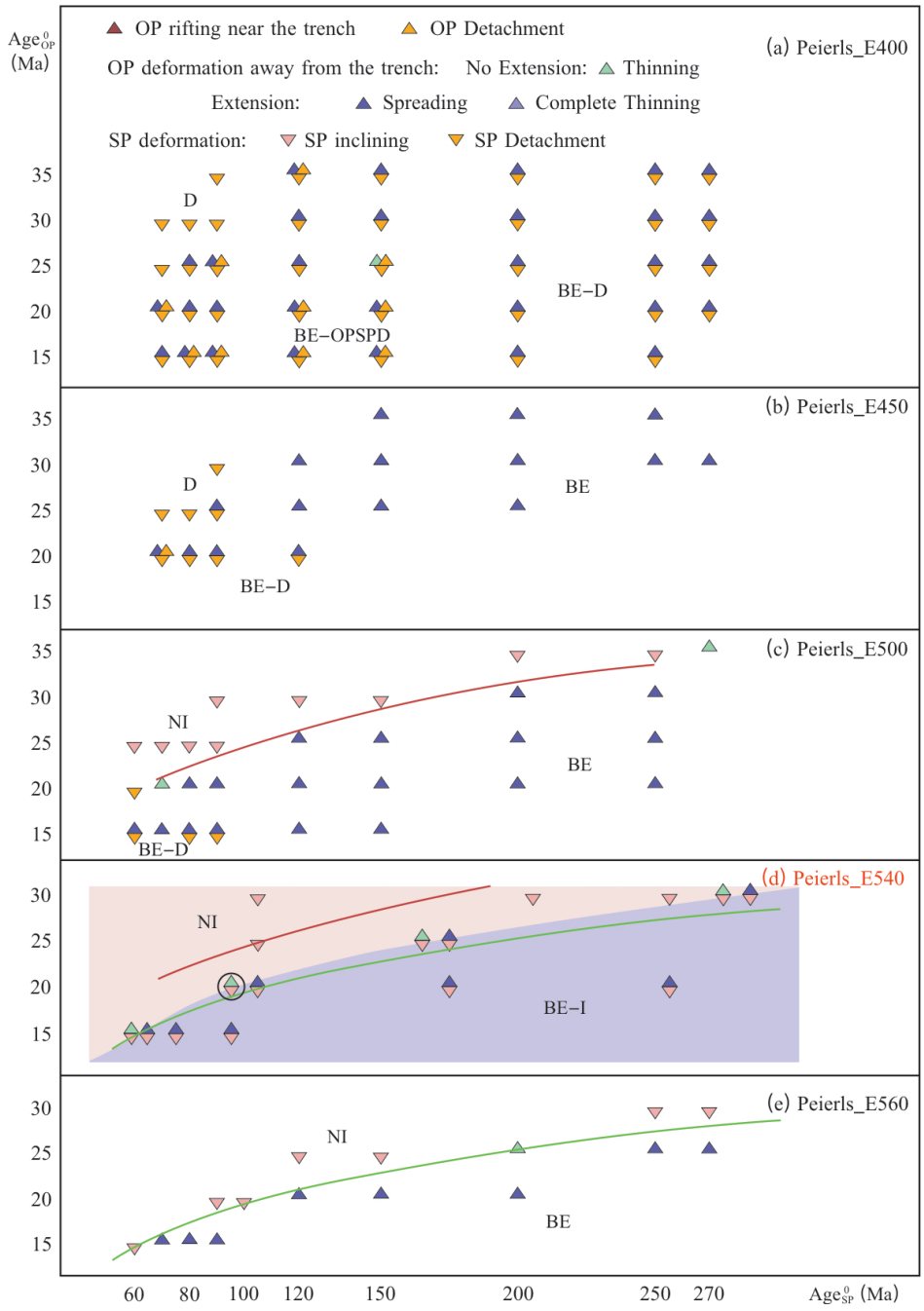

Figure 4.9: Regime diagrams resulting from varying the plate ages with 5 different E_P, which are (a) 400, (b) 450, (c) 500, (d) 540, and (e) 560 kJ/mol, respectively. (d) is based on the reference rheology and as a comparison. The red and green lines in (c) (d) and (e) are lines to guide the eye in (d). They represent the transition from BE in (c) and in (e), respectively, showing how the boundary moves when the E_P varies. The reference model (RM) is marked as a circle in (d).

Table 4.5: Models of changing parameters of Yield Strength.

fc yld_{max} (MPa)	0.1	0.12	0.14	0.16	0.18	0.2	0.22	0.24
1.0×10^{11}	Y_1	Y_4	Y_7	Y_10	Y_13		Y_16	Y_19
1.0×10^{10}	Y_22	Y_23	Y_24	Y_25	Y_26	RM		
1.0×10^{9}	Y_2	Y_5	Y_8	Y_11	Y_14	Y_27	Y_17	Y_20
1.0×10^{8}	Y_3	Y_6	Y_9	Y_12	Y_15	Y_28	Y_18	Y_21

* RM (Reference Model) and the models used in Figure 4.7 are marked in red.

4.3.4 Yield Strength

4.3.4.1 Varying parameters of Yield Strength

Parameters of the yield strength act on the whole domain except the weak layer, in which the friction coefficient (fc) is much smaller. I vary the maximum yield strength (yld_{max}) from 1×10^{8} to 1×10^{11} MPa, and the friction coefficient (fc) from 0.1 to 0.26 (Table 4.5). This combination of parameters is different from the three discussed above (diffusion, dislocation and Peierls). Both E and A are factors used to calculate the viscosity, so when they are changed systematically, the viscosity changes gradually, as well as the modes. While fc controls the yield strength, the yld_{max} represents a limit of the value, which results in a different way of changing modes.

In this series of models, four modes which are mostly the same as mode NI, BE, BE-D, and BE-OPSPD in models of changing Peierls creep parameters have been recognised (Figures 4.10a–d). Additionally, there are two unique modes when I decrease the maximum yield strength but do not reduce the friction coefficient low enough (Figures 4.10e, f). They both have a rapid detachment of the SP tip when it is far

from reaching the LM, whereas the SP detachment occurs when the tip subducts to a deeper depth in other modes. The broken-off fragment of the slab sinks rapidly until it reaches the LM. Then, the remaining SP continues to subduct downward, which can be regarded as a new subduction process. When the new SP tip is close to the fragment, back-arc extension occurs on the OP in model Y_12 at about 8 Myr after the simulation initiation, while there is no OP extension in model Y_15 under the same situation (ca. 12 Myr, Figure 4.10e). The back-arc extension in model Y_12 only lasts for a short period and heals in less than 1 Myr. At 10.67 Myr, the new SP changes its subduction direction suddenly and surprisingly, then it breaks off soon after and piles up zigzag in the transition zone of the UM and the LM (Figure 4.10f).

There are 6 combinations of different SP and OP behaviours in this series of models: (a)–(d) are the same as those in Section 4.3.3 (Figures 4.10a–d); (e) There is no deformation on the OP, and a detachment of the SP tip, then the remainder of the SP continues subduction (N-DS, Figure 4.10e); (f) Detachment of the SP tip—remaining SP subducts constantly—OP extension at the back-arc region—SP detachment (D-BE-D, Figure 4.10f). The models shown in Figure 4.10 are all highlighted in red in Table 4.5.

From figure 4.11 it is obvious that the friction coefficient (fc) plays a more important role in the plate behaviours compared to the maximum yield strength (yld_{max}). When yld_{max} is over 10^9 Pa, only fc influences the modes of plate behaviours, whereas yld_{max} of 10^8 Pa generates modes N-DS and D-BE-D which are not currently found on Earth.

4.3.4.2 Varying plate ages with various friction coefficients of Yield Strength

As stated above, fc is a significant parameter in the yielding mechanism, and a yld_{max} of 10^8 Pa is relatively low compared to experiments of mantle minerals at high pressure (Mei et al., 2010). Based on the reference yld_{max}, models show different

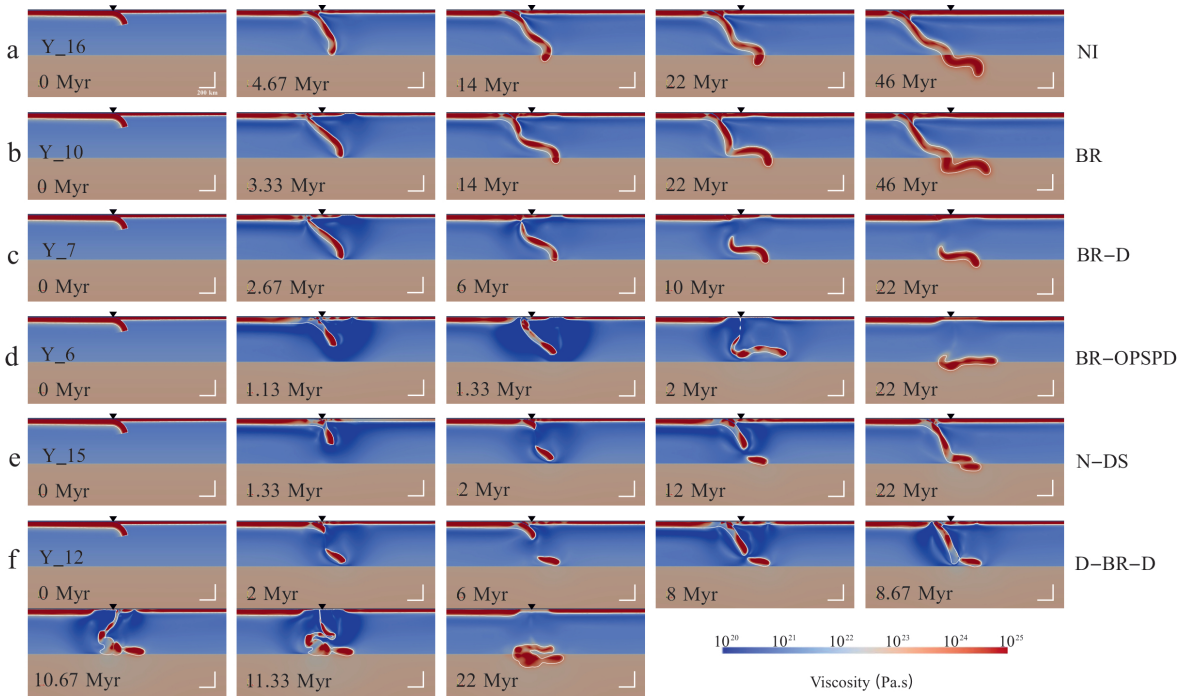

Figure 4.10: Example cases of the deformation modes resulting from changing parameters of the yield strength, illustrated using the viscosity field. (a) Mode NI (Y_16), (b) mode BE (Y_10), (c) mode BE-OPSPD (Y_6), (d) mode BE-D (Y_7), (e) mode N-DS (Y_15), (f) mode D-BE-D (Y_12). The models shown here are marked by red in Table 4.3.4 and the rheology parameters of each model can be found in this table. The black triangles mark the initial trench positions.

modes (BE-OPSPD, BE-D, BE, BT-I and NI) as the fc are 0.1, 0.14, 0.18, 0.2 and 0.22, respectively (Figure 4.11). Thus, the models run to test the influence of plate ages were run for these fc values. For comparison, the reference value of fc is 0.2.

When fc is increased from 0.2 to 0.22, the regime diagram of plate ages barely changes. The threshold of the plate ages to Mode BE, when fc is 0.22, is almost the same as that when fc is 0.2 (Figure 4.12e). However, a surprising phenomenon is that extension on the OP does not happen at the back-arc location anymore but in the fore-arc when fc is further increased to 0.26 (Figures 4.12f, 4.13b). It is noticed that fore-arc extension does not occur in models with smaller fc values. When fc is reduced to 0.18, the line showing the threshold of the plate ages to Mode BE rises obviously

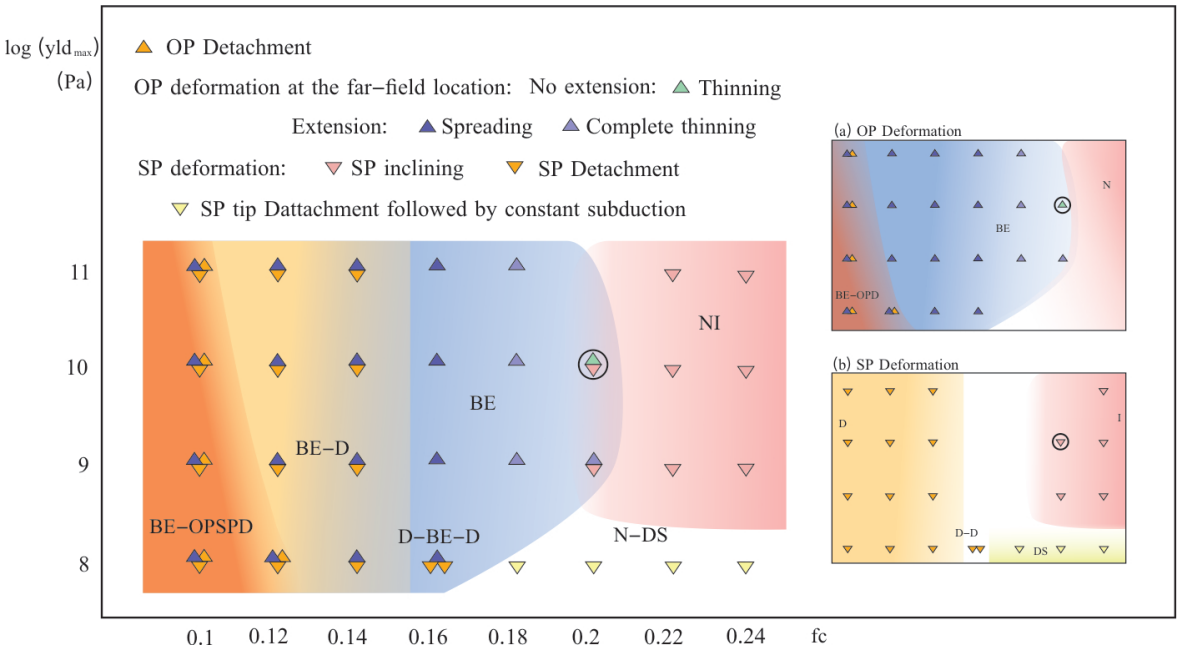

Figure 4.11: The regime diagram of the maximum yield strength (yld_{max}) and friction coefficient (fc) of the normal (i.e. non-weak zone) material. To provide clearer information, diagrams of (a) OP deformation and (b) SP deformation are shown separately. The meanings of symbols are the same as that in Figure 4.2.

compared to models with reference fc (Figures 4.12c, d), and young ages (50 to 60 Ma) encourage the slab to break off. Continuously lowering fc (0.14) further encourages slab detachment when the SP is relatively young (Figure 4.12b). When the fc is very low (0.1, half of the reference value), most models show BE-OPSPD. The generation of a large number of unrealistic modes when fc equals 0.1 in models suggests that 0.1 is too low a value for the friction coefficient in the mantle away from the slab interface.

Additionally, a new mode of plate behaviour is generated when fc is low enough (0.1 and 0.14), and it occurs when the Age^0_{SP} is young (80 or 90 Myrs) and Age^0_{OP} is relatively old (25 or 30 Myrs). The mode shows that the SP rifts and the slab tip pulls the OP to subduct the same as that in Mode BE-OPSPD, but the back-arc extension does not exist (Figure 4.13a). This mode is named OPSPD.

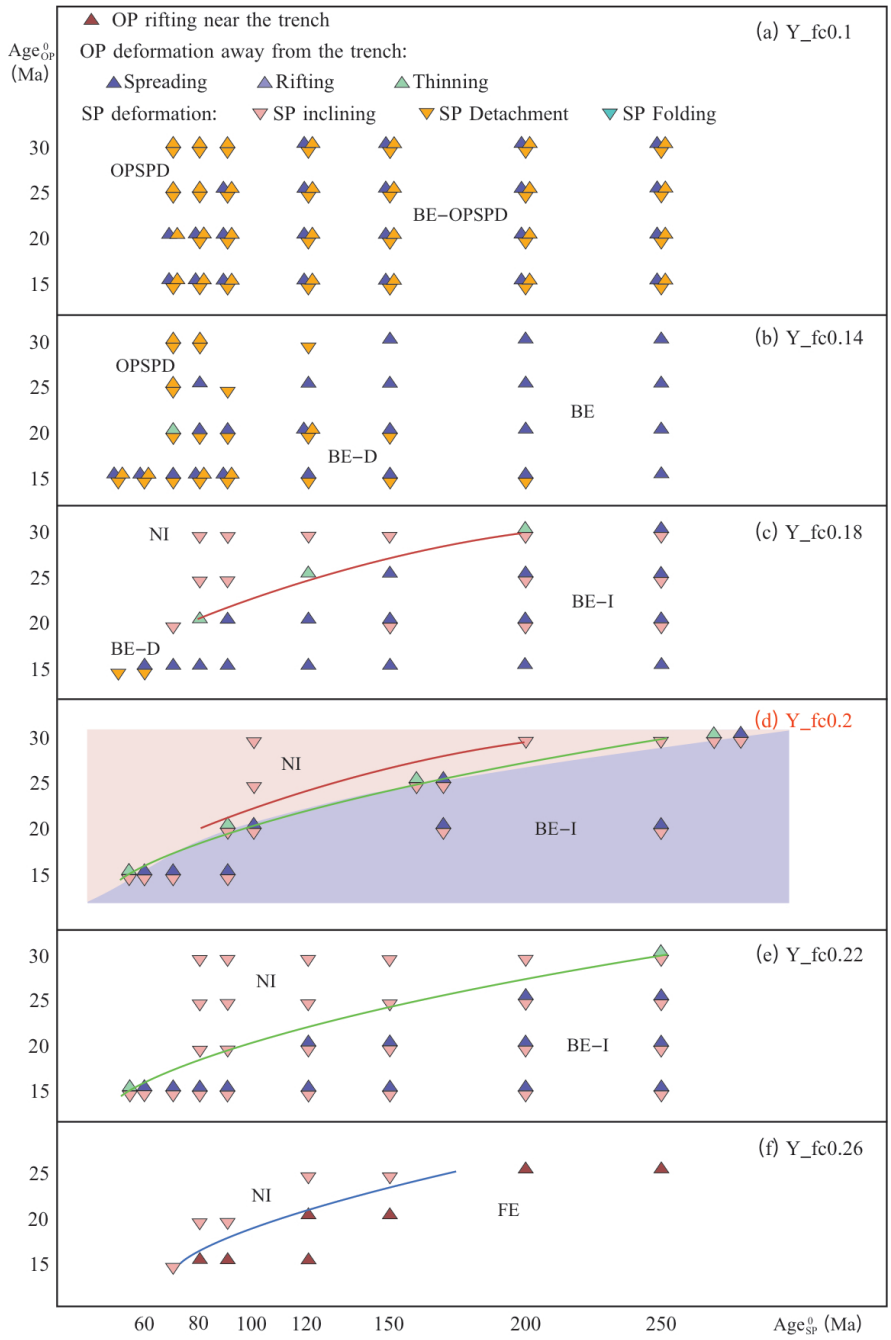

Figure 4.12: Regime diagrams resulting from varying the plate ages with 6 different friction coefficients (fc), which are (a) 0.1, (b) 0.14, (c) 0.18, (d) 0.2, (e) 0.22 and (f) 0.26 kJ/mol, respectively. (d) is based on the reference rheology and as a comparison. The red and green lines in (c) (d) and (e) are lines to guide the eye in (d). They represent the transition from BE in (c) and in (e), respectively, showing how the boundary moves when the E_P varies. The reference model (RM) is marked as a circle in (d).

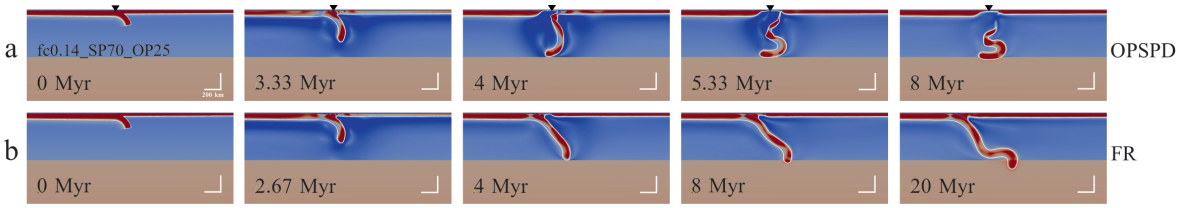

Figure 4.13: Example cases of the deformation modes resulting from changing parameters of the yield strength, illustrated using the viscosity field. (a) Mode OPSPD (fc0.14_SP70_OP25), (b) mode FE (fc0.26_SP120_OP20). The black triangles mark the initial trench positions.

4.3.5 The role of each deformation mechanism in composite rheology

Despite the obvious influence of plate ages, it's evident that rheology is the key to determining plate behaviours.

The dominant deformation mechanism is defined as the one that has the lowest viscosity value. Figure 3.2 shows that the dominant deformation mechanism is spatially layered within the OP in the non-steady state (before the SP tip reaches the LM) in RM. The yielding mechanism dominates the shallowest layer of OP near the surface, which is down to about 23-km depth when the Age^0_{OP} is 20 Myrs (the thickness of each deformation mechanism can be varied slightly according to the different Age^0_{OP}s). Next in depth, the underlying Peierls layer is always less than 10-km thick except when changing the Peierls parameters. The bottom of the OP is dominated by dislocation creep and this deformation mechanism also dominates a large domain around the OP and the SP in the UM. The rest of the UM and the whole of the LM are dominated by diffusion creep, whereas the majority of the SP is governed by Peierls creep except for a core with the maximum viscosity. The RM does not show the minimum viscosity (1.0×10^{18} Pa s) during its evolution, while changing some parameters could produce the minimum viscosity near the plates, particularly around the trench (e.g. Figures

4.16a, g). These models showing such low viscosity may not fit the reality, but they still help us to understand how the viscosity changes affect plate behaviours in the UM (e.g. Section 4.4.1).

The model results demonstrate a nuanced difference between the effects of decreasing diffusion versus dislocation creep parameters. While the former results in slab folding, the latter significantly weakens the bending knee leading to possible slab detachment. This distinction emphasises the importance of understanding and accurately modelling both deformation mechanisms when investigating subduction processes.

The viscosity field shows that the reduction in viscosity on the OP begins at the surface (due to yielding) and the plate's base (because of dislocation creep). Subsequently, the necking of the viscosity is observed at the plate's mid-depth, where Peierls creep is the primary factor. This implies that Peierls creep plays a less important role in triggering OP softening compared to yielding and dislocation creep. This phenomenon is also consistent with the results that plate behaviours are less sensitive to Peierls creep than other deformation mechanisms (see Section 4.3.3).

One of the commonly distinctive outcomes of decreasing dislocation and Peierls creep viscosity is the pronounced weakening at the bending knee (near the trench horizontally, Figures 4.4, 4.7). This weakening dictates the subsequent behaviour of the SP. This is particularly crucial as it underscores the sensitivity of the subduction zone to changes in dislocation creep parameters. A significant weakening could lead to the detachment of the leading part of the SP, an end-member behaviour seen in these models.

4.4 Discussion

4.4.1 How the overriding and subducting plates deform

4.4.1.1 OP deformation: extension at different locations

There exist three distinct morphologies for the OP in this study: Extension at the far-field location (Back-arc Extension, abbreviated as BE), Extension very near the trench (Fore-arc Extension, abbreviated as FE), No Extension on the entire OP (NE). For easier reading, a conclusion table of all the plate behaviours has been made (Figure 4.14).

<table>
<tr><th></th><th>Diffusion creep</th><th>Dislocation creep</th><th>Peierls creep</th><th>Yield strength</th></tr>
<tr><td rowspan="7">High viscosity
↑
Low viscosity</td><td colspan="4">NI (No extension on the OP with Inclined SP)</td></tr>
<tr><td colspan="4">BT-I (Back-arc Thinning on the OP with Inclined SP)</td></tr>
<tr><td colspan="4">BE-I (Back-arc Extension on the OP with Inclined SP)</td></tr>
<tr><td colspan="4">BE (Back-arc Extension with transitional SP)</td></tr>
<tr><td>BT-F (Back-arc Thinning with Folded SP)</td><td>FE (Fore-arc Extension)</td><td colspan="2">BE-D (Back-arc Extension with Detached SP)</td></tr>
<tr><td>NF (No extension on the OP with Folded SP)</td><td>FE-D (Fore-arc Extension with Detached SP)</td><td colspan="2">BE-OPSPD (Back-arc Extension with Detached OP and SP)</td></tr>
<tr><td>Speciality</td><td></td><td></td><td></td><td>D-BE-D</td></tr>
</table>

*D-BE-D SP Detaches, then Back-arc Extension happens, after that the SP Detaches again.

Figure 4.14: Conclusion table of plate behaviours in the 4 classes of models.

As discussed in Chapter 3, the Extension process at the far-field location is a competition between basal drag that thins the OP versus thermal healing that thickens it. The process in that case is straightforward because the thermal structure was changed directly by the initial ages of the plates in that section. Here the difference is that

what is varied are the parameters of each deformation mechanism, including activation energy (E) and prefactor (A) in diffusion, dislocation, and Peierls creeps, as well as friction coefficient (fc) and maximum yield strength (yld_{max}) in yielding strength. When the parameters are varied, the composite rheology changes correspondingly, and the feedback to the temperature influences the thermal structure as a result. When the basal drag wins out, thermal weakening happens on the OP and the viscosity is significantly reduced, but because of the different dominant deformation mechanisms, not all thermal weakening causes viscous extension. In NE models, the basal drag is too weak to drive extension or the OP is so strong, when thermal healing wins out. For FE and BE modes, the Extension process is a competition between the thermal weakening near the trench and at the far-field location. As a matter of fact, the RM has already shown that the location near the trench is a potential place of thermal weakening because the mantle flow wedge thins the OP in the corner (Figure 3.2). However, the mantle flow cell always causes stronger basal drag at the far-field location than the near-trench location if there is no existing thermal weakened area somewhere else (a hot region is introduced on the OP in Chapter 5, and these models provide insights into the change of the mantle flow cell). The FE mode is shown in models whose dislocation viscosity is reduced by E_{disl} and/or A_{disl} (Figure 4.5). Take the case Disl_10 for example (Figure 4.15), the viscosity at the mantle wedge corner which is dominated by the dislocation creep decreases quickly and soon becomes the minimum viscosity in less than 1 Myr because of the relatively high temperature and low E_{disl} and/or A_{disl}. The weakness in rheology feeds back to the thermal structure and results in the thermal weakening. This, in turn, attracts some flow into the weak area due to mass continuity, restricting the growth of the mantle flow at the far-field location before it can expand substantially. In contrast, if the dislocation component of the viscosity does not decrease that fast at the mantle wedge corner when E_{disl} and/or A_{disl} are higher, then the mantle

flow cell grows large enough to encourage the extension at the far-field location, and the models will show the BE mode.

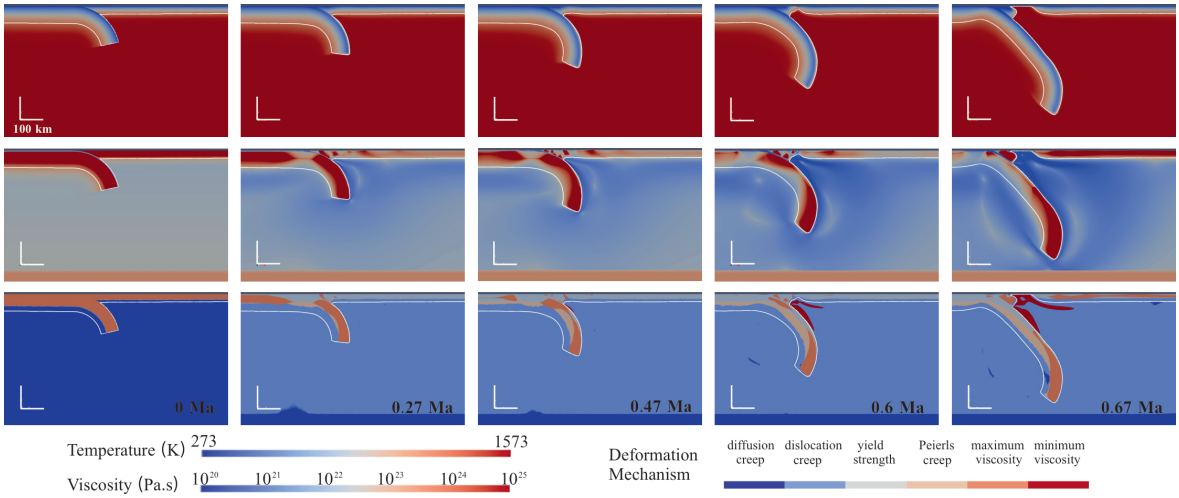

Figure 4.15: Simultaneous snapshots of a zoom-in of the case 'Disl_10' showing the time evolution of temperature field, viscosity field, and dominant deformation mechanism. All snapshots show the isothermal contour of 1300 K in white.

4.4.1.2 SP morphologies and their probable influence on OP deformation

The results of varying parameters in the four deformation mechanisms show a few different SP morphologies, generally including SP inclining, SP folding, and SP detachment, where the SP detachment always occurs after the back-arc extension if there is one, so it does not influence back-arc extension in these simulations. These three SP morphologies represent three end-member deformations. There are transitional behaviours between SP inclining and detachment, as well as SP inclining and folding, respectively, which helps to understand the evolution. In common, the SP tip in all models penetrates through the transition zone and into the LM no matter which SP deformation style it is in.

The stiffness of the SP is significant to sinking, bending and other deformation

(Ribe, 2010). SP inclining is produced from a rigid slab, which is hard to deform or bend. When the viscosity of any deformation mechanism is high, which means the composite viscosity in the whole domain is high, the SP becomes inclined (Figures 4.1, 4.4, 4.7, 4.10).

SP detachment happens when the dislocation, the Peierls viscosity or yielding strength is low enough. The models in this study show that the mantle flow triggered by the SP is not only active under the OP but also on the SP side. When the mantle flow is going up to the OP and growing stronger, the upwelling to the SP is growing as well and weakening the SP near the trench (this location of weakness in the SP which migrates with subduction is called 'bending knee' in this thesis) at that time. In models which have relatively weak rheology due to reduced viscosity mechanism parameters, the rheology of the bending knee is significantly weakened and break-off can occur. There is also a transitional SP morphology between SP inclining and detachment shown in all the above three families of models (Figures 4.4e, 4.7d, and 4.10b), helping to understand the SP break-off process. In the transitional SP mode, the bending knee is not weak enough to break off, instead, it continues to sink into the UM, but the SP bends over at the bending knee because of its weakness. Before the signature deformation starts, the dominant deformation mechanism is layered in the horizontal part of the SP the same as the RM (see Section 4.3.5). They are yielding, Peierls and dislocation creeps from the top to the bottom of the SP, and the surrounding mantle around the bending knee is governed by dislocation creep. With the decrease of dislocation viscosity, the composite rheology lowers and the strain rate increases at the bending knee. When the yielding viscosity decreases, almost the entire SP, especially the bending knee near the trench, is dominated by yielding, so it becomes very weak (Figure 4.16). However, brittle failure (which the yielding mechanism is possibly modelling) only works at shallow depths on Earth, so this model might not

be a realistic case.

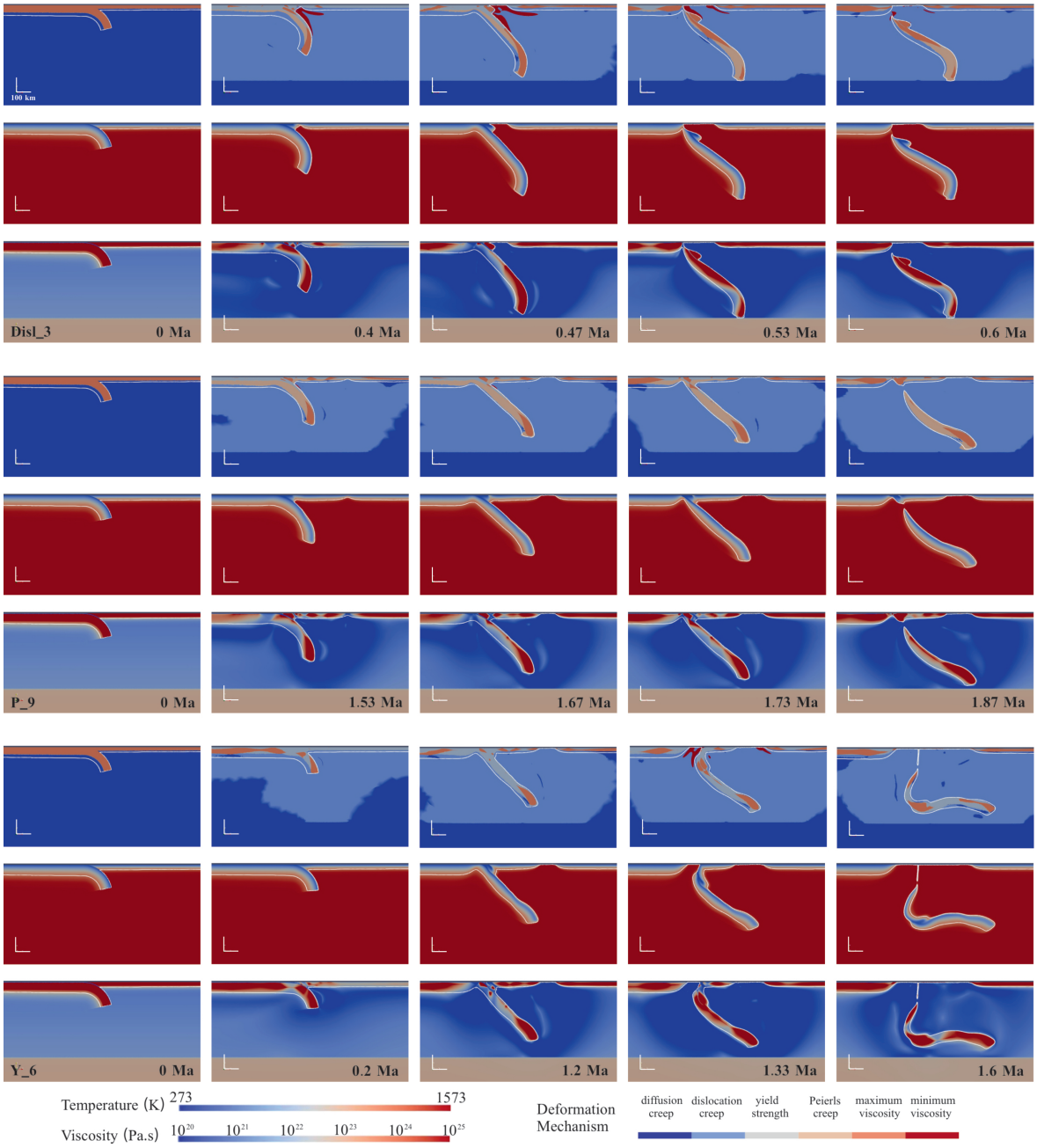

Figure 4.16: Simultaneous snapshots of a zoom-in of 3 cases which show SP detachment from Disl, Peierls and Yielding series of models showing the time evolution of dominant deformation mechanism (a, d, g), temperature field (b, e, h), and viscosity field (c, f, I). The cases are 'Disl_9' (Mode FE-D), P_9 (Mode BE-D), and Y_6 (Mode OPSPD). All snapshots show the isothermal contour of 1300 K in white.

SP detachment and folding are both shown to form from a relatively malleable SP.

The difference is that SP detachment is the result of a specific area of the SP being extremely weakened, while SP folding indicates that the entire sinking part of the SP exhibits deformable characteristics. In the SP folding models, the SP sinks very quickly, always reaching the LM in less than 1 Myr, then it starts to fold up above the LM and finally penetrates into the LM. In addition, the SP exhibits a steep dip angle with the OP because of the fast sinking speed. In this study, the models with reduced diffusion viscosity by varying E_{diff} and A_{diff}. In the RM and other models in which the parameters of diffusion viscosity are not varied, the UM around the SP is dominated by dislocation creep. However, when the E_{diff} and/or A_{diff} is reduced, the lower diffusion creep takes over the dominating role in this domain, so that the sinking velocity of the SP is enhanced by mantle lubrication through diffusion creep. Furthermore, after the quick trench retreat in some SP folding models within the initial 1 Myr, some models then show a brief period of trench advance (Figure 4.17), which never emerges in other modes. The reason is that the SP is not stiff enough to push the trench backwards.

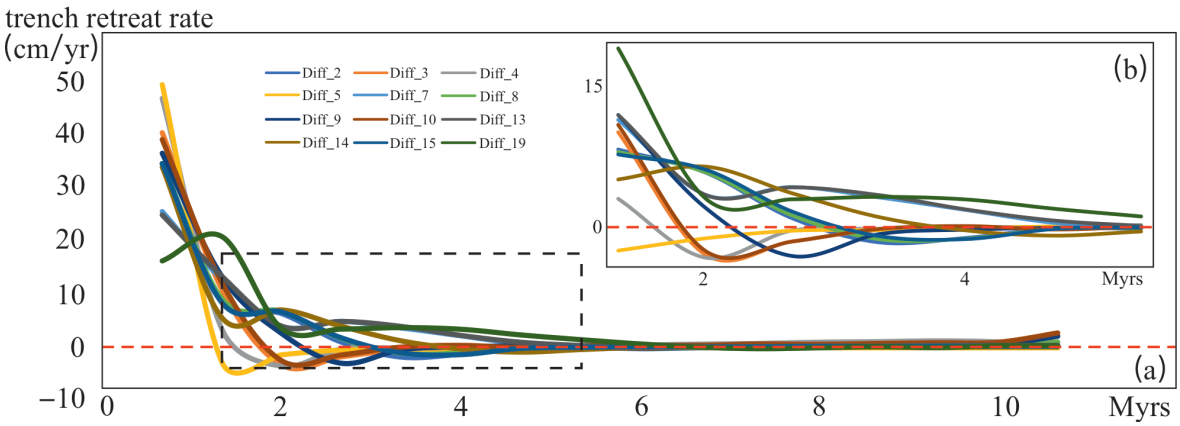

Figure 4.17: Trench retreat rate throughout the first 10 Myr simulations in models showing SP folding mode. The positive value means that the trench is retreating, and the negative value shows that the trench is advancing. The red dashed line represents no trench motion.

According to the results stated in Section 4.3, different SP morphologies might in-

fluence the OP deformation. For example, an SP folding inhibits the OP extension even though the OP viscosity is also reduced by diffusion creep. Slab folding serves as a barrier for the continuous sinking of the SP into the mantle. As the SP folds, it affects the slab pull, which is a significant driving force for plate tectonics (Conrad and Lithgow-Bertelloni, 2002). A weakened slab pull due to folding can lead to reduced forces acting on the OP, causing variations (e.g. decrease) in its deformation. Furthermore, the feedback between the SP folding and the OP deformation is dynamic. As the SP folds more prominently, the slab pull becomes more localised, influencing OP deformation. Conversely, changes in OP deformation might influence how the slab descends and folds, creating a complex feedback loop that could influence long-term tectonic evolution.

The animations of deformation mechanism field can be found in: https://cf-my.sharepoint.com/:f:/r/personal/zhangd27_cardiff_ac_uk/Documents/My%20Project/documents%20for%20thesis/figures/rheology_models/animations_deformation_mechanism/Deformation_mechanism_field?csf=1&web=1&e=zkx3bt.

4.4.2 Subduction zones on the earth – significance of the modes

The distinct influence of varying E_{diff} and plate age on deformation modes has potential applications in understanding past tectonic events. For example, by correlating the observations of subduction morphologies with the modes delineated in this study, one can potentially infer past mantle conditions, providing clues about the Earth's thermal and tectonic evolution.

Since Davies and von Blanckenburg (1995) proposed the concept of slab break-off, the reported SP detachments are almost all claimed to happen in continent-continent collisions (van Hunen and Allen, 2011). Although it seems like some modes in this study are unrealistic because the SP detachment is rarely found in the ocean-ocean

subduction zones on Earth, this deformation pattern, which ultimately leads to SP detachment, might be meaningful for some observations in nature. The Pacific slab under the Izu-Bonin trench shows a typical inclining mode in the E–W direction, but its morphology shown on the NW–SE cross-section is closer to the transitional mode between SP inclining and detachment (She et al., 2023). It could be assumed that the turning location of the slab has gone through weakening near the trench before it sinks. Furthermore, another characteristic of this slab is that it is lying over the LM, but no model shows this behaviour in this thesis, the SP tip always penetrates the LM after millions of years in this study.

In the context of these investigations, a geodynamic phenomenon categorised as SP folding is identified. Intriguingly, this mode appears to have strong parallels with the SP buckling behaviour documented in prior studies using seismic tomography techniques. Both the Mariana and Tonga-Kermadec subduction zones show that the sinking slabs are buckling from the transition zone to the LM with a steep angle (van der Hilst, 1995; Schellart and Spakman, 2012; She et al., 2023), highlighting its potential prevalence in such tectonic environments. Meanwhile, they are typical subduction zones with back-arc basins. However, the results in Section 4.3.1 show that a folded slab is to the disadvantage of back-arc extension (Figure 4.2), and there is no deformation on the OP in most cases with SP folding. Only a few cases show back-arc extension and SP folding together when the diffusion creep viscosity is not low enough to produce an NF mode (calculated by E_{diff} and A_{diff}), and a few more models show back-arc thinning as the diffusion viscosity decreases. Diff_18 and Diff_25 are the only two cases that show both SP folding and back-arc extension, behaviour consistent with the Mariana and Tonga subduction zones. They also show a little trench advance after rapidly retreating for a few Myrs. The trench retreat rate in the Tonga subduction zone is the highest on Earth (about 12–16 cm/yr calculated from different plate velocity reference frames,

Schellart et al. 2008), which is consistent with the high trench retreat value during back-arc extension in Diff_18. In contrast, the Mariana Trench may be not retreating anymore but advances slowly at about 1.5 cm/yr by the calculation in Schellart et al. (2008), which can also be compared with Diff_18, but it is going through a different stage from Tonga. Actually, because of the different ways of calculating the kinematic velocity of a geological unit, whether the Mariana trough retreats or advances (Carlson and Mortera-Gutiérrez, 1990) is still debated. However, certainly, the Mariana Trench is not retreating a lot currently.

I should at this point remind the reader that there are many limitations in the modelling, and it might be too early to compare to nature; for example, most of these models have only just reached the LM, while many subduction zones clearly show subduction deep into the LM. So before pushing these speculative early comparisons too hard, the work would benefit from further advances, including moving into 3 dimensions.

4.4.3 Insights of the rheology parameters from the modes out of the reality

The models in this study reiterate the importance of accurate parameterization when attempting to replicate real-world tectonic behaviours. Even small changes in parameters like activation energy can significantly alter predicted outcomes, underscoring the need for precision in laboratory experiments and model setups.

I will now speculate about the possibility of constraining (if only weakly) rheological parameters by comparing models with observations – with us needing to remember the limitations mentioned at the end of the previous subsection. Although the range of rheology parameters values investigated in my models are not as wide as the exper-

imental values, they still demonstrate various modes of model behaviour shown in the regime diagrams (Figures 4.2, 4.5, 4.8 and 4.11). Not all the modes find their counterparts in reality. Some modes are reasonable mechanically, but do not seem to exist in observations by geophysics and geology such as SP detachment in an ocean-ocean subduction zone.

The results show that a folded SP and back-arc extension are less likely to exist in a single model, and they only together in a very narrow range of combination of E_{diff} and A_{diff} (Figure 4.2). When the diffusion creep viscosity decreases further, the SP folds more and the extension on the OP vanishes. However, a folded SP which has a steep dip angle is always observed with a back-arc extension (van der Hilst, 1995; Schellart and Spakman, 2012; She et al., 2023), which probably means that the combinations of E_{diff} and A_{diff} in the pure yellow domain (Figure 4.2) are less likely to exist in nature. Given the A_{diff} set in my models is relatively small (Karato et al., 1986; Hirth and Kohlstedt, 2003), to combine with a larger A_{diff}, the estimated E_{diff} should be greater than 300 kJ/mol approximately, which is consistent with the experimental estimations of dry olivine (Karato et al., 1986; Hirth and Kohlstedt, 2003).

Another plate behaviour which helps constrain parameters is the SP detachment as mentioned above. An SP never breaks off in an ocean-ocean subduction zone, which phenomenon is shown in models changing dislocation creep, Peierls creep or yielding strength. This contradiction means that the parameter combinations at the yellow domain in Figures 4.5, 4.8 and 4.11 are not sensible estimations. For dislocation creep, both E_{disl} and A_{disl} vary a lot in the laboratory experiments (Chopra and Paterson, 1981, 1984; Karato et al., 1986; Hirth and Kohlstedt, 1996, 2003; Jain et al., 2019; Burov, 2011; Keefner et al., 2011). The scale of A_{disl} varies from 10^{-18} to 10^{-13}, and E_{disl} varies from 138 to 535 kJ/mol. Because there is no (or few) data of E_{disl} over 535 kJ/mol, and the experimental estimations show a downward trend which is under

500 kJ/mol in recent years due to the consideration of factors such as water content and oxygen fugacities (Keefner et al., 2011; Tielke et al., 2017), using an A_{disl} less than 1×10^{-15} (see Figure 4.5) in numerical modelling is more sensible. Similarly, the E_P and A_P can be constrained as well. Unfortunately, only a few researchers tried to measure these parameters for Peierls creep (Karato, 1997), and they got the value of E_P approximately 540 kJ/mol. Using this value, A_P is hard to be limited in a relatively small range. For yielding, a friction coefficient greater than 0.16 would be fine in models. However, experiments show lower values for a dynamic friction coefficient, which are mostly lower than 0.1 (Korenaga, 2020; Nakagawa and Karato, 2021). These values might be relevant at the shallow slab interface, where I introduce the weak material with its lower friction coefficient of 0.02.

The parameters of only one deformation mechanism are varied at one time in this study. There is uncertainty since the parameters could influence each other if the parameters of more than one deformation mechanism were changed simultaneously.

4.4.4 Limitations

One of the aims of this chapter is to constrain the range of rheology parameters by comparison to observations in nature, so covering as many geodynamic phenomena as possible is important. Indeed, the models lack some plate behaviours, for example, they do not show flat subduction in this chapter, which is a quite common SP behaviour around the Pacific in nature (Gutscher et al., 2000; van Hunen et al., 2004). This might be the result of not having imposed velocities, for example of the overriding plate. Of course, showing all the phenomena on Earth is not realistic. In addition, the OP in these models is very mobile, the OP is more likely to have an extension when the OP is not that mobile on Earth.

Limiting the variation of variables in this chapter limits the range of behaviours I

observe. When the parameters of a single deformation mechanism are changed, the parameters of others remain the same. It is a beneficial way to investigate the effect of every parameter, but limits the testing for the combination of rheology parameters. Additionally, n, the stress exponent of dislocation creep remains the same in all models. Its value seems uncertain with values that vary from 2.5 (Tielke et al., 2017) to more than 7 (Jain et al., 2019) from laboratory experiments, but most experiments show values of 3–3.5, which the value used in this study is consistent with (3).

A homogeneous OP is a limitation of accurately simulating the differential stress distribution within the plate. The stress state in an OP is influenced by its heterogeneity, which affects the initiation and propagation of faults, as well as the localization of strain, all of which are critical aspects of back-arc extension.

4.5 Conclusion

The results present findings from a series of models examining the effects of different rheological parameters on the OP deformation in a subduction zone. The study involved altering the activation energy (E) and prefactor (A) for diffusion, dislocation, and Peierls creep viscosities in the oceanic mantle, as well as varying the friction coefficient and maximum yield strength for models investigating yielding. The influence of initial plate ages was also considered, showing that viscosity is more sensitive to activation energy changes.

The study reveals that rheology plays a critical role in governing the mechanical behaviour of both the OP and SP. Key findings include the identification of the critical thresholds for various rheological parameters, beyond which the nature of back-arc extension significantly changes. The models demonstrate that variations in viscosity, temperature, and mechanical layering within the lithosphere can lead to different

modes of extension. Furthermore, the research highlights the sensitivity of subduction dynamics to changes in rheological properties. It is observed that minor alterations in parameters like viscosity contrast and thermal structure can lead to substantial differences in the extent and location of back-arc extension. This sensitivity underscores the need for constraints of rheological properties in geodynamic models.

In diffusion creep models, varying the parameters in UM altered the dominant deformation mechanism and composite viscosity. As diffusion creep viscosity changed, different behaviours in the SP and OP were observed. The SP displayed two end-member morphologies: inclined SP with minor bending (I) and steep SP with strong folding (F). The OP showed three degrees of deformation: no deformation (N), back-arc thinning (BT), and back-arc extension (BE). Various modes of deformation were identified, including NI, BT-I, BE-I, BE-F, BT-F and NF as the diffusion creep viscosity decreased, demonstrating a continuum of possible outcomes rather than distinct modes.

In dislocation creep models, decreasing viscosity led to different behaviours than in diffusion creep models. When the dislocation creep viscosity is high, the rigid SP inclines (I) as that in diffusion creep models. Lower dislocation creep viscosity resulted in slab detachment (D) at shallow depths, another end-member SP behaviour. This process varied significantly from diffusion creep, where decreasing parameters resulted in slab folding. Several modes of OP deformation were observed, including no deformation (N), back-arc thinning (BT), back-arc extension (BE), and fore-arc extension (FE). The identified modes of plate behaviours are NI, BT-I, BE-I, BE, BT-FE, FE, and FE-D.

Peierls creep models showed that both plate deformations to changes in Peierls creep viscosity were not as sensitive as that in diffusion and dislocation creep viscosities. Two new modes of SP behaviour were observed, one of them is that the remaining slab continued to subduct after initial detachment (BE-DS), and the other is that

the near-trench part of the OP breaks off following the detached SP after back-arc extension (BE-OPSPD). Back-arc extension was common in models with decreased Peierls viscosity, differentiating them from dislocation models where fore-arc extension was more prominent, and also from diffusion models where no extension occurs. The identified modes in decreasing order of viscosity are NI, BT-I, BE-I, BE, BE-D, and BE-OPSPD.

The yield strength models revealed that the friction coefficient played a more significant role in plate behaviour compared to maximum yield strength. Lowering the friction coefficient resulted in rapid SP tip detachment and new subduction processes. Various combinations of SP and OP behaviours were identified in these models: NI, BT-I, BE-I, BE, N-DS, and D-BE-D. N-DS and D-BE-D are not currently observed on Earth.

Extension in a homogeneous OP results from the interaction between basal drag, which causes thinning, and thermal healing, leading to thickening. Plate age initially determines the thermal structure, but adjusting rheological properties like activation energy (E), prefactor (A), friction coefficient (fc), and yield strength (yld_{max}) modifies the plate's rheology, impacting its thermal state. Dominant basal drag can induce thermal weakening and reduce viscosity, but this does not always extend the OP. Without extension (NE mode), thermal healing dominates, either due to weak basal drag or a particularly strong OP. For modes involving extension near the trench (FE) and away from it (BE), the location of Extension hinges on where thermal weakening outweighs—near the trench for low dislocation viscosity or in the back-arc region when dislocation resistance is relatively high but not high enough.

This study underscores the critical role of precise rheological parameterisation in modelling tectonic behaviours, small adjustments in parameters such as activation energy significantly impact the simulation outcomes. Comparisons between model pre-

dictions and geological observations offer a method to tentatively constrain rheological parameters to some extent, though they are not always directly observable in nature. For instance, the SP detachment in ocean-ocean subduction is rarely represented in models and observed reality, suggesting that some parameter combinations may not occur naturally. Parameters derived from laboratory data provide a range of plausible values that improve model realism, acknowledging the complexity of interactions when multiple parameters are varied. This research points towards a nuanced understanding of subduction processes, reliant on carefully calibrated rheological models.

Overall, the insights gained from this research not only aid in interpreting geological phenomena associated with subduction zones but also provide valuable constraints for future modelling efforts aimed at unravelling the complex processes governing plate tectonics.

My models have all used a homogeneous OP so far, but a real OP is never homogeneous and this property probably influences the occurrence and the location of back-arc extension. Thus, an inhomogeneous OP will be investigated in the next chapter, specifically investigating a hot zone mimicking the role of an arc.

Chapter 5

Investigating the role of an arc in back-arc extension

A version of this chapter has been accepted to Solid Earth and the Doi is https://doi.org/10.5194/egusphere-2023-1791.

5.1 Introduction

Even though BABs are all referred to as 'back'-arc basins, most of them were formed by breaking volcanic island arcs apart, leaving a remnant arc on the other side of the basin, such as Lau Basin which was formed by splitting Tonga Ridge and Lau Ridge apart (Sclater et al., 1972; Gill, 1976; Zellmer and Taylor, 2001), Havre Trough between Kermadec Ridge and Colville Arc (Karig, 1970; Ballance et al., 1999), Mariana Trough between Mariana Arc and West Mariana Ridge (Karig et al., 1978; Oakley et al., 2009), etc. This phenomenon demonstrates that the presence of a volcanic arc can be important for constraining the location of extension, but few studies have taken this into account (Baitsch-Ghirardello et al., 2014). To investigate this further, I have in this

study run a series of 2D thermo-mechanical and self-consistently driven models with a hot region that simulates a thermal volcanic arc on the OP. I will interchangeably use the terms volcanic arc / arc / hot zone knowing that readers understand that this is shorthand for approximating the effect of an arc with a hot zone. Firstly, I tested a series of models which have homogeneous overriding plates (OP) without arcs for comparison. Then, an arc was introduced into the OP to investigate its role in back-arc extension. I aim to look into how an arc influences back-arc extension and its position.

A remaining issue is that the properties of a volcanic arc are not very well known. Even though the location of present-day arcs is known from the Smithsonian Global Volcanism Project database, the arc-trench distances range widely from 2–1539 km data from Earthbyte (Jodie, 2016). Additionally, the temperatures of arcs before their extension are difficult to constrain. Thus, I introduced a simplified model for the thermal signature of an arc, which allowed us to test a range of parameters for the arcs (including their width, arc-trench distance, and the central temperature anomaly) systematically to figure out their roles in back-arc extension.

5.2 Model description

High heat flow has been observed in active volcanic arcs (Manga et al., 2012), so arcs can be expected to be described by a relatively high temperature. In the initial thermal structure, a hot region has been introduced on the OP to simulate the volcanic arc (Figure 5.1). The temperature at a chosen distance (from 100 to 1050 km) from the trench is increased by a certain degree (from 25 to 800 degrees) vertically from the mantle depth (which varies with the age of OP) to the surface. It cools off by a linear function over a prescribed horizontal distance (named 'Width', from 10 to 50

km) to merge in with the background temperature. The mantle temperature limits the maximum value, which is 1300°C. The hot region extends in depth from the surface to where it reaches the maximum temperature. The hot region has a higher temperature than the background, so its viscosity is lower as well (producing a pre-existing weak zone in the OP at the start of the simulation). All parameters of each rheology are the same as that in the reference model (RM).

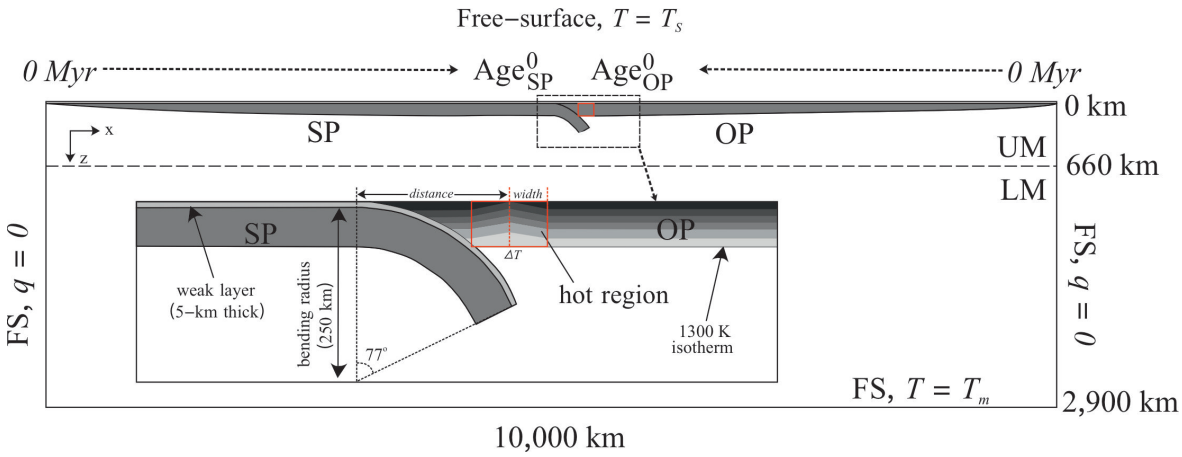

Figure 5.1: Model setup and initial geometry of the subduction simulations with the initial thermal structure of the hot region (adapted from Garel et al. 2014).

5.3 Results

Two sets of models with a hot region were run to test the role of properties of a hot region (Table A.5) and plate ages (Table A.6), respectively. Before that, I run models that only vary initial plate ages for comparison with those that contain a hot region on the OP (Table A.6). The naming of the models depends on the parameter types and is shown in Tables A.5 and A.6.

Model SP90_OP20 (Age^0_{SP} is 90 Ma and Age^0_{OP} is 20 Ma) without a hot region was chosen as a reference model (RM, Figure 3.2) for testing properties of the hot region.

The subducting plate (SP) sinks rapidly and reaches the boundary between the upper mantle (UM) and lower mantle (LM) at about 4 Ma after model initiation. During this time, the OP basement near the trench is eroded by the mantle wedge flow, and the region that is about 750 km away from the trench on the OP becomes thinner, a region which is under extensional stress (Figure 3.2d). After the SP tip reaches the LM which is more viscous compared to the UM, its subduction slows down due to the increased resistance, which leads to the subduction process becoming steady state (Capitanio et al., 2007). The thinning region of the OP lithosphere heals gradually during the steady state subduction stage, after which time the whole OP is under a compressional environment. The trench retreats all the time though the rate of retreat varies. The models that tested the effect of the properties of the hot region are all set the same Age^0_{SP} and Age^0_{OP} with the RM (Table A.5).

5.3.1 Back-arc extension modes

Based on the above definition of Extension (in Section 3.4, three end-member modes of back-arc extension on the OP are recognised (Figure 5.2): (A) No Extension on the OP (NE), which means there is no actual spreading on the OP; (B) Extension at the far-field location (around 750 km from the trench) which is far away from the hot region and the very same region where the thinning takes place in the RM (EF); (C) Extension at the Hot region (EH, EH-D). I also get the fourth mode (D) which has two (dual) extensions, i.e. at both places in modes B and C (EF+EH). The ones showing slab detachment after the back-arc extension have been subdivided into EH-D (Figures 5.2g, h), for the case in which the slab breaks off, in these cases, the plate loses its slab pull and both the subduction and trench retreat stops. The extension of all modes lasts for a short time (just 1 to several Myrs) and then heals gradually in the steady

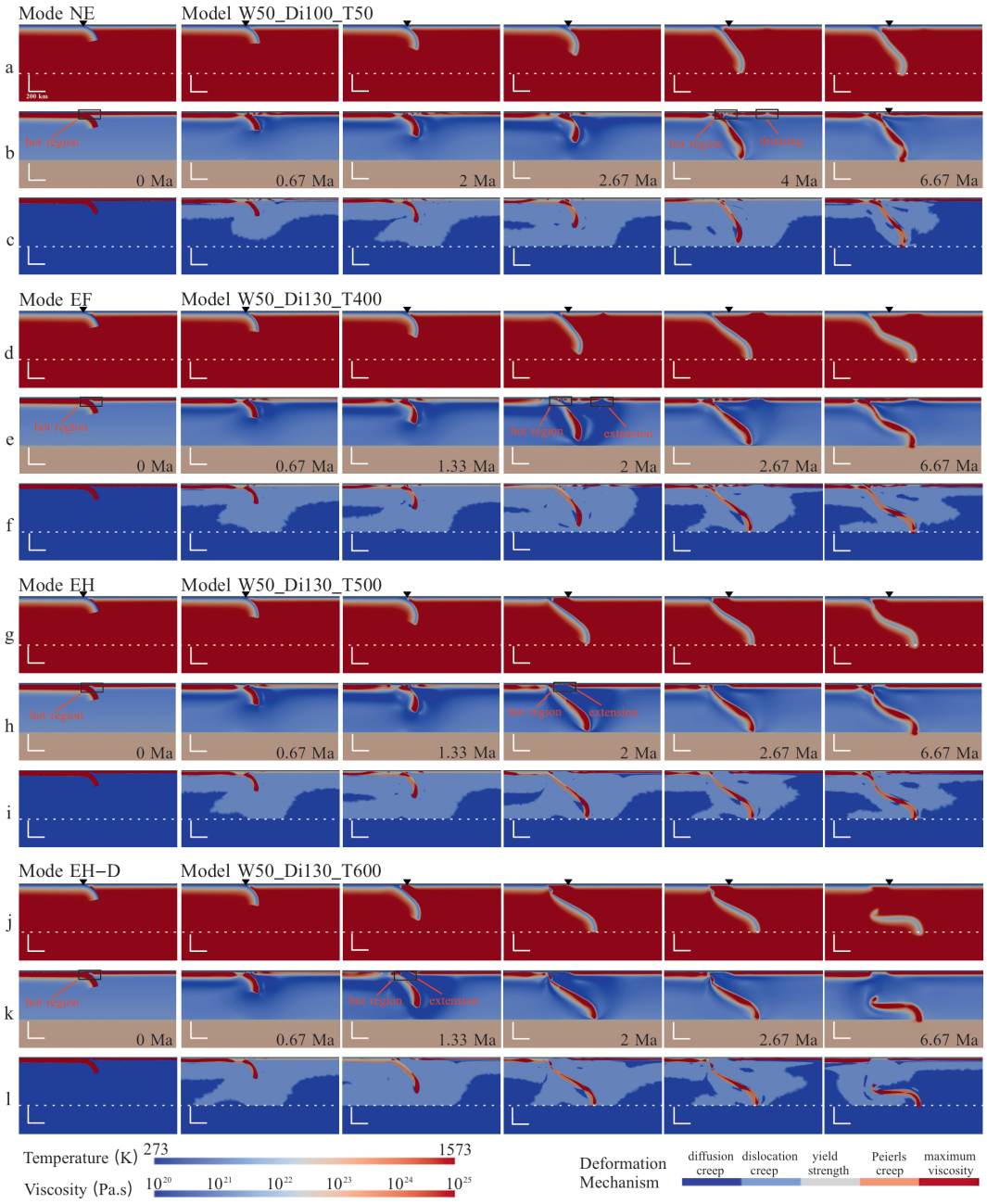

Figure 5.2: Four modes of the back-arc extension on the OP: (a)(b) NE, (c)(d) EF, (e–h) EH (including EH-D which shows slab detachment in (g)(h)), (i)(j) EF+EH. (a) (c) (e) (g) (i) show the temperature field with the isothermal contour of 1300 K in white, while (b) (d) (f) (h) (j) show the viscosity field, respectively. The parameters of each model are shown in Table A.5. For example, in Model hSP90_OP20, Age^0_{SP} is 90 Myrs and Age^0_{OP} is 20 Myrs, 'h' means a hot region is included. W50_Di130_T400–600 means that Width is 50 km, Distance is 130 km, ΔT is 400, 500 and 600°C, respectively.

subduction state or after slab detachment (in EH-D mode).

The reason why I combine EH and EH-D into the same mode is that the slab detachment occurs after the back-arc extension and has no effect on driving the extension. The specific morphology is not the primary focus of this research.

5.3.2 Varying parameters of the hot region

More than 200 models have been performed by varying the following parameters of the hot region: the distance from the trench to the centre of the hot region (Distance), the width from the heated centre of the hot region to each side (Width), and the increased temperature at the centre of the hot region from the background temperature (ΔT, shown in Figure 5.1 and Table A.5), to investigate the influence of a pre-existing hot region (a volcanic arc) on back-arc extension.

5.3.2.1 Regime diagrams

In this section, I mainly show how the modes change through changes in the above parameters (Figures 5.3, 5.5).

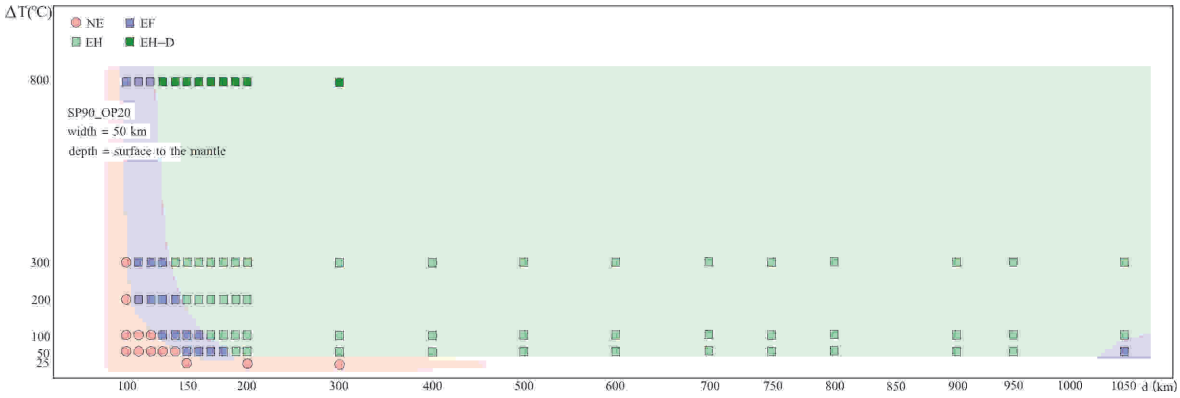

Figure 5.3: Regime diagram showing the Extension behaviour of the overriding plate (OP) with a hot zone. It is a function of the distance from the trench to the centre of the hot region (d, km) and the temperature anomaly of the hot region (ΔT). The width of the hot region is fixed at 50 km.

Firstly, the Width was fixed to 50 km and the Distance and ΔT were tested systematically (Figure 5.3). All of the modes I introduced in Section 5.3.1 are identified in this series of models. When the hot region is quite close to the trench, such as when the Distance is 100 km, the model behaves as mode NE (No Extension) no matter how hot the hot region is. As the hot region is emplaced farther away from the trench, an extension emerges at the far-field location (mode EF). When the ΔT is prescribed to 50 degrees, Extension cannot appear if the distance is less than 150 km. Whereas when the thermal anomaly is increased to 100 degrees, the Extension occurs even when the distance is only 130 km. In other words, the distance threshold controlling the emergence of Extension on the OP reduces as the temperature of the thermal anomaly increases.

As the distance increases further, the mode of the cases changes from EF to EH, which has Extension at the hot region close to the trench. The threshold of distance, controlling the transition from mode EF to EH, has the same trend as that controlling the existence of Extension. When the distance is larger than the threshold, most of the cases show mode EH as long as there is an Extension. However, model W50_Di1050_T50 (W50 means that the Width is 50 km, Di1050 represents the Distance is 1050 km, and T50 means that the ΔT is 50 degrees) shows mode EF unexpectedly (Figure 5.4). In this model, the hot region is located at 1000–1100 km from the trench, but the Extension is still around 750 km from the trench. When the hot region is very close or very far away from the trench, the Extension could emerge near a distance of around 750 km from the trench.

To find out the role of the Width, I reduce it from 50 km to 25 km. A series of cases investigate how the combination of the Distance and ΔT changes the extension behaviour of the different-width hot region (Figure 5.5). The depth extent of the thermal anomaly has not been changed in these models. Compared to Figure 5.5a, the

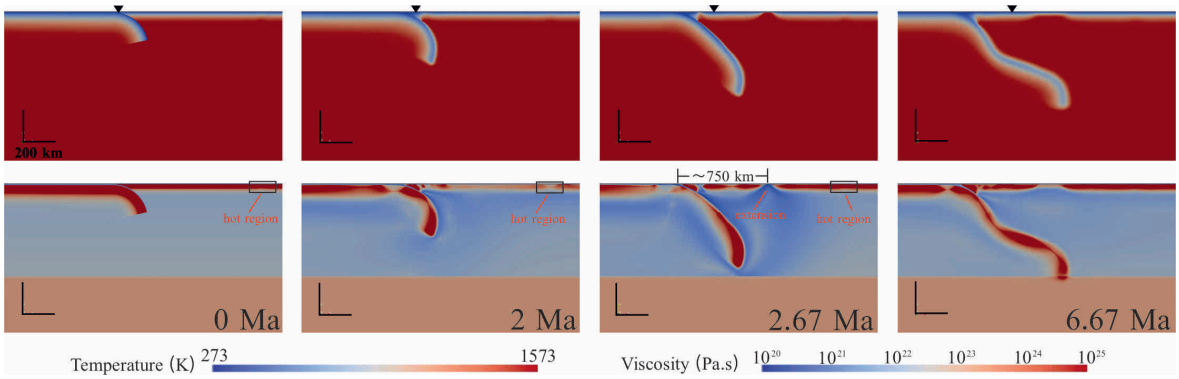

Figure 5.4: Evolution of model W50_Di1050_T50 (temperature field and viscosity field), a special case in EF mode which shows Extension between the trench and the arc.

results in Figure 5.5b show that the thresholds between mode NE and EF, as well as mode EF to EH in distance and heating temperature both increase obviously. Take models with 100 degrees temperature increase for example, when the distance is 150 km, the model with a width of 50 km shows EF mode which has an Extension on the OP, but the model with a width of 25 km is in NE mode which does not show Extension on the OP. Regardless of the specific values, the tendency of the changes in threshold when the width is 25 km is the same as that with a width of 50 km. In summary, as one might expect, a wider hot region favours Extension.

In conclusion, a farther distance from the heated centre to the trench, a higher temperature, and a larger size of the hot region all favour back-arc extension on the OP.

5.3.2.2 Correlation to the trench retreat rate

The models with a fixed Distance of 130 km in Figure 5.3 are chosen to investigate the influence of the ΔT. The ΔT varies from 50 to 800 degrees, and the modes that they show transfer from NE to EF, then to EH as the ΔT increases.

As stated in the description of the Reference Model (RM), the SP sinks rapidly

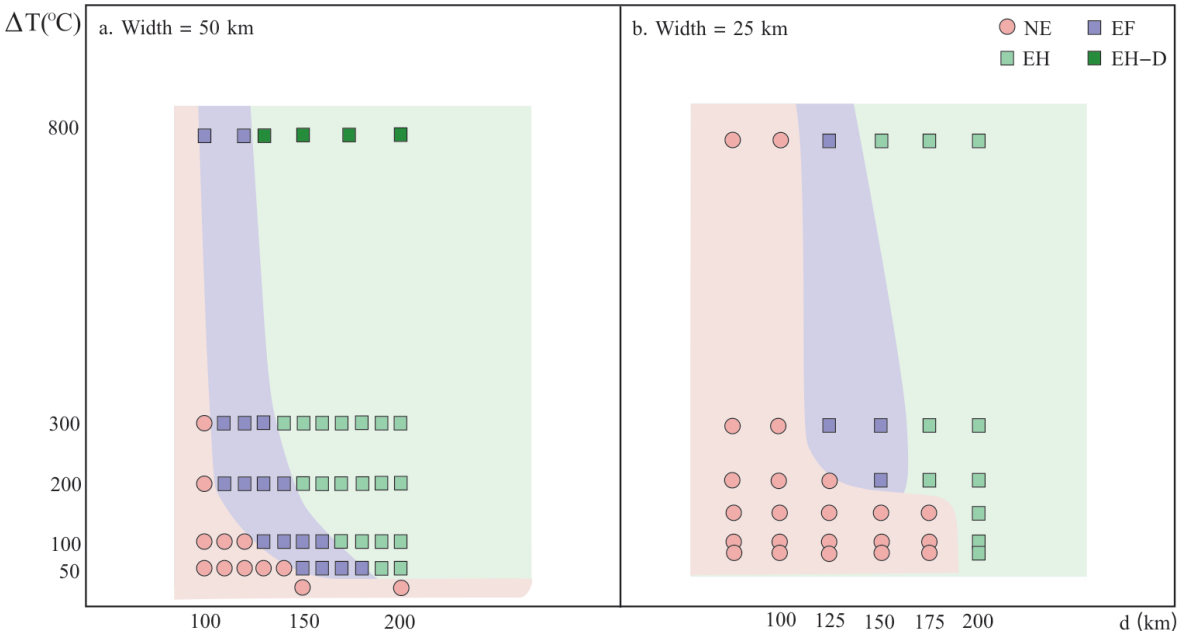

Figure 5.5: (a) Regime diagram of distance vs. ΔT when the width is 50 km and (b) the comparison to the results when the width is 25 km.

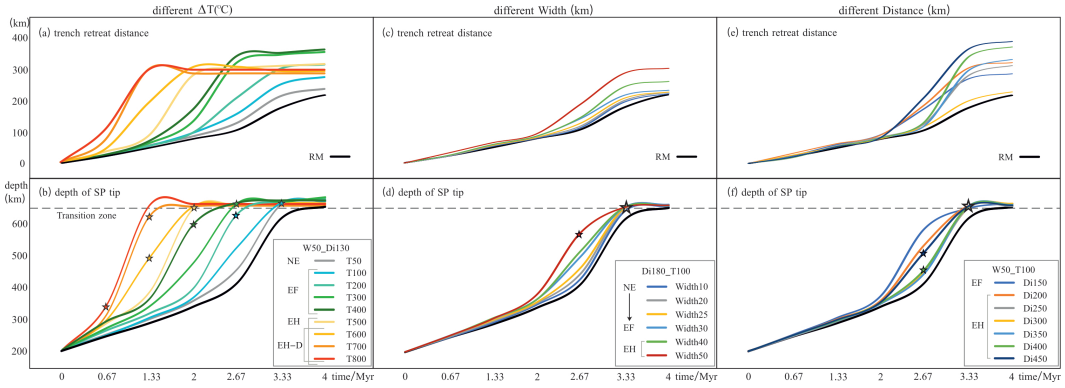

Figure 5.6: Comparisons of total (a) (c) (e) trench retreat and (b) (d) (f) depth of SP tip subduction throughout the first 4 Myr simulation with various ΔT (a, b), different Width (c, d) and various Distance (e, f), respectively. The grey dashed line represents the transition zone depth (660 km). The stars mark the time when the Extension occurs in each model, and the colour of the stars is the same as the lines of each model. The reference model (RM) is marked as the black dashed line.

initially, accelerating until the tip reaches the transition zone between the UM and the LM. After introducing a hot region into the OP, the SP sinks more rapidly on average and the trench retreats slightly faster before the SP reaches the LM than in the RM. When the ΔT increases, the general SP sinking rate also rises, and the SP tip takes less time to get to the transition zone (Figure 5.6b). Like the vertical slab sinking rate, the trench retreat rate shows a similar trend as ΔT increases (Figure 5.6a). When the ΔT is no more than 400 degrees, the trench retreats at a similar speed at first, then the model with a hotter 'arc' shows a quicker trench retreat, after 3.33 Myrs, the trench keeps quite a slow retreating rate in the steady state stage. As the ΔT is increased further, the trench obviously retreats faster before the SP reaches the transition zone. The trench stops retreating after the slab detachment in Mode EH-D, because there is no extra force exerted on the SP.

Similarly, when the Width rises, both the SP rate and trench retreat rate slightly increase with the same trend as when ΔT increases (Figures 5.6c, d), though the increase with Width is much less than with ΔT. However, there is no specific correlation between Distance and trench retreat rate (Figure 5.6e) / SP sinking rate (Figure 5.6f). For example, compared to model W50_T100_Di300 showing the slowest trench retreat rate except for the RM, the trench in model W50_T100_Di200 retreated more quickly and farther until 4 Myrs.

Whether increasing the Width or ΔT, the hot region is hotter and weaker in total, which encourages the trench retreat by providing less horizontal resistance to the trench rollback. Whereas varying the Distance alone has no influence on the trench retreat since the heated area and temperature are unchanging. Besides, the EH-D did not occur in the two latter series of models, which possibly means that the ΔT has the most significant influence on the behaviours of the plates.

5.3.3 Varying initial plate ages adjacent to the trench

I chose the hot region located 100–200 km from the trench and heated it by 200 degrees (the same as that in Model W100_Di150_T200), and tested how different combinations of plate ages influence the OP deformation (Table A.6). The results of changing the initial OP age and SP age at the trench, showing the modes of the OP deformation, are shown in Table A.6 and Figure 5.7. In general, the figure reveals that older SP age tends to result in Extension when the OP age remains unchanged, whereas a younger OP age leads to Extension when the SP age is fixed.

In models without a hot region (modes changing shown by the dashed line), when the initial age of the OP adjacent to the trench (Age^0_{OP}) is prescribed to be 20 Ma, the threshold of the initial age of the SP at the trench (Age^0_{SP}) that leads to Extension is 100 Ma (Model SP100_OP20), and a little bit of thinning occurs at the place where Extension exists in Model SP100_OP20 if the Age^0_{SP} is decreased to 90 Ma (Model SP90_OP20). I change the Age^0_{OP} and find the minimum Age^0_{SP} to generate Extension for each Age^0_{OP}. As seen in Figure 5.7, model SP60_OP15, SP95_OP20, SP165_OP25, and SP280_OP30 are the marginal cases in the region in which the models have Extension. As Age^0_{SP} increases from 70 Ma to 280 Ma, the time before Extension occurs gets slightly longer, from 2.7 Ma to 4.7 Ma (not shown here). For these three models, increasing Age^0_{OP} or decreasing Age^0_{SP} stops Extension. All of this extension or thinning happens at a far-field location about 700–750 km from the trench.

Adding a hot region increases the age threshold of the existence of Extension, which is shown by the boundary of the pink area and the dashed line (Figure 5.7), and allows Extension to occur at the hot region which is much closer to the trench than the far-field location. When the Age^0_{SP} is relatively young, Extension is more likely to happen at the arc, though some cases showed far-field Extension before adding the hot region (e.g. SP80_OP15 and hSP80_OP15, 'h' in the model name means a hot

region is set in the model). Most models with an Age^0_{SP} older than 100 Ma tend to lead to an EF mode. Furthermore, the transition modes in Figure 5.7 show how the end-member modes change when the initial plate ages near the trench vary. Take the OP20 series of models for example, when the Age^0_{SP} increases from a low value (such as hSP60_OP20 which is mode NE), Extension first occurs at the hot region (e.g. hSP70_OP20, mode EH) and at the far-field location (mode EF) when Age^0_{SP} is old enough (e.g. hSP150_OP20). Transitional mode EH+EF is shown in this process as well.

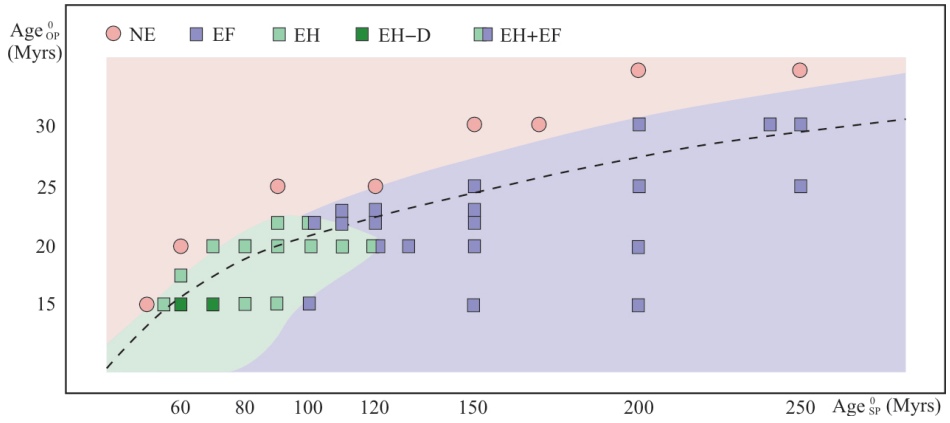

Figure 5.7: Regime diagram of the combination of Age^0_{OP} and Age^0_{SP} in models with a hot region located from 100 to 200 km from the trench. Each symbol represents a model, and the different colour regions are classified by the results of models with a hot region. For comparison, the threshold for the existence of extension in models without a hot region is marked by the black dashed line. Note that one symbol with two squares means two end-member modes both happen in one model.

5.4 Discussion

5.4.1 The driving mechanism of the back-arc extension

In Section 3.6, the driving mechanism of back-arc extension in models that do not have a hot region on the OP is discussed. The poloidal flow reduced by the trench

retreat is considered the main driving force for a back-arc extension in these models. This opinion can also be proved by the new results shown in this chapter.

The analysis of the horizontal stress shows a compressional region close to the trench just before the Extension occurs in all the models (Figure 5.8), which is consistent with that in RM (Figure 3.2d) and some previous research (Chen et al., 2016; Schellart and Moresi, 2013; Balázs et al., 2022; Corradino et al., 2022). The compressional stress accumulation on the forearc region is probably driven by vertical suction (resulting in horizontal compression) of the slab. Even though Extension in Mode EH occurs near the trench (orange star in Figure 5.8), the vertically integrated horizontal stress (Σ_h) shows no observable difference from that in EF mode. The introduction of the hot region has almost no influence on σ_h. Therefore, the change of Σ_h or σ_h does not really decide if Extension occurs, which suggests that the horizontal extensional stress is not the critical cause of Extension in my models. It is worth noting that these models have a mobile OP, facilitated by a ridge on the right-hand boundary, and the conclusion might be different for fixed OP.

The RM shows only very limited thinning at approximately 750 km away from the trench on the OP (Figure 3.2). To produce back-arc extension, either the OP needs to weaken or the driving force needs to increase. In this series of models, the OP can be weakened in two ways. One is through the hot zone which was introduced in the initial setup, because viscosity decreases as temperature rises (Eq. 2.6), the hot zone would be easier to extend; the other way it could be weakened is by upwelling flow beneath the OP. This latter process is really important in models which have a homogeneous OP (in Chapters 3 and 4), and it also must have occurred in this series of models, as implied by the existence of the EF mode. Thus, the main driving mechanism is also poloidal flow shown by the velocity field (Figure 5.9) as same as the previous models in this thesis.

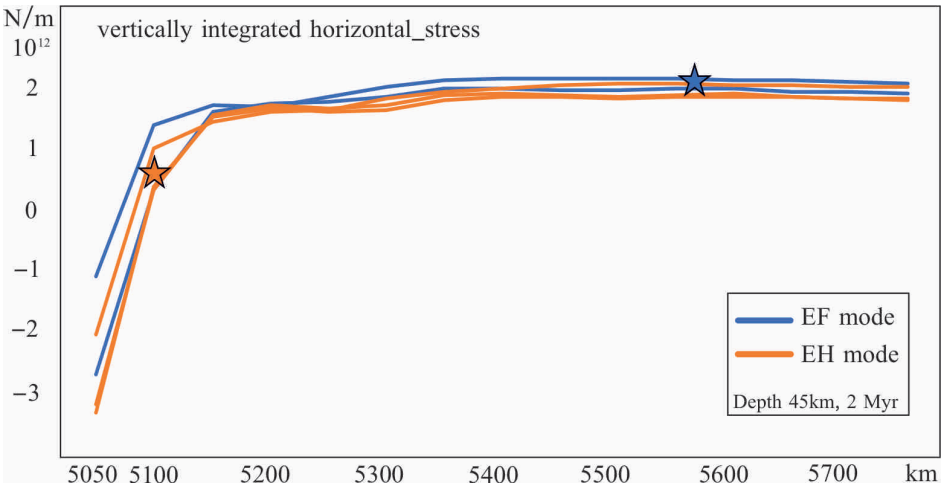

Figure 5.8: Vertically integrated horizontal stress over OP thickness (from the surface to the OP bottom, 45 km depth, which was defined by the temperature contour of 1300K) vs. x coordinate (the trench starts with an x coordinate of 5000 km). A positive stress value means extensional. For clarity, only two colours are used in this figure to represent models in different modes (see the legend). The chosen models are W50_Di120_T100 and W50_Di150_T100 which are in EF mode, W50_Di170_T100, W50_Di190_T100, and W50_Di250_T100 which are in EH mode. Stars mark locations of back-arc extension in the same colour as their plots (e.g. blue star represents the extensional location in EF mode), respectively. This is evaluated after 2 Myr in all simulations.

5.4.2 The role of an existing arc

In numerical models, the existence of an arc is not necessary to produce Extension in the OP (Figure 5.7, e.g. Sheng et al., 2019). However, the position of the Extension depends on the size of the mantle flow cell (about 750 km in these models) if the OP is homogeneous. A hot region on the OP not only facilitates the Extension to happen but also changes the position of the Extension under some conditions (Figures 5.3, 5.7). The specific mode that a model produces depends on different parameters, including properties of the hot region and plate ages in these cases. There have been many studies investigating back-arc extension (Sdrolias and Müller, 2006; Capitanio et al., 2010, 2011; Schellart and Moresi, 2013; Dal Zilio et al., 2018; Sheng et al., 2019; Dasgupta et al., 2021) and some have emphasised the balance of strength and forces that lead to extension and shown that the location of extension in the OP can be

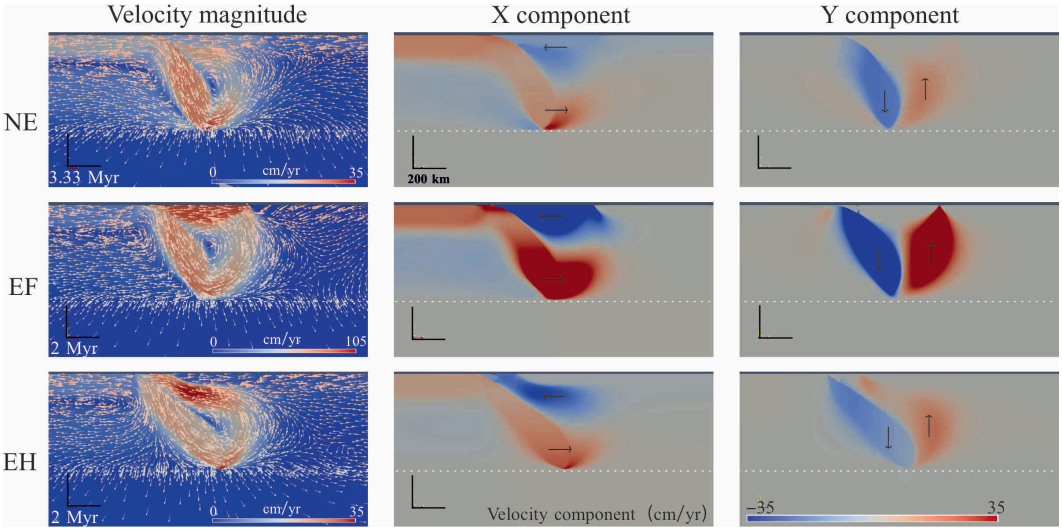

Figure 5.9: Velocity fields in 3 modes. The small arrows indicating the direction of the mantle flow are marked in the magnitude velocity field. In the velocity component field, the positive value represents rightwards (in the x component field) or upwards (in the y component field). The large arrows in the velocity component field show the velocity directions. The chosen time is just before the Extension (in Mode EF and EH) or Thinning (in Mode NE). Note that the scale of Velocity magnitude in Mode EF is set three times larger than that in other modes to improve figure clarity.

related to the flow cell in the mantle wedge (Dal Zilio et al., 2018). In this work here I similarly can find extension in a similar flow cell controlled location, but emplacement of a hot region can sufficiently weaken the OP to change the location of extension to this weakened region.

When the plate ages are fixed and the model shows Thinning but no Extension before a hot region is introduced, some models show Extension at the hot region (Mode EH), which means the hotter and weaker 'arc' is split apart; whereas some others show Extension at the same place as the thinning location even though the weakened zone is much closer to the trench (Mode EF), which implies the driving force (including the force which weakens the OP) is undoubtedly enhanced.

Thermal thinning gives thermal weakening, equally the hot region provides thermal thinning at the start of such simulations and encourages Extension. The Extension process is a competition of thermal weakening (reduced viscosity due to increased

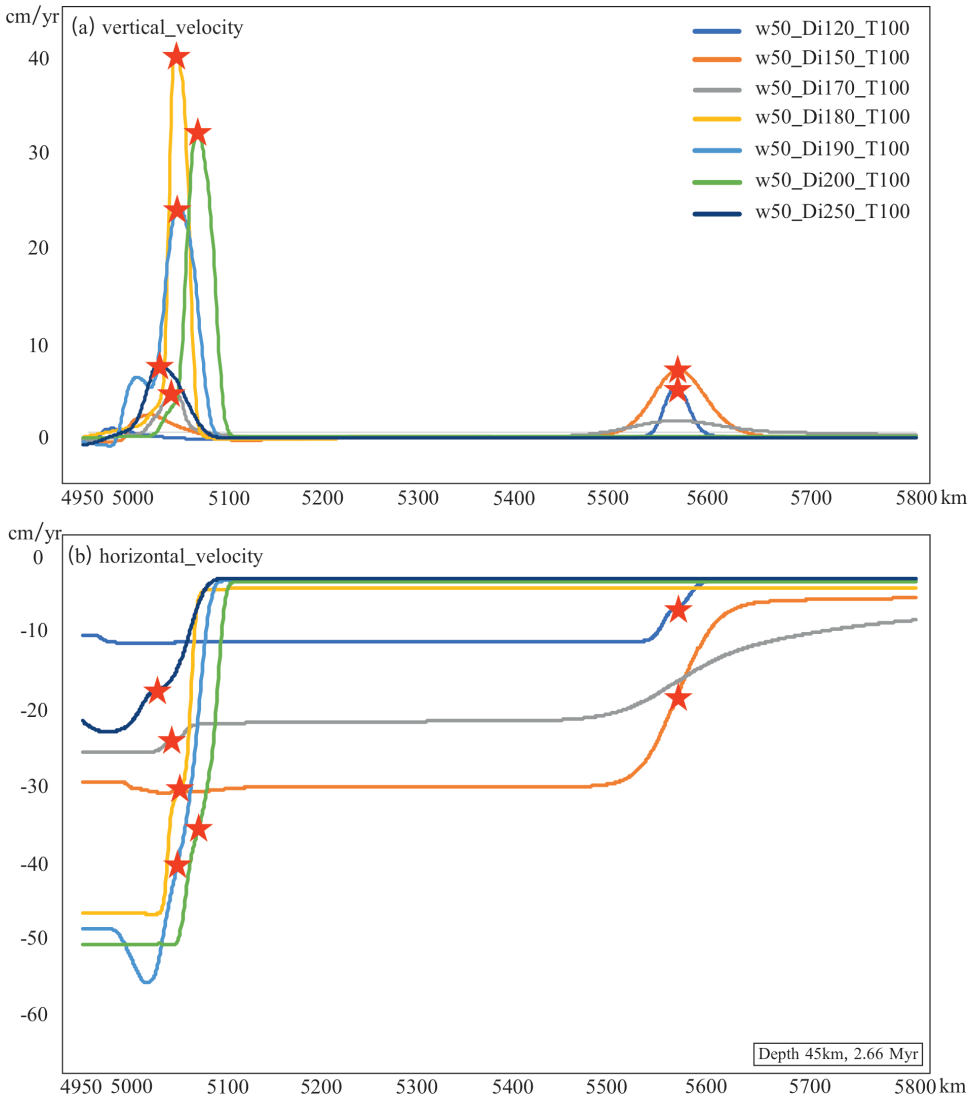

Figure 5.10: Velocity components vs. x coordinate at 45-km depth at 2.66 Myr. (a) Vertical velocity (Y component) vs. x coordinate, and (b) Horizontal velocity (X component) vs. x coordinate. The back-arc extension is marked by red stars. Models W50_Di120_T100 and W50_Di150_T100 are in Mode EF, the others are all in Mode EH.

temperature) at the hot region and at the far-field location. The former is mainly from the thermal thinning of the hot region itself, so it depends on the Width and ΔT (the viscosity is dependent on temperature which is shown in Eq. 2.6). The latter is from the mantle wedge flow, which is controlled by initial plate ages and Width and ΔT as well because faster trench retreat (Section 5.3.2) induces a stronger

mantle flow (Lei, 2022). The results show the contribution that Width and ΔT make to the thermal weakening of the hot region is greater than that to the wedge flow. The thinning is generated by thermal weakening. The thermal weakening draws in some flow because of the continuity of mass, which makes the hot region weaker and encourages more Extension. At the same time, the weakening accelerates the trench retreats and induces more wedge flow. When the mantle flow is firstly strengthened, the place which concentrates the flow at the far-field location is weakened and dragged by stronger basal traction no matter where the weak region is, which results in Mode EF. However, when the Width and ΔT are high enough, the thermal weakening in the hot region dominates the process, and the hot region becomes the region of Extension, which is Mode EH (Figure 5.9). At the same time, the flow going to the far-field location reduces because the upwelling focuses on the hot region, so the far-field location does not show Extension anymore. If the thermal thinning which the mantle wedge flow produces exceeds that produced by the hot region, then Extension occurs at the far-field location.

Different from the Width and ΔT, the Distance influences neither the trench retreat rate nor the size of the mantle flow. The upwelling flow is sucked into the edge of the flow cell and gradually decreases to each side (Figure 5.9). Compared to the reference model, the introduction of the hot region enhances the trench retreat rate and the slab subducting rate, so that the mantle wedge flow grows. However, the total thermal weakening in the hot area is limited when the hot region is close to the trench, because the extra weakening from the mantle flow is quite small. This leads to Extension at the far-field location where the growing mantle flow focuses, which results in thermal weakening exceeding that in the hot region. When the Distance increases, the hot region initially gets close to the cell edge and gains more upwelling intrusion. Hence, the hot region is increasingly weakened and attracts the mantle flow to itself. As

the Distance increases further, the hot region moves away from the cell edge, and the mantle flow fades away, so Model W50_Di1050_T100 changes to EF mode again (Figure 5.4). However, a larger trench-arc distance is always associated with a flatter slab in nature (Cross and Pilger, 1982), and there are positive correlations between the slab dip and back-arc extension so that a BAB would be rarely observed when the arc is relatively far away from the trench.

Figure 5.7 shows that when Age^0_{SP} is relatively young (e.g. 60–90 Ma), some cases which have an Extension at 750 km away from the trench with a homogeneous OP generate EH mode after adding the hot region. In these cases, a hot region largely weakens the OP and concentrates the flow at the weak zone though the arc also facilitates the mantle flow. When the arc is much easier to be broken than the far-field location for this mantle flow, the flow tends to focus on the arc and the far-field location loses the extensional stress. The high negative buoyancy and strength of an older SP encourage a higher trench retreat rate and a stronger mantle flow (Garel et al., 2014), so that the flow is strong enough to break at the far-field location before the weak zone is broken. Under such circumstances, the models show EF mode.

5.4.3 Comparison to observations in nature

Mode NE (No Extension), Mode EH (Extension at the Hot region) and Mode EF (Extension at far-field location) are identified as three end-member modes (Section 5.3.1). In nature, similar behaviours to Mode NE and Mode EH are shown in many subduction zones. For example, the Lesser Antilles subduction zone does not show back-arc extension on the OP (Caribbean Plate, Cerpa et al. 2021), which is consistent with Mode NE. The phenomenon that many BABs were formed by splitting a volcanic arc apart (Mariana Trough, Lau Basin, East Scotia Basin, etc; Karig 1970; Dalziel and Elliot 1971; Sclater et al. 1972; Gill 1976; Karig et al. 1978; Ballance et al. 1999; Zellmer

and Taylor 2001; Oakley et al. 2009) is reproduced by Mode EH. However, very few or even no BAB is definitely observed extending far away from the volcanic arc (like the Mode EF process). Speculating from the limited available information, the Japan Sea possibly formed far away behind the Japan Arc (Tatsumi et al., 1990) and might be an EF example. It is observed that the Japan Arc is approximately 300 km away from the Japan Trench (Jarrard, 1986), and the distance from the spreading centre of the Japan Sea to the trench is around 700 km (Tamaki, 1992), which is close to the mantle flow size in my models (750 km). Admittedly, there are opinions claiming that the Japan Sea opened at a proto-Japan Arc (Jolivet et al., 1994), but the evidence presented is debatable due to the lack of a remnant ridge on the western side of the Japan Sea.

As discussed in Section 3.6, an old SP facilitates back-arc extension in my models, and the trend meets observations in nature. Introducing a hot region enhances the initial OP ages which makes an extension happen. However, my models show Mode EF when the SP age is quite old because of the strong mantle flow it induces, whereas most of the BABs along the western Pacific formed in the process of Mode EH. To generate an EH, these models require an SP aged less than about 100 Ma and a young OP, or a hot region with a large size and high temperature when the SP is relatively old. In view of the ages of the western Pacific SPs (over 100 Ma), it is assumed that the arcs in nature would be hotter than those in my models. Unfortunately, the uncertainty in the effects of actual arcs on back-arc extensions makes it difficult to compare these models directly with observations.

Besides, the survival time of the extensions in my models is consistent with that in nature. Real back-arc basins are not active for a long time, mostly a single extension duration, without regard to the follow-up episodic ones, lasts less than 20 Myrs (Luyendyk et al., 1973; Tamaki, 1995; Fujioka et al., 1999; Jolivet and Faccenna, 2000; Eagles et al., 2005; Eagles, 2010; Barckhausen et al., 2014; Doo et al., 2015). For exam-

ple, ^{40}Ar–^{39}Ar dating indicated that the basement of the Japan Basin was aged 24–17 Ma, which means the crust grew for 7 Myrs (Kaneoka, 1992). The ages of the present-day BABs are usually less than 10 Myrs (Madsen and Lindley, 1994; Caratori Tontini et al., 2019), like the Mariana Trough started 5 Myrs ago (Yamazaki et al., 2003), the Okinawa Trough is only 2 Ma (Kimura, 1985; Sibuet et al., 1998), and the Lau Basin has been active for less than 6 Myrs (Weissel, 1977; Taylor et al., 1996; Ruellan et al., 2003). The models of both EF and EH show that the Extension stops extending within 4–15 Myrs (older SP keeps the Extension longer), which is consistent with some cases in nature (e.g. the Sulu Sea lasted for about 4 Myrs and Vavilov Basin lasted for 3–4 Myrs; Schliffke et al., 2022).

It is worth noting that the temperature in the hot zone is not maintained after the model starts, so it gives an upper bound on the strength of the OP, which means that it might be simpler to form an extension in reality because the arc might keep being heated. Another possibility on Earth is that the arc becomes active again after the back-arc stops being active. I did not renew an arc after the Extension, so there is no episodic back-arc extension in these models.

I must also acknowledge that the properties that a given arc would present to an OP, in simulations like mine, are currently poorly defined. This further complicates, for now, a detailed comparison between models and nature.

5.5 Conclusion

These models show that a volcanic arc significantly impacts the back-arc extension on the OP in a subduction system even though extension can also happen without the arc.

1. By means of introducing a hot region on the OP and testing various parameters,

three end-member types of back-arc extension are depicted: (a) No back-arc Extension on the OP (Mode NE); (b) back-arc Extension occurs at the far-field location (about 750 km from the trench, Mode EF); and (c) back-arc Extension at the Hot region (Mode EH), including models with slab Detachment (EH-D). NE and EH modes are common in nature, whereas EF mode is very rare. I speculate that the Japan Sea might be a case of EF mode.

2. Properties of the hot region influence the modes. A farther distance from the hot region centre to the trench (Distance), a larger width of the hot region (Width), and a higher increased temperature of the hot region centre (ΔT) encourage back-arc extension on the OP, as well as the modes transfer from (a) Mode NE, to (b) Mode EF, to (c) Mode EH.

3. Plate ages are important parameters influencing the mode changes as well. When the OP is homogeneous, an old SP or a young OP in a model encourages back-arc extension about 750 km from the trench on the OP (almost the same location as that in Mode EF). After introducing the hot region, I note that not only is back-arc extension more likely to happen, but the Extension switches from its far-field location into the hot region itself in some modes with a relatively young SP (Age^0_{SP} less than 100 Ma in these models, but this threshold age would change if the hot region varies).

4. The poloidal flow underneath the OP is confirmed as a primary driving force, and the mechanism is understood better. The flow cell has almost the same size in every model, which focuses at around 750 km from the trench on the OP. The introduction of a hot region weakens the OP and enhances a higher trench retreat rate which facilitates the poloidal flow, thus encouraging back-arc extension.

Chapter 6

Conclusion

6.1 Summary and conclusions

Running a series of 2D thermo-mechanical models using the code Fluidity, a computational modelling framework suitable for geodynamic models, this thesis has investigated the coupling strength at the subduction interface (Chapter 3), rheology parameters (Chapter 4), a hot region on the overriding plate (OP) (Chapter 5) and plate ages (in all these chapters) in generating different modes of plate behaviours, especially extension on the OP.

Chapter 3 provides foundational models for this dissertation, presenting a reference model (as illustrated in Figure 3.2) and a reference regime diagram (Figure 3.6) that explore the initial ages of the plates at the trench (Age^0_{SP} and Age^0_{OP}). These models serve as benchmarks for comparative analyses in Chapters 4 and 5. The regime diagram delineates a threshold between plate age combinations that result in either Extension or No Extension modes of the OP, noting that the Age^0_{OP} is typically younger than those observed in actual geological settings. This discrepancy is potentially attributable to the assumption of a uniformly rigid OP, prompting the introduction of a thermally

weakened region in Chapter 5 to address this rigidity. Additionally, the study examines the variability of coupling strength at the plate interface by adjusting the friction coefficient of the weak layer above the subducting plate (SP), simulating the lubrication effect that facilitates subduction. Through this investigation, a friction coefficient value is selected that yields commonly observed SP behaviour and OP thinning without inducing extension.

Chapter 4 discusses how variations in the parameters of deformation mechanisms impact the deformation of overriding and subducting plates. Three distinct behaviours for the OP are identified: back-arc Extension (BE), Fore-arc Extension (FE), and No Extension (NE). The SP morphologies, including Inclining (I), Folding (F), and Detachment (D), influence OP deformation. SP folding inhibits the Extension on the OP, and SP detachment helps the Extension stop and heal. The study finds that SP inclining is associated with high composite viscosity, while detachment occurs with reduced viscosity in specific deformation mechanisms (dislocation and Pierels creeps, yielding deformation), and SP folding, associated with rapid sinking and steep dip angles, appears to be influenced by variations in diffusion creep parameters. This study underscores the critical role of precise rheological parameterisation in modelling tectonic behaviours, small adjustments in parameters significantly impact the results. Comparisons between model predictions and geological observations offer a method to constrain rheological parameters to some extent, for instance, the SP detachment in ocean-ocean subduction is rarely represented in models and observed reality, suggesting that some parameter combinations may not occur naturally.

In Chapter 5 I introduce a hot region into the OP, mimicking a volcanic arc, to respond to the limitation of a homogeneous OP in the previous chapters. By testing three properties (the distance between the hot region and the trench, the width of the hot region and the increasing temperature at the centre) of the hot region, three end-

member types of back-arc extension have been identified: (1) No back-arc Extension on the OP (Mode NE); (2) back-arc Extension at a far-field location, approximately 750 km from the trench (Mode EF); and (3) back-arc Extension at the Hot region (Mode EH), including scenarios with slab Detachment (EH-D). Then the initial plate ages are also tested in models with a fixed hot region. Properties of the hot region and plate ages are both important parameters influencing the modes. They help understand the driving mechanism of back-arc extension and the role of an arc in this system. An arc encourages an extension and also influences the location of an extension. Comparing the results with reality, my models suggest that the EH mode is common, while the EF mode is rare. I note that on the Earth presently there are many EH-like cases (e.g. Mariana Trough and Lau Basin), while EF cases are rarer (potentially Japan Sea). This phenomenon is consistent with the initial plate ages on Earth and gives a clue to the properties of an arc.

Overall, Extension within the OP predominantly manifests under conditions where the SP is older, or the OP is younger, or where the coupling strength at the plate interface is reduced. This extension is also favoured by lower viscosities across most mechanisms, with the notable exception of diffusion creep viscosity, and is further facilitated when a region of relative weakness, characterised by elevated temperatures, is present within the OP.

In conclusion, this study shows that the poloidal flow induced by the subduction (enhanced by the trench retreat) is the main driving mechanism of back-arc extension in the 2D models, and Extension starts from the base of an OP. In detail, the vertically upwelling component of the flow helps weaken the OP from the base, and the trench-ward horizontal component provides the extensional force at the OP base. The mantle flow cell has almost the same size in every model, which focuses on the OP at around 750 km from the trench, but a preexisting thermally weakened zone can change the

mantle flow cell before it grows, and therefore extension does not occur at the far-field location (750 km from the trench). The preexisting thermally weakened zone can include such a zone at the mantle wedge corner near the trench caused by a low dislocation creep viscosity (Chapter 4) or a hot zone which is set initially on the OP (Chapter 5). It can be seen that thermal weakening dominates in the extension process.

6.2 Limitations and Further work

6.2.1 Limitations

1. 2D modeling. (1) 2D models lack the lateral dimension of the real 3D world, which means the toroidal component of the mantle flow is ignored. There is some research suggesting that toroidal flow makes an important contribution to back-arc extension on the OP (Clio and Pieter, 2013; Chen et al., 2016), especially at narrow subduction zones (Schellart and Moresi, 2013). My 2D models imply that the width of plates is infinitely wide and everywhere is the same along the third dimension. Thus, the models may not be applicable to the narrow subduction system, such as Gibraltar and the Calabria subduction zones. (2) I am implicitly assuming that the arcs are linear and constant along strike, while in reality the arc volcanoes focus along strike. (3) The plates can be inhomogeneous perpendicular to strike, a direction which is modelled, but only with simply varying plates to allow comparison, or along strike, a direction that is not modelled.

2. Simplification of the models. (1) I did not run models with a real continental OP, even though the Japan Sea, a case with a continental OP, is discussed in this thesis. Because the models are simplified to include only mantle (more viscous than crust at the same temperature) viscosity, the OP lithosphere is stronger than it should be at a given age (the thermal structure depends on the initial age of plates). Using

a younger age reduces the OP thickness and decreases the total strength to partly counteract the lack of crust. As a result, the same phenomenon requires a real plate to be older than that in my models (and even older age for a continental plate compared to an oceanic plate). Since the extension initiates at the base of the plate, maybe the lack of the crust is quantitatively unimportant. (2) I kept the structure of the OP simple and similar to allow comparison across models, but the actual history might be complex and important in actual cases. (3) I have used a simple far-field boundary condition on the OP of a ridge, different boundary conditions might better represent actual settings. I have kept the models simple in this case to allow comparison. (4) The process of forming an arc is part of the subduction process, therefore, there is a possibility for important feedback between the arc and subduction that I cannot capture in these models. (5) I am here using such old SP ages of a half-space cooling model to investigate a greater negative thermal buoyancy (this could reflect densification processes, eg. eclogitisation). Assuming a plate model rather than a half-space cooling model would lead to no difference in slab buoyancy at such old ages. Therefore one should be careful in not to make simple comparisons with such old oceanic plate ages.

6.2.2 Future work

Based on some of the limitations I mentioned above, some future work can be done to better understand the geodynamics in a subduction zone, especially the driving mechanism of back-arc extension.

(1) Because of the limitation of 2D models, some 3D work should be done to check the proportion of poloidal versus toroidal flow that drives back-arc extension. Also, some lateral properties can be tested in 3D models, such as the width of the slab and individual volcanic centres of arcs. (2) It is worth investigating whether adding a continental crust to the OP makes a significant difference in geodynamics. (3) The

righthand side edge of the OP can be fixed in future models. The OPs of all models in this thesis are mobile so that the trench retreats at quite high rates, which enhances the mantle flow. However, the OPs in reality might not move as freely as these models. Thus, it is worth testing a fixed OP as an end-member case.

References

Bibliography

Arcay, D., Lallemand, S., and Doin, M. P.: Back-arc strain in subduction zones: Statistical observations versus numerical modeling, Geochemistry, Geophysics, Geosystems, 9, 2008.

Artemieva, I. M.: Back-arc basins: A global view from geophysical synthesis and analysis, Earth-Science Reviews, 236, 104 242, 2023.

Auzende, J. M., Rissen, J. P., Lafoy, Y., Gente, P., and Charlou, J. L.: Seafloor spreading in the north Fiji basin (Southwest Pacific), Tectonophysics, 146, 317–352, 1988.

Auzende, J. M., Pelletier, B., and Eissen, J. P.: The North Fiji Basin geology, structure, and geodynamic evolution, in: Backarc basins: Tectonics and magmatism, pp. 139–175, Springer, 1995.

Baitsch-Ghirardello, B., Gerya, T., and Burg, J. P.: Geodynamic regimes of intra-oceanic subduction: Implications for arc extension vs. shortening processes, Gondwana Research, 25, 546–560, 2014.

Balázs, A., Faccenna, C., Ueda, K., Funiciello, F., Boutoux, A., Blanc, E. J. P., and

Gerya, T.: Oblique subduction and mantle flow control on upper plate deformation: 3D geodynamic modeling, Earth and Planetary Science Letters, 569, 117 056, 2021.

Balázs, A., Faccenna, C., Gerya, T., Ueda, K., and Funiciello, F.: The dynamics of forearc–back-arc basin subsidence: Numerical models and observations from Mediterranean subduction zones, Tectonics, 41, e2021TC007 078, 2022.

Ballance, P. F., Ablaev, A. G., Pushchin, I. K., Pletnev, S. P., Birylina, M. G., Itaya, T., Follas, H. A., and Gibson, G. W.: Morphology and history of the Kermadec trench–arc–backarc basin–remnant arc system at 30 to 32 S: Geophysical profile, microfossil and K–Ar data, Marine Geology, 159, 35–62, 1999.

Barckhausen, U., Engels, M., Franke, D., Ladage, S., and Pubellier, M.: Evolution of the South China Sea: Revised ages for breakup and seafloor spreading, Marine and Petroleum Geology, 58, 599–611, 2014.

Barker, P. F.: A spreading centre in the east Scotia Sea, Earth and Planetary Science Letters, 15, 123–132, 1972.

Barker, P. F.: Tectonic framework of the east Scotia Sea, Backarc Basins: Tectonics and Magmatism, pp. 281–314, 1995.

Barker, P. F. and Hill, I. A.: Back-arc extension in the Scotia Sea, Philosophical Transactions of the Royal Society of London. Series A, Mathematical and Physical Sciences, 300, 249–262, 1981.

Baumgardner, J. R.: Three-dimensional treatment of convective flow in the Earth's mantle, Journal of Statistical Physics, 39, 501–511, 1985.

Behr, W. M., Holt, A. F., Becker, T. W., and Faccenna, C.: The effects of plate

interface rheology on subduction kinematics and dynamics, Geophysical Journal International, 230, 796–812, 2022.

Bibee, L. D., Shor Jr, G. G., and Lu, R. S.: Inter-arc spreading in the Mariana Trough, Marine Geology, 35, 183–197, 1980.

Biju-Duval, B., Letouzey, J., Montadert, L., et al.: 50. Structure and evolution of the Mediterranean basins, Deep Sea Drilling Project Initial Reports, 142, 951–984, 1978.

Buffett, B. and Heuret, A.: Curvature of subducted lithosphere from earthquake locations in the Wadati-Benioff zone, Geochemistry, Geophysics, Geosystems, 12, 2011.

Burov, E. B.: Rheology and strength of the lithosphere, Marine and petroleum Geology, 28, 1402–1443, 2011.

Butterworth, N. P., Quevedo, L., Morra, G., and Müller, R. D.: Influence of overriding plate geometry and rheology on subduction, Geochemistry, Geophysics, Geosystems, 13, 2012.

Byerlee, J.: Friction of rocks, Rock friction and earthquake prediction, pp. 615–626, 1978.

Capitanio, F. A. and Replumaz, A.: Subduction and slab breakoff controls on Asian indentation tectonics and Himalayan western syntaxis formation, Geochemistry, Geophysics, Geosystems, 14, 3515–3531, 2013.

Capitanio, F. A., Morra, G., and Goes, S.: Dynamic models of downgoing plate-buoyancy driven subduction: Subduction motions and energy dissipation, Earth and Planetary Science Letters, 262, 284–297, 2007.

Capitanio, F. A., Stegman, D. R., Moresi, L. N., and Sharples, W.: Upper plate controls on deep subduction, trench migrations and deformations at convergent margins, Tectonophysics, 483, 80–92, 2010.

Capitanio, F. A., Faccenna, C., Zlotnik, S., and Stegman, D. R.: Subduction dynamics and the origin of Andean orogeny and the Bolivian orocline, Nature, 480, 83–86, 2011.

Caratori Tontini, F., Bassett, D., de Ronde, C. E., Timm, C., and Wysoczanski, R.: Early evolution of a young back-arc basin in the Havre Trough, Nature Geoscience, 12, 856–862, 2019.

Carlson, R. L. and Mortera-Gutiérrez, C. A.: Subduction hinge migration along the Izu-Bonin-Mariana arc, Tectonophysics, 181, 331–344, 1990.

Cerpa, N. G., Hassani, R., Arcay, D., Lallemand, S., Garrocq, C., Philippon, M., Cornée, J.-J., Münch, P., Garel, F., Marcaillou, B., et al.: Caribbean Plate Boundaries Control on the Tectonic Duality in the Back-Arc of the Lesser Antilles Subduction Zone During the Eocene, Tectonics, 40, e2021TC006 885, 2021.

Chen, Z., Schellart, W. P., and Duarte, J. C.: Quantifying the energy dissipation of overriding plate deformation in three-dimensional subduction models, Journal of Geophysical Research: Solid Earth, 120, 519–536, 2015.

Chen, Z., Schellart, W. P., Strak, V., and Duarte, J. C.: Does subduction-induced mantle flow drive backarc extension?, Earth and Planetary Science Letters, 441, 200–210, 2016.

Chopra, P. N. and Paterson, M. S.: The experimental deformation of dunite, Tectonophysics, 78, 453–473, 1981.

Chopra, P. N. and Paterson, M. S.: The role of water in the deformation of dunite, Journal of Geophysical Research: Solid Earth, 89, 7861–7876, 1984.

Čížková, H. and Bina, C. R.: Effects of mantle and subduction-interface rheologies on slab stagnation and trench rollback, Earth and Planetary Science Letters, 379, 95–103, 2013.

Clark, S. R., Stegman, D., and Müller, R. D.: Episodicity in back-arc tectonic regimes, Physics of the Earth and Planetary Interiors, 171, 265–279, 2008.

Clio, M. and Pieter, S. W.: Three-dimensional dynamic models of subducting plate-overriding plate-upper mantle interaction, Journal of Geophysical Research: Solid Earth, 118, 775–790, 2013.

Conrad, C. P. and Lithgow-Bertelloni, C.: How mantle slabs drive plate tectonics, Science, 298, 207–209, 2002.

Corradino, M., Balázs, A., Faccenna, C., and Pepe, F.: Arc and forearc rifting in the Tyrrhenian subduction system, Scientific Reports, 12, 4728, 2022.

Crameri, F., Tackley, P., Meilick, I., Gerya, T., and Kaus, B.: A free plate surface and weak oceanic crust produce single-sided subduction on Earth, Geophysical Research Letters, 39, 2012.

Crawford, A. J., Beccaluva, L., and Serri, G.: Tectono-magmatic evolution of the West Philippine-Mariana region and the origin of boninites, Earth and Planetary Science Letters, 54, 346–356, 1981.

Cross, T. A. and Pilger, R. H.: Controls of subduction geometry, location of magmatic arcs, and tectonics of arc and back-arc regions, Geological Society of America Bulletin, 93, 545–562, 1982.

Dal Zilio, L., Faccenda, M., and Capitanio, F.: The role of deep subduction in supercontinent breakup, Tectonophysics, 746, 312–324, 2018.

Dalziel, I. W. and Elliot, D. H.: Evolution of the Scotia arc, Nature, 233, 246–252, 1971.

Dasgupta, R., Mandal, N., and Lee, C.: Controls of subducting slab dip and age on the extensional versus compressional deformation in the overriding plate, Tectonophysics, 801, 228 716, 2021.

Davies, D. R., Wilson, C. R., and Kramer, S. C.: Fluidity: A fully unstructured anisotropic adaptive mesh computational modeling framework for geodynamics, Geochemistry, Geophysics, Geosystems, 12, 2011.

Davies, J. H. and von Blanckenburg, F.: Slab breakoff: a model of lithosphere detachment and its test in the magmatism and deformation of collisional orogens, Earth and planetary science letters, 129, 85–102, 1995.

Deschamps, A. and Lallemand, S.: The West Philippine Basin: An Eocene to early Oligocene back arc basin opened between two opposed subduction zones, Journal of Geophysical Research: Solid Earth, 107, EPM–1, 2002.

Di Giuseppe, E., Van Hunen, J., Funiciello, F., Faccenna, C., and Giardini, D.: Slab stiffness control of trench motion: Insights from numerical models, Geochemistry, Geophysics, Geosystems, 9, 2008.

Di Giuseppe, E., Faccenna, C., Funiciello, F., van Hunen, J., and Giardini, D.: On the relation between trench migration, seafloor age, and the strength of the subducting lithosphere, Lithosphere, 1, 121–128, 2009.

Doo, W. B., Hsu, S. K., Yeh, Y. C., Tsai, C. H., and Chang, C. M.: Age and tectonic evolution of the northwest corner of the West Philippine Basin, Marine Geophysical Research, 36, 113–125, 2015.

Dvorkin, J., Nur, A., Mavko, G., and Ben-Avraham, Z.: Narrow subducting slabs and the origin of backarc basins, Tectonophysics, 227, 63–79, 1993.

Eagles, G.: The age and origin of the central Scotia Sea, Geophysical Journal International, 183, 587–600, 2010.

Eagles, G., Livermore, R. A., Fairhead, J. D., and Morris, P.: Tectonic evolution of the West Scotia Sea, Journal of Geophysical Research: Solid Earth, 110, 2005.

Faccenna, C., Mattei, M., Funiciello, R., and Jolivet, L.: Styles of back-arc extension in the central Mediterranean, Terra Nova, 9, 126–130, 1997.

Faccenna, C., Funiciello, F., Giardini, D., and Lucente, P.: Episodic back-arc extension during restricted mantle convection in the Central Mediterranean, Earth and Planetary Science Letters, 187, 105–116, 2001.

Faccenna, C., Di Giuseppe, E., Funiciello, F., Lallemand, S., and van Hunen, J.: Control of seafloor aging on the migration of the Izu–Bonin–Mariana trench, Earth and Planetary Science Letters, 288, 386–398, 2009.

Fadaie, K. and Ranalli, G.: Rheology of the lithosphere in the East African Rift System, Geophysical Journal International, 102, 445–453, 1990.

Fowler, C. M. R., Fowler, C. M. R., and Fowler, M.: The solid earth: an introduction to global geophysics, Cambridge University Press, 1990.

Fujioka, K., Okino, K., Kanamatsu, T., Ohara, Y., Ishizuka, O., Haraguchi, S., and Ishii, T.: Enigmatic extinct spreading center in the West Philippine backarc basin unveiled, Geology, 27, 1135–1138, 1999.

Gable, C. W., O'Connell, R. J., and Travis, B. J.: Convection in three dimensions with surface plates: Generation of toroidal flow, Journal of Geophysical Research: Solid Earth, 96, 8391–8405, 1991.

Garel, F., Goes, S., Davies, D. R., Davies, J. H., Kramer, S. C., and Wilson, C. R.: Interaction of subducted slabs with the mantle transition-zone: A regime diagram from 2-D thermo-mechanical models with a mobile trench and an overriding plate, Geochemistry, Geophysics, Geosystems, 15, 1739–1765, 2014.

Gerya, T.: Future directions in subduction modeling, Journal of Geodynamics, 52, 344–378, 2011.

Gill, J. B.: Composition and age of Lau Basin and Ridge volcanic rocks: implications for evolution of an interarc basin and remnant arc, Geological Society of America Bulletin, 87, 1384–1395, 1976.

Guillaume, B., Funiciello, F., and Faccenna, C.: Interplays between mantle flow and slab pull at subduction zones in 3D, Journal of Geophysical Research: Solid Earth, 126, e2020JB021 574, 2021.

Gutscher, M.-A., Spakman, W., Bijwaard, H., and Engdahl, E. R.: Geodynamics of flat subduction: Seismicity and tomographic constraints from the Andean margin, Tectonics, 19, 814–833, 2000.

Hawkins, J. W., Lonsdale, P. F., Macdougall, J. D., and Volpe, A. M.: Petrology of the axial ridge of the Mariana Trough backarc spreading center, Earth and Planetary Science Letters, 100, 226–250, 1990.

Herzer, R. H., Barker, D. H. N., Roest, W. R., and Mortimer, N.: Oligocene-Miocene spreading history of the northern South Fiji Basin and implications for the evolution of the New Zealand plate boundary, Geochemistry, Geophysics, Geosystems, 12, 2011.

Heuret, A. and Lallemand, S.: Plate motions, slab dynamics and back-arc deformation, Physics of the Earth and Planetary Interiors, 149, 31–51, 2005.

Hirth, G. and Kohlstedt, D.: Rheology of the upper mantle and the mantle wedge: A view from the experimentalists, Geophysical monograph-american geophysical union, 138, 83–106, 2003.

Hirth, G. and Kohlstedt, D. L.: Water in the oceanic upper mantle: implications for rheology, melt extraction and the evolution of the lithosphere, Earth and Planetary Science Letters, 144, 93–108, 1996.

Holt, A. F., Becker, T. W., and Buffett, B. A.: Trench migration and overriding plate stress in dynamic subduction models, Geophysical Journal International, 201, 172–192, 2015.

Hussong, D. M.: Tectonic processes and the history of the Mariana Arc: a synthesis of the results of Deep Sea Drilling Project Leg 60, Initial reports of the deep sea drilling project, 60, 909–929, 1981.

Ikeda, Y., Stern, R. J., Kagami, H., and Sun, C. H.: Pb, Nd, and Sr isotopic constraints on the origin of Miocene basaltic rocks from northeast Hokkaido, Japan: Implications for opening of the Kurile back-arc basin, Island Arc, 9, 161–172, 2000.

Jadamec, M. A.: Insights on slab-driven mantle flow from advances in three-dimensional modelling, Journal of Geodynamics, 100, 51–70, 2016.

Jadamec, M. A. and Billen, M. I.: Reconciling surface plate motions with rapid three-dimensional mantle flow around a slab edge, Nature, 465, 338–341, 2010.

Jain, C., Korenaga, J., and Karato, S. I.: Global analysis of experimental data on the rheology of olivine aggregates, Journal of Geophysical Research: Solid Earth, 124, 310–334, 2019.

Jarrard, R. D.: Relations among subduction parameters, Reviews of Geophysics, 24, 217–284, 1986.

Jodie, P.: Calculating arc-trench distances using the Smithsonian Global Volcanism Project database, URL https://www.earthbyte.org/calculating-arc-trench-distances-using-the-smithsonian-global-volcanism-project-database/, accessed April 27, 2023, 2016.

Jolivet, L. and Faccenna, C.: Mediterranean extension and the Africa-Eurasia collision, Tectonics, 19, 1095–1106, 2000.

Jolivet, L., Tamaki, K., and Fournier, M.: Japan Sea, opening history and mechanism: A synthesis, Journal of Geophysical Research: Solid Earth, 99, 22 237–22 259, 1994.

Kaneoka, I.: ^{40}Ar-^{39}Ar analysis of volcanic rocks recovered from the Japan Sea Floor: Constraints on the age of formation of the Japan Sea, Proceedings of the Ocean Drilling Program, Scientific Results, 1992, 127, 819–836, 1992.

Karato, S. I.: Effects of pressure on plastic deformation of polycrystalline solids: some geological applications, MRS Online Proceedings Library (OPL), 499, 3, 1997.

Karato, S. I. and Wu, P.: Rheology of the upper mantle: A synthesis, Science, 260, 771–778, 1993.

Karato, S. I., Paterson, M. S., and FitzGerald, J. D.: Rheology of synthetic olivine aggregates: Influence of grain size and water, Journal of Geophysical Research: Solid Earth, 91, 8151–8176, 1986.

Karato, S.-i., Riedel, M. R., and Yuen, D. A.: Rheological structure and deformation of subducted slabs in the mantle transition zone: implications for mantle circulation and deep earthquakes, Physics of the Earth and Planetary Interiors, 127, 83–108, 2001.

Karig, D. E.: Ridges and basins of the Tonga-Kermadec island arc system, Journal of geophysical research, 75, 239–254, 1970.

Karig, D. E.: Origin and development of marginal basins in the western Pacific, Journal of geophysical research, 76, 2542–2561, 1971.

Karig, D. E., Anderson, R. N., and Bibee, L. D.: Characteristics of back arc spreading in the Mariana Trough, Journal of Geophysical Research: Solid Earth, 83, 1213–1226, 1978.

Keefner, J. W., Mackwell, S. J., and Kohlstedt, D. L.: Dependence of dislocation creep of dunite on oxygen fugacity: Implications for viscosity variations in Earth's mantle, Journal of Geophysical Research: Solid Earth, 116, 2011.

Kimura, M.: Back-arc rifting in the Okinawa Trough, Marine and Petroleum Geology, 2, 222–240, 1985.

Király, Á., Capitanio, F. A., Funiciello, F., and Faccenna, C.: Subduction induced mantle flow: Length-scales and orientation of the toroidal cell, Earth and Planetary Science Letters, 479, 284–297, 2017.

Korenaga, J.: Plate tectonics and surface environment: Role of the oceanic upper mantle, Earth-Science Reviews, 205, 103 185, 2020.

Kramer, S. C., Wilson, C. R., and Davies, D. R.: An implicit free surface algorithm for geodynamical simulations, Physics of the Earth and Planetary Interiors, 194, 25–37, 2012.

Lallemand, S., Heuret, A., and Boutelier, D.: On the relationships between slab dip, back-arc stress, upper plate absolute motion, and crustal nature in subduction zones, Geochemistry, Geophysics, Geosystems, 6, 2005.

Le Pichon, X. and Angelier, J.: The Hellenic Arc and trench system: a key to the neotectonic evolution of the eastern Mediterranean area, Tectonophysics, 60, 1–42, 1979.

Lee, S. M. and Ruellan, E.: Tectonic and magmatic evolution of the Bismarck Sea, Papua New Guinea: review and new synthesis, Washington DC American Geophysical Union Geophysical Monograph Series, 166, 263–286, 2006.

Lei, Z.: Numerical investigation of the influence of subduction on deformation within the overriding plate, Ph.D. thesis, Cardiff University, 2022.

Li, Z., Xu, Z., Gerya, T., and Burg, J. P.: Collision of continental corner from 3-D numerical modeling, Earth and Planetary Science Letters, 380, 98–111, 2013.

Luyendyk, B. P., MacDonald, K. C., and Bryan, W. B.: Rifting history of the Woodlark Basin in the southwest Pacific, Geological Society of America Bulletin, 84, 1125–1134, 1973.

Madsen, J. A. and Lindley, I. D.: Large-scale structures on Gazelle Peninsula, New

Britain: Implications for the evolution of the New Britain arc, Australian Journal of Earth Sciences, 41, 561–569, 1994.

Magni, V., Faccenna, C., van Hunen, J., and Funiciello, F.: How collision triggers backarc extension: Insight into Mediterranean style of extension from 3-D numerical models, Geology, 42, 511–514, 2014.

Malinverno, A. and Ryan, W. B. F.: Extension in the Tyrrhenian Sea and shortening in the Apennines as result of arc migration driven by sinking of the lithosphere, Tectonics, 5, 227–245, 1986.

Manga, M., Hornbach, M. J., Le Friant, A., Ishizuka, O., Stroncik, N., Adachi, T., Aljahdali, M., Boudon, G., Breitkreuz, C., Fraass, A., et al.: Heat flow in the Lesser Antilles island arc and adjacent back arc Grenada basin, Geochemistry, Geophysics, Geosystems, 13, 2012.

Mantovani, E., Albarello, D., Tamburelli, C., and Babbucci, D.: Evolution of the Tyrrhenian basin and surrounding regions as a result of the Africa-Eurasia convergence, Journal of Geodynamics, 21, 35–72, 1996.

Mantovani, E., Albarello, D., Tamburelli, C., Babbucci, D., Viti, M., et al.: Plate convergence, crustal delamination, extrusion tectonics and minimization of shortening work as main controlling factors of the recent Mediterranean deformation pattern, Annals of Geophysics, 40, 611–643, 1997.

Mantovani, E., Albarello, D., Babbucci, D., Tamburelli, C., Viti, M., Boschi, E., Ekstrom, G., and Morelli, A.: Genetic mechanism of back-arc opening: insights from the Mediterranean deformation pattern, Problems in Geophysics for the new millennium, Editrice Compositori, Bologna, pp. 611–643, 2000.

Mantovani, E., Viti, M., Babbucci, D., Tamburelli, C., and Albarello, D.: Back arc extension: which driving mechanism, J. Virtual Explorer, 3, 17–45, 2001.

Mantovani, E., Viti, M., Albarello, D., Babbucci, D., Tamburelli, C., and Cenni, N.: Generation of backarc basins in the Mediterranean region: driving mechanisms and quantitative modelling, Bollettino della Società geologica italiana, 121, 99–111, 2002.

Martinez, F. and Taylor, B.: Mantle wedge control on back-arc crustal accretion, Nature, 416, 417–420, 2002.

Martinez, F. and Taylor, B.: Controls on back-arc crustal accretion: insights from the Lau, Manus and Mariana basins, Geological Society, London, Special Publications, 219, 19–54, 2003.

Martínez, F., Fryer, P., Baker, N. A., and Yamazaki, T.: Evolution of backarc rifting: Mariana Trough, 20–24 N, Journal of Geophysical Research: Solid Earth, 100, 3807–3827, 1995.

McKenzie, D. P., Roberts, J. M., and Weiss, N. O.: Convection in the Earth's mantle: towards a numerical simulation, Journal of Fluid Mechanics, 62, 465–538, 1974.

Mei, S. and Kohlstedt, D. L.: Influence of water on plastic deformation of olivine aggregates: 2. Dislocation creep regime, Journal of Geophysical Research: Solid Earth, 105, 21 471–21 481, 2000.

Mei, S., Suzuki, A. M., Kohlstedt, D. L., and Xu, L.: Experimental investigation of the creep behavior of garnet at high temperatures and pressures, Journal of Earth Science, 21, 532–540, 2010.

Minear, J. W. and Toksöz, M. N.: Thermal regime of a downgoing slab and new global tectonics, Journal of Geophysical Research, 75, 1397–1419, 1970.

Mortimer, N., Herzer, R. H., Gans, P. B., Parkinson, D. L., and Seward, D.: Basement geology from Three Kings Ridge to West Norfolk Ridge, southwest Pacific Ocean: evidence from petrology, geochemistry and isotopic dating of dredge samples, Marine Geology, 148, 135–162, 1998.

Müller, R. D., Sdrolias, M., Gaina, C., and Roest, W. R.: Age, spreading rates, and spreading asymmetry of the world's ocean crust, Geochemistry, Geophysics, Geosystems, 9, 2008.

Nakagawa, T. and Karato, S. I.: Influence of realistic rheological properties on the style of mantle convection: roles of dynamic friction and depth-dependence of rheological properties, Geophysical Journal International, 226, 1986–1996, 2021.

Nakakuki, T. and Mura, E.: Dynamics of slab rollback and induced back-arc basin formation, Earth and Planetary Science Letters, 361, 287–297, 2013.

Oakley, A. J., Taylor, B., Moore, G. F., and Goodliffe, A.: Sedimentary, volcanic, and tectonic processes of the central Mariana Arc: Mariana Trough back-arc basin formation and the West Mariana Ridge, Geochemistry, Geophysics, Geosystems, 10, 2009.

Parson, L. M. and Wright, I. C.: The Lau-Havre-Taupo back-arc basin: A southward-propagating, multi-stage evolution from rifting to spreading, Tectonophysics, 263, 1–22, 1996.

Pe-piper, G. and Piper, D. J. W.: Spatial and temporal variation in Late Cenozoic back-arc volcanic rocks, Aegean Sea region, Tectonophysics, 169, 113–134, 1989.

Platt, J. P., Whitehouse, M. J., Kelley, S. P., Carter, A., and Hollick, L.: Simultaneous extensional exhumation across the Alboran Basin: implications for the causes of late orogenic extension, Geology, 31, 251–254, 2003.

Ranalli, G. and Fischer, B.: Diffusion creep, dislocation creep, and mantle rheology, Physics of the earth and planetary interiors, 34, 77–84, 1984.

Ribe, N.: Bending and stretching of thin viscous sheets, Journal of Fluid Mechanics, 433, 135–160, 2001.

Ribe, N. M.: Bending mechanics and mode selection in free subduction: A thin-sheet analysis, Geophysical Journal International, 180, 559–576, 2010.

Rogers, G. C.: An assessment of the megathrust earthquake potential of the Cascadia subduction zone, Canadian Journal of Earth Sciences, 25, 844–852, 1988.

Rosenbaum, G. and Lister, G. S.: Formation of arcuate orogenic belts in the western Mediterranean region, Orogenic curvature: integrating paleomagnetic and structural analyses, 383, 41–56, 2004.

Royden, L.: The tectonic expression of slab pull at continental convergent boundaries, Tectonics, 12, 3, 1993.

Ruellan, E., Delteil, J., Wright, I., and Matsumoto, T.: From rifting to active spreading in the Lau Basin–Havre Trough backarc system (SW Pacific): Locking/unlocking induced by seamount chain subduction, Geochemistry, Geophysics, Geosystems, 4, 2003.

Schellart, W. P.: Subduction zones: A short review, Dynamics of Plate Tectonics and Mantle Convection, pp. 321–355, 2023.

Schellart, W. P. and Moresi, L.: A new driving mechanism for backarc extension and backarc shortening through slab sinking induced toroidal and poloidal mantle flow: Results from dynamic subduction models with an overriding plate, Journal of Geophysical Research: Solid Earth, 118, 3221–3248, 2013.

Schellart, W. P. and Spakman, W.: Mantle constraints on the plate tectonic evolution of the Tonga–Kermadec–Hikurangi subduction zone and the South Fiji Basin region, Australian Journal of Earth Sciences, 59, 933–952, 2012.

Schellart, W. P., Freeman, J., Stegman, D. R., Moresi, L., and May, D.: Evolution and diversity of subduction zones controlled by slab width, Nature, 446, 308–311, 2007.

Schellart, W. P., Stegman, D. R., and Freeman, J.: Global trench migration velocities and slab migration induced upper mantle volume fluxes: Constraints to find an Earth reference frame based on minimizing viscous dissipation, Earth-Science Reviews, 88, 118–144, 2008.

Schliffke, N., van Hunen, J., Allen, M. B., Magni, V., and Gueydan, F.: Episodic back-arc spreading centre jumps controlled by transform fault to overriding plate strength ratio, Nature Communications, 13, 582, 2022.

Schmeling, H., Babeyko, A., Enns, A., Faccenna, C., Funiciello, F., Gerya, T., Golabek, G., Grigull, S., Kaus, B., Morra, G., Schmalholz, S., and van Hunen, J.: A benchmark comparison of spontaneous subduction models—Towards a free surface, Physics of the Earth and Planetary Interiors, 171, 198–223, https://doi.org/https://doi.org/10.1016/j.pepi.2008.06.028, 2008.

Scholz, C. H. and Campos, J.: On the mechanism of seismic decoupling and back arc spreading at subduction zones, Journal of Geophysical Research: Solid Earth, 100, 22 103–22 115, 1995.

Sclater, J. G., Hawkins, J. W., Mammerickx, J., and Chase, C. G.: Crustal extension between the Tonga and Lau ridges: petrologic and geophysical evidence, Geological Society of America Bulletin, 83, 505–518, 1972.

Sdrolias, M. and Müller, R. D.: Controls on back-arc basin formation, Geochemistry, Geophysics, Geosystems, 7, 2006.

Sdrolias, M., Roest, W. R., and Müller, R. D.: An expression of Philippine Sea plate rotation: the Parece Vela and Shikoku basins, Tectonophysics, 394, 69–86, 2004.

She, L. J., Zhang, G. B., Jiang, G. M., Zhao, D. P., Xi, J. J., Lü, Q. T., and Shi, D. N.: Slab morphology around the Philippine Sea: new insights from P-wave mantle tomography, Journal of Geophysical Research: Solid Earth, 128, e2022JB024 757, 2023.

Sheng, J., Li, C. Z., Liao, J., Yang, Z., and Jiang, S. Y.: Dynamics of back-arc extension controlled by subducting slab retreat: Insights from 2D thermo-mechanical modelling, Geological Journal, 54, 3376–3388, 2019.

Sibuet, J. C., Deffontaines, B., Hsu, S. K., Thareau, N., Le Formal, J. P., and Liu, C. S.: Okinawa trough backarc basin: Early tectonic and magmatic evolution, Journal of Geophysical Research: Solid Earth, 103, 30 245–30 267, 1998.

Stegman, D. R., Freeman, J., Schellart, W. P., Moresi, L., and May, D.: Influence of trench width on subduction hinge retreat rates in 3-D models of slab rollback, Geochemistry, Geophysics, Geosystems, 7, 2006.

Stegman, D. R., Farrington, R., Capitanio, F. A., and Schellart, W. P.: A regime diagram for subduction styles from 3-D numerical models of free subduction, Tectonophysics, 483, 29–45, 2010.

Sternai, P., Jolivet, L., Menant, A., and Gerya, T.: Driving the upper plate surface deformation by slab rollback and mantle flow, Earth and Planetary Science Letters, 405, 110–118, 2014.

Stocker, R. L. and Ashby, M. F.: On the rheology of the upper mantle, Reviews of Geophysics, 11, 391–426, 1973.

Tamaki, K.: Tectonic synthesis and implications of Japan Sea ODP drilling, Tamaki, K., K. Suyehiro, J. Allan, M. McWilliams, et al, Proceedings of the Ocean Drilling Program, Scientific Results. Texas: College Station, 127, 2, 1992.

Tamaki, K.: Opening tectonics of the Japan Sea, in: Backarc basins: Tectonics and magmatism, pp. 407–420, Springer, 1995.

Tatsumi, Y., Maruyama, S., and Nohda, S.: Mechanism of backarc opening in the Japan Sea: role of asthenospheric injection, Tectonophysics, 181, 299–306, 1990.

Taylor, B.: Bismarck Sea: evolution of a back-arc basin, Geology, 7, 171–174, 1979.

Taylor, B., Zellmer, K., Martinez, F., and Goodliffe, A.: Sea-floor spreading in the Lau back-arc basin, Earth and Planetary Science Letters, 144, 35–40, 1996.

Tielke, J. A., Zimmerman, M. E., and Kohlstedt, D. L.: Hydrolytic weakening in olivine single crystals, Journal of Geophysical Research: Solid Earth, 122, 3465–3479, 2017.

Toksöz, M. N. and Hsui, A. T.: Numerical studies of back-arc convection and the formation of marginal basins, Tectonophysics, 50, 177–196, 1978.

van der Hilst, R.: Complex morphology of subducted lithosphere in the mantle beneath the Tonga trench, Nature, 374, 154–157, 1995.

van Hunen, J. and Allen, M. B.: Continental collision and slab break-off: A comparison of 3-D numerical models with observations, Earth and Planetary Science Letters, 302, 27–37, 2011.

van Hunen, J., van den Berg, A. P., and Vlaar, N. J.: Various mechanisms to induce present-day shallow flat subduction and implications for the younger Earth: a numerical parameter study, Physics of the Earth and Planetary Interiors, 146, 179–194, 2004.

van Hunen, J., Zhong, S., Shapiro, N. M., and Ritzwoller, M. H.: New evidence for dislocation creep from 3-D geodynamic modeling of the Pacific upper mantle structure, Earth and Planetary Science Letters, 238, 146–155, 2005.

Wallace, L. M., Ellis, S., and Mann, P.: Collisional model for rapid fore-arc block rotations, arc curvature, and episodic back-arc rifting in subduction settings, Geochemistry, Geophysics, Geosystems, 10, 2009.

Weissel, J. K.: Evolution of the Lau Basin by the growth of small plates, Island Arcs, Deep Sea Trenches and Back-Arc Basins, 1, 429–436, 1977.

Wright, I. C.: Pre-spread rifting and heterogeneous volcanism in the southern Havre Trough back-arc basin, Marine geology, 113, 179–200, 1993.

Yamazaki, T., Seama, N., Okino, K., Kitada, K., Joshima, M., Oda, H., and Naka, J.: Spreading process of the northern Mariana Trough: Rifting-spreading transition at 22 N, Geochemistry, Geophysics, Geosystems, 4, 2003.

Yan, Q. S., Shi, X. F., Yuan, L., Yan, S. S., and Liu, Z. X.: Tectono-magmatic evolution of the Philippine Sea Plate: A review, Geosystems and Geoenvironment, 1, 100 018, 2022.

Zellmer, K. E. and Taylor, B.: A three-plate kinematic model for Lau Basin opening, Geochemistry, Geophysics, Geosystems, 2, 2001.

Zhong, S. J. and Gurnis, M.: Interaction of weak faults and non-Newtonian rheology produces plate tectonics in a 3D model of mantle flow, Nature, 383, 245–247, 1996.

Zhou, D., Ru, K., and Chen, H. Z.: Kinematics of Cenozoic extension on the South China Sea continental margin and its implications for the tectonic evolution of the region, Tectonophysics, 251, 161–177, 1995.

Appendix

Table A.1: Models testing plate ages with 5 different E_{diff}

Models	E_{diff}	SP age (Ma)	OP age (Ma)	Mode
E270_SP80_OP15	270	80	15	BE-F
E270_SP80_OP20	270	80	20	NF
E270_SP80_OP25	270	80	25	NF
E270_SP80_OP30	270	80	30	NF
E270_SP90_OP15	270	90	15	BE-F
E270_SP90_OP20	270	90	20	NF
E270_SP90_OP25	270	90	25	NF
E270_SP90_OP30	270	90	30	NF
E270_SP120_OP15	270	120	15	BE
E270_SP120_OP20	270	120	20	BE-I
E270_SP120_OP25	270	120	25	N
E270_SP120_OP30	270	120	30	N
E270_SP150_OP15	270	150	15	BE
E270_SP150_OP20	270	150	20	BE-I
E270_SP150_OP25	270	150	25	BE

E270_SP150_OP30	270	150	30	N
E270_SP200_OP15	270	200	15	BE
E270_SP200_OP20	270	200	20	BE-I
E270_SP200_OP25	270	200	25	BE-I
E270_SP200_OP30	270	200	30	NI
E270_SP250_OP15	270	250	15	BE
E270_SP250_OP20	270	250	20	BE-I
E270_SP250_OP25	270	250	25	BE-I
E280_SP70_OP20	280	70	20	NF
E280_SP80_OP20	280	80	20	NF
E280_SP80_OP25	280	80	25	NF
E280_SP90_OP20	280	90	20	BE
E280_SP90_OP25	280	90	25	NF
E280_SP90_OP30	280	90	30	NF
E280_SP120_OP20	280	120	20	BE
E280_SP120_OP25	280	120	25	N
E280_SP120_OP30	280	120	30	N
E280_SP150_OP25	280	150	25	BE
E280_SP150_OP30	280	150	30	N
E280_SP200_OP20	280	200	20	BE-I
E280_SP200_OP25	280	200	25	BE-I
E280_SP200_OP30	280	200	30	NI
E280_SP250_OP20	280	250	20	BE-I
E280_SP250_OP25	280	250	25	BE-I
E290_SP60_OP15	290	60	15	BE
E290_SP70_OP15	290	70	15	BE

E290_SP80_OP15	290	80	15	BE
E290_SP80_OP20	290	80	20	N
E290_SP80_OP25	290	80	25	N
E290_SP90_OP20	290	90	20	BE
E290_SP90_OP25	290	90	25	N
E290_SP90_OP30	290	90	30	N
E290_SP120_OP20	290	120	20	BE
E290_SP120_OP25	290	120	25	N
E290_SP120_OP30	290	120	30	NI
E290_SP150_OP20	290	150	20	BE-I
E290_SP150_OP25	290	150	25	BE
E290_SP150_OP30	290	150	30	NI
E290_SP200_OP20	290	200	20	BE-I
E290_SP200_OP25	290	200	25	BE-I
E290_SP200_OP30	290	200	30	NI
E290_SP250_OP20	290	250	20	BE-I
E290_SP250_OP25	290	250	25	BE-I
E290_SP250_OP30	290	250	30	BE-I
E310_SP80_OP15	310	80	15	BE
E310_SP80_OP20	310	80	20	NI
E310_SP80_OP25	310	80	25	NI
E310_SP80_OP30	310	80	30	NI
E310_SP90_OP15	310	90	15	BE
E310_SP90_OP20	310	90	20	NI
E310_SP90_OP25	310	90	25	NI
E310_SP90_OP30	310	90	30	NI

E310_SP100_OP15	310	100	15	BE
E310_SP120_OP20	310	120	20	BE-I
E310_SP120_OP25	310	120	25	NI
E310_SP120_OP30	310	120	30	NI
E310_SP150_OP20	310	150	20	BE-I
E310_SP150_OP25	310	150	25	NI
E310_SP150_OP30	310	150	30	NI
E310_SP200_OP20	310	200	20	BE-I
E310_SP200_OP25	310	200	25	FE-I
E310_SP200_OP30	310	200	30	NI
E310_SP250_OP20	310	250	20	BE-I
E310_SP250_OP25	310	250	25	BE-I
E310_SP250_OP30	310	250	30	NI

Table A.2: Models testing plate ages with 5 different E_{disl}

Models	E_{disl}	SP age (Ma)	OP age (Ma)	Mode
E510_SP60_OP20	510	60	20	D
E510_SP70_OP20	510	70	20	FE-D
E510_SP70_OP25	510	70	25	D
E510_SP70_OP35	510	70	35	D
E510_SP70_OP40	510	70	40	D
E510_SP80_OP20	510	80	20	FE-D
E510_SP80_OP25	510	80	25	FE-D
E510_SP80_OP30	510	80	30	D

E510_SP90_OP20	510	90	20	FE-D
E510_SP90_OP25	510	90	25	FE-D
E510_SP90_OP30	510	90	30	D
E510_SP100_OP25	510	100	25	FE
E510_SP100_OP30	510	100	30	FE-D
E510_SP100_OP35	510	100	35	D
E510_SP120_OP25	510	120	25	FE
E510_SP120_OP30	510	120	30	FE-F
E510_SP120_OP35	510	120	35	NF
E510_SP120_OP40	510	120	40	NF
E510_SP150_OP30	510	150	30	FE
E510_SP150_OP35	510	150	35	FE
E510_SP150_OP40	510	150	40	NF
E510_SP200_OP30	510	200	30	FE-D
E510_SP200_OP35	510	200	35	FE
E520_SP60_OP20	520	60	20	D
E520_SP70_OP20	520	70	20	FE-D
E520_SP70_OP25	520	70	25	D
E520_SP80_OP20	520	80	20	FE
E520_SP80_OP25	520	80	25	D
E520_SP80_OP30	520	80	30	D
E520_SP80_OP35	520	80	35	D
E520_SP90_OP20	520	90	20	FE
E520_SP90_OP25	520	90	25	FE
E520_SP90_OP30	520	90	30	D
E520_SP90_OP35	520	90	35	D

E520_SP100_OP30	520	100	30	D
E520_SP120_OP25	520	120	25	FE
E520_SP120_OP30	520	120	30	D
E520_SP120_OP35	520	120	35	D
E520_SP150_OP20	520	150	20	FE
E520_SP150_OP25	520	150	25	FE
E520_SP150_OP30	520	150	30	FE
E520_SP150_OP35	520	150	35	D
E520_SP170_OP35	520	170	35	D
E520_SP180_OP35	520	180	35	FE
E520_SP200_OP25	520	200	25	FE
E520_SP200_OP30	520	200	30	FE
E520_SP200_OP35	520	200	35	FE
E520_SP250_OP30	520	250	30	FE
E520_SP250_OP35	520	250	35	FE
E530_SP60_OP15	530	60	15	BE-D
E530_SP60_OP20	530	60	20	D
E530_SP60_OP25	530	60	25	D
E530_SP70_OP15	530	70	15	BE
E530_SP70_OP20	530	70	20	FE
E530_SP70_OP25	530	70	25	D
E530_SP80_OP15	530	80	15	BE
E530_SP80_OP20	530	80	20	BE
E530_SP80_OP25	530	80	25	D
E530_SP90_OP15	530	90	15	BE-D
E530_SP90_OP20	530	90	20	BE

E530_SP90_OP25	530	90	25	D
E530_SP120_OP15	530	120	15	BE
E530_SP120_OP20	530	120	20	FE
E530_SP120_OP25	530	120	25	BT
E530_SP120_OP30	530	120	30	D
E530_SP150_OP15	530	150	15	BE
E530_SP150_OP20	530	150	20	BT-FE
E530_SP150_OP25	530	150	25	FE
E530_SP150_OP30	530	150	30	D
E530_SP200_OP15	530	200	15	BE
E530_SP200_OP20	530	200	20	BE
E530_SP200_OP25	530	200	25	FE
E530_SP200_OP30	530	200	30	BE
E530_SP200_OP35	530	200	35	D
E530_SP250_OP15	530	250	15	BE
E530_SP250_OP20	530	250	20	BE
E530_SP250_OP25	530	250	25	BE
E530_SP250_OP30	530	250	30	BE-FE
E530_SP250_OP35	530	250	35	D
E530_SP270_OP20	530	270	20	BE
E530_SP270_OP25	530	270	25	BE
E530_SP270_OP30	530	270	30	BE
E530_SP270_OP35	530	270	35	D
E550_SP70_OP15	550	70	15	NI
E550_SP70_OP20	550	70	20	NI
E550_SP80_OP15	550	80	15	BT

E550_SP80_OP20	550	80	20	NI
E550_SP90_OP15	550	90	15	BE
E550_SP90_OP20	550	90	20	NI
E550_SP120_OP15	550	120	15	BE
E550_SP120_OP20	550	120	20	BT
E550_SP120_OP25	550	120	25	NI
E550_SP150_OP20	550	150	20	BE
E550_SP150_OP25	550	150	25	NI
E550_SP200_OP20	550	200	20	BE
E550_SP200_OP25	550	200	25	NI
E550_SP200_OP30	550	200	30	NI
E550_SP250_OP20	550	250	20	BE
E550_SP250_OP25	550	250	25	BT
E550_SP250_OP30	550	250	30	NI
E550_SP270_OP15	550	270	15	BE
E550_SP270_OP25	550	270	25	BE
E550_SP270_OP30	550	270	30	NI

Table A.3: Models testing plate ages with 5 different E_P

Models	E_P	SP age (Ma)	OP age (Ma)	Mode
E400_SP70_OP15	400	70	15	BE-D
E400_SP70_OP20	400	70	20	BE-OPSPD
E400_SP70_OP25	400	70	25	D
E400_SP70_OP30	400	70	30	D

E400_SP80_OP15	400	80	15	BE-OPSPD
E400_SP80_OP20	400	80	20	BE-D
E400_SP80_OP25	400	80	25	BE-D
E400_SP80_OP30	400	80	30	D
E400_SP90_OP15	400	90	15	BE-OPSPD
E400_SP90_OP20	400	90	20	BE-D
E400_SP90_OP25	400	90	25	BE-OPSPD
E400_SP90_OP30	400	90	30	D
E400_SP90_OP35	400	90	35	D
E400_SP120_OP15	400	120	15	BE-OPSPD
E400_SP120_OP20	400	120	20	BE-OPSPD
E400_SP120_OP25	400	120	25	BE-D
E400_SP120_OP30	400	120	30	BE-D
E400_SP120_OP35	400	120	35	BE-OPSPD
E400_SP150_OP15	400	150	15	BE-OPSPD
E400_SP150_OP20	400	150	20	BE-OPSPD
E400_SP150_OP25	400	150	25	BT-OPSPD
E400_SP150_OP30	400	150	30	BE-D
E400_SP150_OP35	400	150	35	BE-D
E400_SP200_OP15	400	200	15	BE-D
E400_SP200_OP20	400	200	20	BE-D
E400_SP200_OP25	400	200	25	BE-D
E400_SP200_OP30	400	200	30	BE-D
E400_SP200_OP35	400	200	35	BE-D
E400_SP250_OP15	400	250	15	BE-D
E400_SP250_OP20	400	250	20	BE-D

E400_SP250_OP25	400	250	25	BE-D
E400_SP250_OP30	400	250	30	BE-D
E400_SP250_OP35	400	250	35	BE-D
E400_SP270_OP20	400	270	20	BE-D
E400_SP270_OP25	400	270	25	BE-D
E400_SP270_OP30	400	270	30	BE-D
E400_SP270_OP35	400	270	35	BE-D
E450_SP70_OP20	450	70	20	BE-OPSPD
E450_SP70_OP25	450	70	25	D
E450_SP80_OP20	450	80	20	BE-D
E450_SP80_OP25	450	80	25	D
E450_SP90_OP20	450	90	20	BE-D
E450_SP90_OP25	450	90	25	BE-D
E450_SP90_OP30	450	90	30	D
E450_SP120_OP20	450	120	20	BE-D
E450_SP120_OP25	450	120	25	BE
E450_SP120_OP30	450	120	30	BE
E450_SP150_OP25	450	150	25	BE
E450_SP150_OP30	450	150	30	BE
E450_SP150_OP35	450	150	35	BE
E450_SP200_OP25	450	200	25	BE
E450_SP200_OP30	450	200	30	BE
E450_SP200_OP35	450	200	35	BE
E450_SP250_OP25	450	250	25	BE
E450_SP250_OP30	450	250	30	BE
E450_SP270_OP30	450	270	30	BE

E500_SP60_OP15	500	60	15	BE-D
E500_SP60_OP20	500	60	20	D
E500_SP60_OP25	500	60	25	NI
E500_SP70_OP15	500	70	15	BE
E500_SP70_OP20	500	70	20	BT
E500_SP70_OP25	500	70	25	NI
E500_SP80_OP15	500	80	15	BE-D
E500_SP80_OP20	500	80	20	BE
E500_SP80_OP25	500	80	25	NI
E500_SP90_OP15	500	90	15	BE-D
E500_SP90_OP20	500	90	20	BE
E500_SP90_OP25	500	90	25	NI
E500_SP90_OP30	500	90	30	NI
E500_SP120_OP15	500	120	15	BE
E500_SP120_OP20	500	120	20	BE
E500_SP120_OP25	500	120	25	BE
E500_SP120_OP30	500	120	30	NI
E500_SP150_OP15	500	150	15	BE
E500_SP150_OP20	500	150	20	BE
E500_SP150_OP25	500	150	25	BE
E500_SP150_OP30	500	150	30	NI
E500_SP200_OP20	500	200	20	BE
E500_SP200_OP25	500	200	25	BE
E500_SP200_OP30	500	200	30	BE
E500_SP200_OP35	500	200	35	NI
E500_SP250_OP20	500	250	20	BE

E500_SP250_OP25	500	250	25	BE
E500_SP250_OP30	500	250	30	BE
E500_SP250_OP35	500	250	35	NI
E500_SP270_OP35	500	270	35	BT
E560_SP60_OP15	560	60	15	D
E560_SP70_OP15	560	70	15	BE
E560_SP80_OP15	560	80	15	BE
E560_SP90_OP15	560	90	15	BE
E560_SP90_OP20	560	90	20	NI
E560_SP100_OP20	560	100	20	NI
E560_SP120_OP20	560	120	20	BE
E560_SP120_OP25	560	120	25	NI
E560_SP150_OP20	560	150	20	BE
E560_SP150_OP25	560	150	25	NI
E560_SP200_OP20	560	200	20	BE
E560_SP200_OP25	560	200	25	BT
E560_SP250_OP25	560	250	25	BE
E560_SP250_OP30	560	250	30	NI
E560_SP270_OP25	560	270	25	BE
E560_SP270_OP30	560	270	30	NI

Table A.4: Models testing plate ages with 5 different friction coefficients

Models	friction coefficient	SP age (Ma)	OP age (Ma)	Mode

fc0.1_SP70_OP15	0.1	70	15	BE-OPSPD
fc0.1_SP70_OP20	0.1	70	20	BE-FE
fc0.1_SP70_OP25	0.1	70	25	OPSPD
fc0.1_SP70_OP30	0.1	70	30	OPSPD
fc0.1_SP80_OP15	0.1	80	15	BE-OPSPD
fc0.1_SP80_OP20	0.1	80	20	BE-OPSPD
fc0.1_SP80_OP25	0.1	80	25	OPSPD
fc0.1_SP80_OP30	0.1	80	30	OPSPD
fc0.1_SP90_OP15	0.1	90	15	BE-OPSPD
fc0.1_SP90_OP20	0.1	90	20	BE-OPSPD
fc0.1_SP90_OP25	0.1	90	25	BE-OPSPD
fc0.1_SP90_OP30	0.1	90	30	OPSPD
fc0.1_SP120_OP15	0.1	120	15	BE-OPSPD
fc0.1_SP120_OP20	0.1	120	20	BE-OPSPD
fc0.1_SP120_OP25	0.1	120	25	BE-OPSPD
fc0.1_SP120_OP30	0.1	120	30	BE-OPSPD
fc0.1_SP150_OP15	0.1	150	15	BE-OPSPD
fc0.1_SP150_OP20	0.1	150	20	BE-OPSPD
fc0.1_SP150_OP25	0.1	150	25	BE-OPSPD
fc0.1_SP150_OP30	0.1	150	30	BE-OPSPD
fc0.1_SP200_OP15	0.1	200	15	BE-OPSPD
fc0.1_SP200_OP20	0.1	200	20	BE-OPSPD
fc0.1_SP200_OP25	0.1	200	25	BE-OPSPD
fc0.1_SP200_OP30	0.1	200	30	BE-OPSPD
fc0.1_SP250_OP15	0.1	250	15	BE-OPSPD

fc0.1_SP250_OP20	0.1	250	20	BE-OPSPD
fc0.1_SP250_OP25	0.1	250	25	BE-OPSPD
fc0.1_SP250_OP30	0.1	250	30	BE-OPSPD
fc0.14_SP55_OP15	0.14	55	15	BE-OPSPD
fc0.14_SP60_OP15	0.14	60	15	BE-OPSPD
fc0.14_SP70_OP15	0.14	70	15	BE-D
fc0.14_SP70_OP20	0.14	70	20	BT-D
fc0.14_SP70_OP25	0.14	70	25	OPSPD
fc0.14_SP70_OP30	0.14	70	30	OPSPD
fc0.14_SP80_OP15	0.14	80	15	BE-OPSPD
fc0.14_SP80_OP20	0.14	80	20	BE-D
fc0.14_SP80_OP25	0.14	80	25	BE
fc0.14_SP80_OP30	0.14	80	30	OPSPD
fc0.14_SP90_OP15	0.14	90	15	BE-OPSPD
fc0.14_SP90_OP20	0.14	90	20	BE-D
fc0.14_SP90_OP25	0.14	90	25	D
fc0.14_SP120_OP15	0.14	120	15	BE-D
fc0.14_SP120_OP20	0.14	120	20	BE-OPSPD
fc0.14_SP120_OP25	0.14	120	25	BE
fc0.14_SP120_OP30	0.14	120	30	D
fc0.14_SP150_OP15	0.14	150	15	BE-D
fc0.14_SP150_OP20	0.14	150	20	BE-D
fc0.14_SP150_OP25	0.14	150	25	BE
fc0.14_SP150_OP30	0.14	150	30	BE
fc0.14_SP200_OP15	0.14	200	15	BE-D
fc0.14_SP200_OP20	0.14	200	20	BE

fc0.14_SP200_OP25	0.14	200	25	BE
fc0.14_SP200_OP30	0.14	200	30	BE
fc0.14_SP250_OP15	0.14	250	15	BE
fc0.14_SP250_OP20	0.14	250	20	BE
fc0.14_SP250_OP25	0.14	250	25	BE
fc0.14_SP250_OP30	0.14	250	30	BE
fc0.18_SP55_OP15	0.18	55	15	D
fc0.18_SP60_OP15	0.18	60	15	BE-D
fc0.18_SP70_OP15	0.18	70	15	BE
fc0.18_SP70_OP20	0.18	70	20	NI
fc0.18_SP80_OP15	0.18	80	15	BE
fc0.18_SP80_OP20	0.18	80	20	BT
fc0.18_SP80_OP25	0.18	80	25	NI
fc0.18_SP80_OP30	0.18	80	30	NI
fc0.18_SP90_OP15	0.18	90	15	BE
fc0.18_SP90_OP20	0.18	90	20	BE
fc0.18_SP90_OP25	0.18	90	25	NI
fc0.18_SP90_OP30	0.18	90	30	NI
fc0.18_SP120_OP15	0.18	120	15	BE
fc0.18_SP120_OP20	0.18	120	20	BE
fc0.18_SP120_OP25	0.18	120	25	BT
fc0.18_SP120_OP30	0.18	120	30	NI
fc0.18_SP150_OP15	0.18	150	15	BE
fc0.18_SP150_OP20	0.18	150	20	BE-I
fc0.18_SP150_OP25	0.18	150	25	BE
fc0.18_SP150_OP30	0.18	150	30	NI

fc0.18_SP200_OP15	0.18	200	15	BE
fc0.18_SP200_OP20	0.18	200	20	BE-I
fc0.18_SP200_OP25	0.18	200	25	BE-I
fc0.18_SP200_OP30	0.18	200	30	BT-I
fc0.18_SP250_OP15	0.18	250	15	BE
fc0.18_SP250_OP20	0.18	250	20	BE-I
fc0.18_SP250_OP25	0.18	250	25	BE-I
fc0.18_SP250_OP30	0.18	250	30	BE-I
fc0.22_SP55_OP15	0.22	55	15	BT-I
fc0.22_SP60_OP15	0.22	60	15	BE-I
fc0.22_SP70_OP15	0.22	70	15	BE-I
fc0.22_SP80_OP15	0.22	80	15	BE-I
fc0.22_SP80_OP20	0.22	80	20	NI
fc0.22_SP80_OP25	0.22	80	25	NI
fc0.22_SP80_OP30	0.22	80	30	NI
fc0.22_SP90_OP15	0.22	90	15	BE-I
fc0.22_SP90_OP20	0.22	90	20	NI
fc0.22_SP90_OP25	0.22	90	25	NI
fc0.22_SP90_OP30	0.22	90	30	NI
fc0.22_SP120_OP15	0.22	120	15	BE-I
fc0.22_SP120_OP20	0.22	120	20	BE-I
fc0.22_SP120_OP25	0.22	120	25	NI
fc0.22_SP120_OP30	0.22	120	30	NI
fc0.22_SP150_OP15	0.22	150	15	BE-I
fc0.22_SP150_OP20	0.22	150	20	BE-I
fc0.22_SP150_OP25	0.22	150	25	NI

fc0.22_SP150_OP30	0.22	150	30	NI
fc0.22_SP200_OP15	0.22	200	15	BE-I
fc0.22_SP200_OP20	0.22	200	20	BE-I
fc0.22_SP200_OP25	0.22	200	25	BE-I
fc0.22_SP200_OP30	0.22	200	30	NI
fc0.22_SP250_OP15	0.22	250	15	BE-I
fc0.22_SP250_OP20	0.22	250	20	BE-I
fc0.22_SP250_OP25	0.22	250	25	BE-I
fc0.22_SP250_OP30	0.22	250	30	BT-I
fc0.26_SP70_OP15	0.26	70	15	NI
fc0.26_SP80_OP15	0.26	80	15	FE
fc0.26_SP80_OP20	0.26	80	20	NI
fc0.26_SP90_OP15	0.26	90	15	FE
fc0.26_SP90_OP20	0.26	90	20	NI
fc0.26_SP120_OP15	0.26	120	15	FE
fc0.26_SP120_OP20	0.26	120	20	FE
fc0.26_SP120_OP25	0.26	120	25	NI
fc0.26_SP150_OP20	0.26	150	20	FE
fc0.26_SP150_OP25	0.26	150	25	NI
fc0.26_SP200_OP25	0.26	200	25	FE
fc0.26_SP250_OP25	0.26	250	25	FE

Table A.5: Models of SP90_OP20 with various hot region

Models	Width (km)	Distance (km)	ΔT (°C)	Mode

w50_Di100_T50	50	100	50	NE
w50_Di100_T800	50	100	100	NE
w50_Di110_T200	50	110	200	EF
w50_Di110_T300	50	110	300	EF
w50_Di110_T800	50	110	800	EF
w50_Di120_T50	50	120	50	NE
w50_Di120_T100	50	120	100	NE
w50_Di120_T200	50	120	200	EF
w50_Di120_T800	50	120	800	EF
w50_Di130_T50	50	130	50	NE
w50_Di130_T100	50	130	100	EF
w50_Di130_T200	50	130	200	EF
w50_Di130_T300	50	130	300	EF
w50_Di130_T400	50	130	400	EF
w50_Di130_T500	50	130	500	EH
w50_Di130_T600	50	130	600	EH
w50_Di130_T700	50	130	700	EH
w50_Di130_T800	50	130	800	EH
w50_Di140_T50	50	140	50	NE
w50_Di140_T100	50	140	100	EF
w50_Di140_T300	50	140	300	EH
w50_Di150_T50	50	150	50	EF
w50_Di150_T100	50	150	100	EF
w50_Di150_T300	50	50	300	EH
w50_Di160_T50	50	160	50	EF

w50_Di160_T100	50	160	100	EF
w50_Di160_T200	50	160	200	EH
w50_Di160_T300	50	160	300	EH
w50_Di170_T50	50	170	50	EF
w50_Di170_T300	50	170	300	EH
w50_Di180_T100	50	180	100	EH
w50_Di180_T300	50	180	300	EH
w50_Di190_T50	50	190	50	EH
w50_Di190_T300	50	190	300	EH
w50_Di200_T50	50	200	50	EH
w50_Di200_T800	50	200	800	EH
w50_Di400_T50	50	400	50	EH
w50_Di750_T50	50	700	50	EH
w50_Di750_T100	50	700	100	EH
w50_Di750_T300	50	700	300	EH
w50_Di800_T50	50	800	50	EH
w50_Di800_T100	50	800	100	EH
w50_Di800_T300	50	800	300	EH
w50_Di900_T50	50	900	50	EH
w50_Di900_T100	50	900	100	EH
w50_Di900_T300	50	900	300	EH
w50_Di1050_T50	50	1050	50	EF
w50_Di1050_T100	50	1050	100	EH
w50_Di1050_T300	50	1050	300	EH
w25_Di125_T200	25	125	200	NE
w25_Di125_T300	25	125	300	EF

w25_Di150_T200	25	150	200	EF
w25_Di150_T300	25	150	300	EF
w25_Di150_T800	25	150	800	EH
w25_Di175_T200	25	175	200	EH
w25_Di175_T800	25	175	800	EH
w25_Di200_T800	25	200	800	EH

Table A.6: Models testing plate ages with/without a hot region

Models	SP age (Ma)	OP age (Ma)	hot region	Mode
SP55_OP15	55	15	N	NE
SP60_OP15	60	15	N	E
SP90_OP20 (RM)	90	20	N	NE
SP95_OP20	95	20	N	E
SP150_OP25	150	25	N	NE
SP160_OP25	160	25	N	NE
SP170_OP25	170	25	N	E
SP240_OP30	175	30	N	NE
SP275_OP30	275	30	N	NE
SP280_OP30	280	30	N	E
SP300_OP30	300	30	N	E
SP300_OP30	300	30	N	E
hSP55_OP15	55	15	Y	EH
hSP60_OP15	60	15	Y	EH-D

hSP60_OP18	60	18	Y	EH
hSP60_OP20	60	20	Y	NE
hSP70_OP15	70	15	Y	EH-D
hSP70_OP20	70	20	Y	EH
hSP80_OP15	80	15	Y	EH
hSP80_OP18	80	18	Y	EH
hSP80_OP22	80	22	Y	EH
hSP90_OP15	90	15	Y	EH
hSP90_OP22	90	22	Y	EH
hSP90_OP23	90	23	Y	NE
hSP90_OP25	90	25	Y	NE
hSP100_OP15	100	15	Y	EF
hSP100_OP20	100	20	Y	EH
hSP100_OP22	100	22	Y	EF+EH
hSP100_OP23	100	23	Y	NE
hSP110_OP15	110	15	Y	EF
hSP110_OP20	110	20	Y	EH
hSP110_OP22	110	20	Y	EF
hSP110_OP23	110	20	Y	EF
hSP120_OP15	120	15	Y	EF
hSP120_OP20	120	20	Y	EF+EH
hSP120_OP22	120	22	Y	EF
hSP120_OP23	120	23	Y	EF
hSP120_OP25	120	25	Y	NE
hSP130_OP20	130	20	Y	EF
hSP150_OP15	150	15	Y	EF+EH

hSP150_OP20	150	20	Y	EF
hSP150_OP22	150	22	Y	EF
hSP150_OP23	150	23	Y	EF
hSP150_OP25	150	25	Y	EF
hSP150_OP30	150	30	Y	NE
hSP200_OP15	200	15	Y	EF
hSP200_OP20	200	20	Y	EF
hSP200_OP25	200	25	Y	EF
hSP250_OP30	250	30	Y	EF
hSP300_OP30	300	30	Y	EF
hSP350_OP30	350	30	Y	EF